EFFECT OF ANTISCALANTS DURING EUTECTIC FREEZE CRYSTALLIZATION OF A REVERSE OSMOSIS RETENTATE

Edward Michael Peters,
Supervisor: Dr. Marcos Rodriguez-Pascual
Co-Supervisor: Professor Alison Emslie Lewis

Dissertation submitted in fulfilment of the requirements for the degree of Master of Science in Engineering

---

Department of Chemical Engineering
Faculty of Engineering and Built Environment
University of Cape Town

February, 2015

***Declaration*:** *I know the meaning of plagiarism and declare that all the work in the document, save for that which is properly referenced, is mine*

.....

Acknowledgements

The author would like to thank the following:

- The main Supervisor, Dr. Marcos Rodriguez-Pascual, and co-Supervisor, Professor Alison Emslie Lewis, for their support in conducting this research as well as proofreading the thesis. Their guidance, expertise and knowledge was indispensable in all the experimental work conducted as well as data analysis and writing.
- The University of Cape Town (UCT) for the financial assistance granted in the form of a UCT International Scholarship, a Research Associateship award and the Chemical Engineering bursary. This catered for all the academic resources and social welfare required for successful culmination of this research.
- Former and current students in the Crystallization and Precipitation (CPU) research unit at UCT for their morale and knowledge support. These include Dereck Ndoro, Vuyiswa Dube, Sibongiseni Gcebe, Lucia Dzinza and Michael Kapembwa. The author would like to thank Dereck Ndoro, Jemitias Chivavava and Moses Nduna for their effort in proofreading the final thesis and providing suggestions. Not forgetting the effort providing by Dereck Ndoro in setting up the continuous EFC crystallizer and the support he provided throughout the experimental work.

Thank you!

Abstract

Eutectic Freeze Crystallization (EFC) is a separation technique which involves simultaneous crystallization of water and solute under eutectic conditions. It can be applied to treatment of various industrial aqueous streams containing dissolved organic and inorganic contaminants, such as reverse osmosis (RO) retentate brine streams. Since antiscalants are dosed in RO feed streams, these become concentrated in the retentate brine stream and could have an undesirable effect on crystallization kinetics of both ice and salt in EFC. In this study, the impact of a phosphonate antiscalant on the kinetic processes of nucleation and growth in EFC was investigated. Firstly, the effect of an antiscalant on the thermodynamic phase equilibria of a binary Na_2SO_4 aqueous solution was experimentally determined. The effect of the antiscalant on the nucleation and growth rates of both ice and salt in a continuous EFC process was then established for concentrations of 200, 350 and 500 mg/L of antiscalant. Product quality parameters such as the Crystal Size Distribution (CSD), morphology and purity of crystals were also measured since they are directly affected by the kinetic rate processes investigated.

It was observed that, the antiscalant did not change the eutectic temperature of a binary Na_2SO_4 aqueous solution. There was no significant change in the salt nucleation rate for the entire range of antiscalant concentrations investigated. The ice nucleation rate diminished up to an antiscalant concentration of 350 mg/L after which it increased in the presence of 500 mg/L antiscalant. A general increase in growth rate of ice in the presence of 350 mg/L and 500 mg/L antiscalant was observed and this was consistent with the trend obtained for the mean and median particle sizes. The growth rate for salt increased up to 350 mg/L antiscalant beyond which it diminished in the presence of 500 mg/L antiscalant with the mean and median crystal sizes following the same trend. This suggested a turning point in the effect of the antiscalant between concentrations of 350 and 500 mg/L. There were no changes observed in the morphology of both ice and salt. The phosphorus content in both ice and salt increased with increasing antiscalant concentration and washing was very effective in reducing the impurity concentration in the products.

Table of Contents

List of figures

List of tables

Nomenclature

Abbreviation	Description	Units
a	Activity	kg/kg solvent
a_*	Activity at equilibrium	kg/kg solvent
AAS	Atomic Absorption Spectroscopy	
A_c	Crystal surface area	m^2
A	Kinetic parameter for primary nucleation	
A_f	Area of focus	m^2
ATMP	Aminotris (methylene phosphonic acid)	
C	Concentration	kg/kg solution
C^*	Surface concentration	kg/kg solution
C_*	Equilibrium concentration	kg/kg solution
$C^*(\infty)$	Equilibrium solubility for spherical particles of very large radius	kg/kg solution
$C^*(r)$	Equilibrium solubility for spherical particles of small radius	kg/kg solution
C_a	Antiscalant concentration	mg/L
C_i	Interfacial concentration	kg/kg solution
C_m	Metastable limit concentration	kg/kg solution
CSD	Crystal Size Distribution	
CV	Co-efficient of Variation	%
Da	Dalton (Atomic Mass Unit)	
d_e	Equivalent spherical diameter of a crystal	m
d_f	Depth of field of focus	m
dL	Change in particle size	m
dm	Change in mass	kg
dt	Change in time	s
DHTPMP	Dihexamethylene triaminepenta (methylene phosphonic acid)	
DTPMP	Diethylene triamine penta (methylene phosphonic acid)	
E_f	Cryoscopic constant	kg/(mol.K)
F(L)	Crystal cumulative distribution function	

f(L) dL	Crystal density distribution function	
FPD	Freezing Point Depression	K
g	Order of growth process	
G	Growth rate	m/s
G_l	Linear growth rate	m/s
G_m	Mass growth rate	kg/s
HDTMP	Hexamethylene diamine tetra (methylene phosphonic acid)	
HEDP	1-hydroxyethylene-1,1-diphosphonic acid	
J	Nucleation rate	#/(m^3.s)
i	Exponent in secondary nucleation rate equation	
ICP-MS	Inductively Coupled Plasma Mass Spectroscopy	
ICP-OES	Inductively Coupled Plasma Optical Emission Spectroscopy	
f	Exponent in secondary nucleation rate equation	
j	Order of nucleation process	
k	Boltzmann constant (1.3805×10^{-23})	J/K
K_G	Overall crystal growth co-efficient	
K_j	Heterogeneous nucleation rate constant	
K'_j	Secondary nucleation rate constant	
L	Particle size	m
L_m	Mean crystal / particle size	m
L_D	Dominant / modal crystal size	m
m	Mass	kg
MP	Methylene phosphonic acid	
M_r	Molar mass	g/mol
MSMPR	Mixed Suspension Mixed Product Removal	
MSZW	Metastable Zone Width	K
m_2	Molality (moles solute per kg solvent)	Moles / kg solvent
m_f	Final mass	kg
m_i	Initial mass	kg

M_T	Magma density (mass of crystals per unit volume of solution)	kg/m^3
n	Crystal population density	$\#/(m^3.m)$
N	Specific crystal population	$\#/m^3$
NMR	Nuclear Magnetic Resonance	
n_o	Nuclei population density	$\#/(m^3.m)$
p_l	Length of one pixel	m
PBM	Population Balance Model	
PBE	Population Balance Equation	
PSD	Particle Size Distribution	
Q	Volumetric flow rate	m^3/s
R	Universal gas constant (8.314)	J/(mol.K)
r	Equivalent spherical radius of a crystal	m
r_c	Critical nuclei radius	m
S	Supersaturation ratio	
S_A	Surface area	m^2
S_a	Surface area	$pixels^2$
Sd	Standard deviation	
T	Absolute Temperature	K
t	Time	s
T_*	Equilibrium temperature	K
T_f	Absolute freezing point temperature	K
T_m	Metastable limit temperature	K
v	Ionization factor	
V	Crystallizer volume	m^3
V_m	Molecular volume	m^3
W	Agitation rate	rpm
x	Activity co-efficient	
XRD	X-ray Diffraction	
X	Dry mass	%
x_*	Activity co-efficient at equilibrium	
ΔC	Concentration difference	Kg/kg solution
$\Delta_{fus}H$	Molar enthalpy of fusion	J/mol

ΔG_c	Critical Gibb's free energy change	J/mol
ΔL_b	Crystal size interval	m
ΔT	Temperature difference	K

Symbols

Symbol	Description	Units
#	Number	
μ	Chemical potential	J/kg
μ*	Chemical potential at equilibrium	J/kg
α	Surface energy of a solid phase	J/m^2
γ	Interfacial energy between solute and solution	J/m^2
Δμ	Chemical potential difference	J/kg
π	Pi (3.14)	
σ	Relative supersaturation	
τ	Hydraulic residence time	s
Ω	Unit for electrical resistance	Ohm

1 Introduction

1.1 Background

Reverse osmosis (RO) plants are in wide use for treating industrial waste water due to their ability to produce potable water. However, by removal of water at high recoveries greater than 70 %, the reject brine becomes highly concentrated in ionic salts. The current practice is to dispose of this reject brine in lined evaporative ponds which require huge spaces of land and can cause environmental pollution. Further treatment of this brine using RO is uneconomical due to increased scaling potential of salts on membrane surfaces, thereby reducing operational efficiency of the plant, reducing membrane life span and increasing downtime due to increased frequency of cleaning required. In order to achieve zero waste discharge, Eutectic Freeze Crystallization (EFC) can be coupled with RO plants to simultaneously recover saleable salts and pure water from these concentrated brine streams. Essentially, the residual brine obtained from filtration of both ice and salt slurries can be recycled to achieve zero waste discharge. Reddy and co-workers (2010) showed that EFC can be used to process an RO retentate stream containing 4 % sodium sulphate (Na_2SO_4) and a number of impurities (F^-, Cl^-, K^+, Li^+, Mg^{2+}, Ca^{2+}, NO_3^- and NH_4^+) producing pure water in the form of ice and mirabilite ($Na_2SO_4.10H_2O$) salt crystals.

EFC is a technique in which pure salt(s) are recovered from industrial brine streams simultaneously with pure water by operating under sub-eutectic conditions. It has several advantages over conventional separation techniques such as evaporative crystallization (EC). It is highly energy efficient since the latent heat of fusion of ice is about six times less than the latent heat of vaporization of water. The operating cost savings of EFC over EC were reported to be 80 – 85 % (Nathoo et al., 2009). Theoretically, a 100 % yield can be achieved at high purities. In EFC, gravitational separation of ice and salt can be achieved in the crystallizer due to density differences between ice crystals, salt crystals and mother liquor. EFC requires a smaller area of land as compared to evaporative ponds which are in wide use for storage and volume reduction of brine streams by natural evaporation.

Knowledge of the interdependences between impurity concentration and crystallization kinetics facilitates control of crystallization processes to obtain products of a desirable Crystal Size Distribution (CSD) and shape (Rauls et al., 2000).

1.2 Problem statement

Antiscalants are dosed in feed streams of RO plants so as to reduce scaling on membranes which occurs by precipitation of sparingly soluble salts, such as, calcium carbonate and sulphates of calcium, magnesium and barium. Due to high water recoveries of RO membranes, the antiscalants become concentrated in the retentate brine stream. These antiscalants could have an effect on thermodynamics (phase equilibria) and kinetics (nucleation and growth rates) of both ice and salt in EFC. This can affect the choice of operating conditions, such as supersaturation, in order to obtain a desired product yield and quality. Therefore, it is necessary to understand the effect of antiscalants on thermodynamics and kinetics in continuous EFC. According to Ruiz-Agudo and co-workers (2006), there is little information about the effect of phosphonates on the crystallization of alkali metal soluble salts. Understanding of the effects of additives or impurities is paramount to the design and development of crystallization processes (Qu et al., 2006).

1.3 Aim

This research aims to investigate the effect of a phosphonate antiscalant on the phase equilibria of an aqueous electrolyte system as well as the nucleation and growth rates of both ice and salt crystals in a continuous EFC process. The nucleation and growth rates are highly dependent on the operating conditions such as residence time and supersaturation. If the antiscalant has a deleterious effect on ice and salt crystallization in EFC, that could necessitate the inclusion of a pre-treatment step to remove the antiscalants from the waste water stream, or a change in the operating conditions and crystallizer design.

1.4 Project scope

The research will focus on both ice and $Na_2SO_4.10H_2O$ crystallization in EFC and phosphonate antiscalant concentrations normally encountered in industry will be used. Information obtained on antiscalant data sheets reveals that normal dosages do not normally exceed 5 mg/L. The research is based on a case study of an RO plant used to treat acid mine drainage (AMD) in South Africa. This plant has a water recovery of about 99 % implying that the antiscalant concentration in the retentate brine is increased by a factor of 100. Therefore, antiscalant concentrations below 500 mg/L were investigated as the worst case scenario based on an assumption that the antiscalant does not lose activity and all of it is in the retentate brine. The determination of nucleation and growth rates of crystals requires

solubility data; hence the need to determine changes in solubility in the presence of different antiscalant concentrations. Following this, the effect of antiscalants on crystallization kinetics was determined. Nucleation and / or growth rates determine the final product quality (Crystal Size Distribution (CSD) and morphology), therefore investigations on the effect of antiscalant on these quality parameters were conducted.

1.5 Plan of development

The thesis comprises of four main chapters. Chapter 2 provides the basic theory behind crystallization in general, principle of operation of EFC, antiscalants and their functional mechanisms, crystallization thermodynamics and kinetics as well as product quality, that is, CSD and morphology. Following this, a critical synthesis of literature on the effect of antiscalant and other impurities or additives on crystallization thermodynamics and kinetics, CSD and morphology is presented in Chapter 3. In this chapter, the research gap is identified, research questions are clearly laid out and the hypothesis is formulated on the basis of theory and literature findings. However, literature on the effect of antiscalants on these parameters in EFC could not be found. Most of the literature centres on the effect of antiscalants and other impurities in evaporative and cooling crystallization. Chapter 4 covers the methodology inclusive of experimental design, experimental set-up and experimental procedure in detail. A thorough description of the equipment and materials used is given here. The results and discussion section follows in Chapter 5 and this presents the experimental results and detailed explanation of the trends observed with reference to literature. Deviations from expected results are thoroughly explained and conclusions are drawn from this.

2 Theory

Crystallization is a solid-liquid separation process by which a solute or the solvent is recovered from a solution or a melt in crystalline form. It is a rate process, which is dependent upon the thermodynamic driving force for nucleation and growth. This driving force is termed supersaturation.

2.1 Supersaturation

Supersaturation is defined more rigorously as the deviation from thermodynamic equilibrium in any of the three forms presented below (Ulrich and Stelzer, 2011):

1. The difference between the chemical potential of a solute in solution (μ) and the chemical potential of the solution in equilibrium with the solid phase (μ_*).

$$\Delta\mu = \mu - \mu_* \tag{2-1}$$

2. The difference between the solute concentration (C) and the equilibrium concentration (C_*).

$$\Delta C = C - C_* \tag{2-2}$$

3. The difference between the system temperature at equilibrium (T_*) and the actual temperature (T).

$$\Delta T = T_* - T \tag{2-3}$$

Supersaturation is also expressed as supersaturation ratio and relative supersaturation defined as follows:

$$S = \frac{C}{C_*} \tag{2-4}$$

$$\sigma = \frac{C - C_*}{C_*} \tag{2-5}$$

where, S is the supersaturation ratio and σ is the relative supersaturation. Supersaturation is related to chemical potential by the following expressions (Myerson, 2002):

$$\frac{\mu - \mu_*}{RT} = \nu \ln \frac{a}{a^*} \tag{2-6}$$

$$\frac{\Delta\mu}{RT} = \nu \ln \frac{x\,C}{x^* C^*} \tag{2-7}$$

where, R is the universal gas constant, T is the absolute temperature, v is the number of ions in solution, a is the activity, x is the activity co-efficient and C is the concentration.

2.2 Crystallization kinetics

Crystallization occurs by two fundamental kinetic processes of nucleation and crystal growth. These processes, in addition to other operating variables in the crystallizer determine crystal characteristics such as the crystal size distribution, purity and morphology obtained (Ulrich and Stelzer, 2011).

2.2.1 Nucleation

Nucleation is the "process of random generation of nanoscopically small formations of the new phase that have the ability for irreversible overgrowth to macroscopic sizes" (Kashchiev, 2000). It is subdivided into two: primary nucleation, which occurs spontaneously in the absence of crystals (homogeneous) or in the presence of foreign particles (heterogeneous), and secondary nucleation which is induced by the presence of crystals. Figure 2-1 summarizes this categorization.

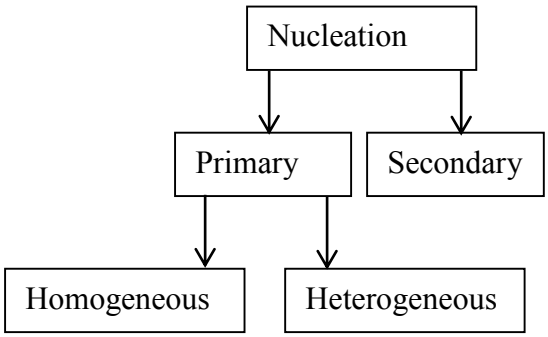

Figure 2-1. Types of nucleation (adapted from Mullin, 2001)

2.2.1.1 Primary homogeneous nucleation

The nucleation rate, J, defined as the number of nuclei formed per unit time per unit volume can be expressed in the form of the Arrhenius reaction velocity equation (Sangwal, 2007):

$$J = A\exp\left(\frac{-\Delta G_c}{kT}\right) \qquad 2\text{-}8$$

where, A is a kinetic parameter determined by attachment of atoms / molecules to the nucleus, $-\Delta G_c$ is the critical Gibbs free energy associated with formation of critical nuclei, k is the Boltzmann constant with a value of 1.3805×10^{-23} J/K (Perry and Green, 2007) and T is the absolute temperature. ΔG_c can be calculated by combining the classical nucleation theory which takes into consideration the free energy change associated with phase transition (Gibbs, 1948; Volmer, 1939 and Becker and Doring, 1935 as cited by Mullin, 2001) and the

Gibbs-Thomson relationship which relates supersaturation ratio, S and nucleus radius, r (Sangwal, 2007). Assuming a spherical nucleus, the resulting expression is:

$$J = Aexp\left(\frac{-16\pi\gamma^3 {V_m}^2}{3k^3T^3(\ln S)^2}\right) \quad 2\text{-}9$$

where, γ is the interfacial energy between the solute surface and solution, and V_m is the molecular volume. It is notable that increasing the temperature and supersaturation whilst decreasing the interfacial tension facilitate formation of 3D nuclei. This occurs by reduction of the Gibb's free energy barrier (ΔG_c) required for formation of stable nuclei with critical sizes. Homogeneous nucleation occurs at high supersaturation levels.

2.2.1.2 Heterogeneous nucleation

This occurs in the presence of foreign particles (heteronuclei) at a lower degree of supersaturation. The presence of heteronuclei lowers the activation energy barrier and the critical nuclei size required for growth. Classical relationships have little use and a simple empirical power law (from the Becker-Doring relationship) can be justified (Myerson, 2002):

$$J = K_j(\Delta C)^j \quad 2\text{-}10$$

where, K_j is the primary nucleation rate constant, ΔC is the concentration driving force (supersaturation) and j is the order of the nucleation process. The latter is usually greater than two and depends on the physical properties such as suspension density as well as the hydrodynamics of the system (Myerson, 2002).

2.2.1.3 Secondary nucleation

Secondary nucleation is dominant in continuous crystallizers and is induced by the presence of seed crystals. This improves the purity of the product, crystal morphology and crystal size distribution (CSD). Processes that govern secondary nucleation include generation of secondary nuclei on or near a solid phase, removal of the clusters and growth to form a new solid phase. These are all dependent on supersaturation, rate of cooling, degree of agitation and the presence of impurities (Myerson, 2002). Secondary nucleation occurs at low supersaturation levels in the metastable zone by various mechanisms, which include initial or dust breeding, needle breeding, collision breeding, impurity concentration gradient and fluid shear (Myerson, 2002). In industrial crystallizers, contact nucleation is dominant and the nucleation rate, J, is a function of the degree of agitation, suspension density and supersaturation as shown in Equation 2-11:

$$J = K_j' W^i M_T^f (\Delta C)^j \qquad 2\text{-}11$$

where, K_j' is the secondary nucleation rate constant, W is the rate of agitation in revolutions per minute and M_T is the suspension density (mass of crystals per unit volume of solution). Exponents i, f and j vary according to the operating conditions (Richardson et al., 2002).

2.2.1.4 Zones of crystallization

Figure 2-2 shows the zones of crystallization and the concept of metastability. Supersaturation is attained by evaporating solvent from the solution effected by heating, or by reduction of solubility effected by dropping the temperature as in the case of cooling crystallization and freeze crystallization.

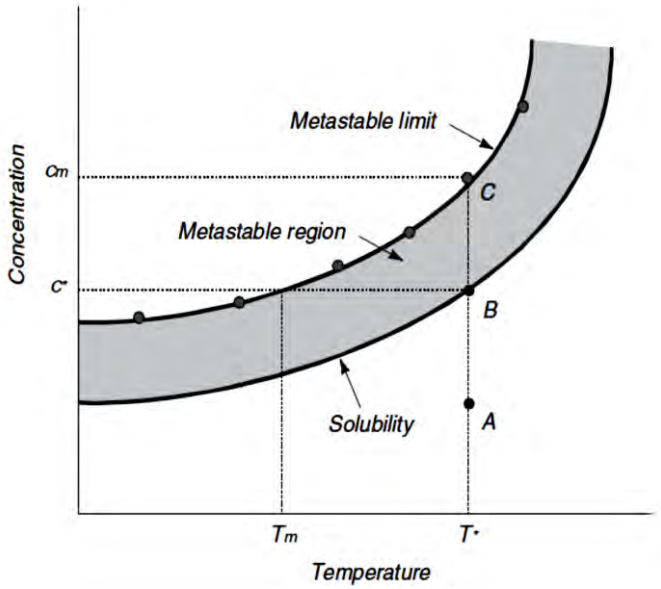

Figure 2-2. Zones of crystallization and metastability (adapted from Ulrich and Stelzer, 2011)

In Figure 2-2, line ABC represents attainment of supersaturation by evaporating the solvent and line BC^* represents attainment of supersaturation by temperature reduction. Cooling an unsaturated solution to the solubility temperature T^* causes the solution to be saturated. Further cooling below T^* results in a supersaturated solution in the metastable region. In this region, only secondary nucleation occurs by seeding with crystals of the desired product. If the solution is further cooled below the metastable limit temperature T_m, primary nucleation occurs in the labile or unstable region. The difference between the solubility temperature T^* and the metastable limit temperature T_m is referred to as the metastable zone width (MSZW). The solubility curve is a thermodynamic property of a system and the metastable limit curve

is a kinetic property which depends on the rate of cooling, types of impurities present, agitation rate and temperature level (Ulrich and Stelzer, 2011).

2.2.2 Crystal growth

After the formation of critical nuclei, the next step of crystallization is crystal growth. Crystal growth is envisaged as a layer-by-layer attachment of solute molecules on crystal surfaces (Myerson, 2002). Figure 2-3 shows three possible sites for incorporation of molecules into the crystal surface. Site A is characterized by the attachment of the molecule to a growing surface. At site B (step), the molecule attaches to both the growing surface and the step and at site C (kink), the molecule is attached at three surfaces. From an energy point of view, site C is the most favourable since the molecule attaches to a greater number of nearest neighbours. The incorporation of a molecule into a crystal surface occurs by adsorption onto the surface and diffusion along the surface to the step or kink site for incorporation into the lattice (Myerson, 2002).

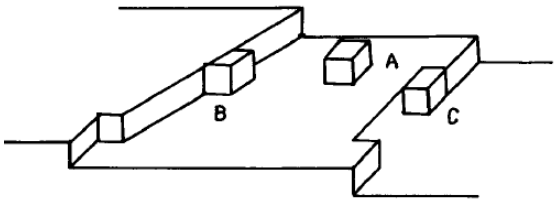

Figure 2-3. Surface structure of a growing crystal (adopted from Myerson, 2002)

Nucleation and growth rates control the final CSD. Growth and crystallizer conditions can also affect the product purity and crystal habit (Myerson, 2002). Two methods of expressing the growth rate are:

1. Change in a linear characteristic dimension of a crystal(s), that is, the rate of growth of a particular face in a direction normal to the face. This can be expressed as:

$$G_l = \frac{dL}{dt} \qquad 2\text{-}12$$

where, G_l is the linear growth rate, dL is the change in the characteristic dimension, L, that occurs in time, dt.

2. Change in crystal mass with time, known as mass growth rate. This can be expressed as:

$$G_m = \frac{dm}{dt} \qquad 2\text{-}13$$

where, G_m is the mass growth rate, dm is the change in mass, m, of crystals in suspension corresponding to a change in time, dt.

Many theories of crystal growth were proposed and one of the most common theories is the diffusion-reaction theory. As shown in Figure 2-4, the diffusion step involves diffusion of solute molecules from the bulk of the solution through the stagnant liquid film surrounding the crystal surface, and the reaction step involves the incorporation of the solute molecules onto sites of lowest Gibb's free energy, hence lattice growth.

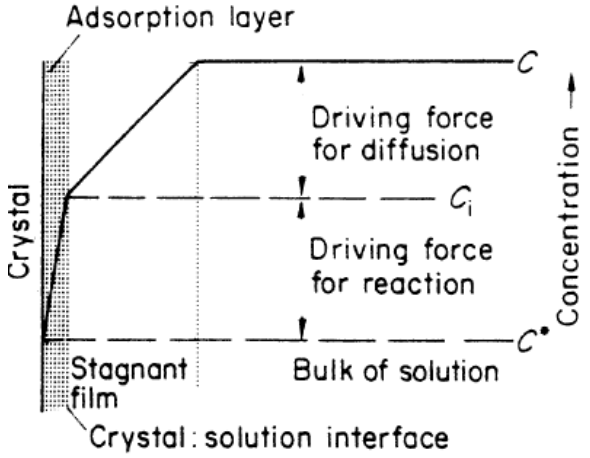

Figure 2-4. Diffusion – reaction theory of crystal growth (adopted from Mullin, 2001)

The rates of mass transfer and deposition as dictated by diffusion and surface reaction respectively are difficult to determine since this requires knowledge of the interfacial concentration, C_i. However, an expression based on overall concentration driving force ($C - C^*$) is shown in Equation 2-14:

$$\frac{dm}{dt} = K_G A_c (C - C^*)^g \qquad 2\text{-}14$$

Where $\frac{dm}{dt}$ is the mass growth rate, K_G is the overall crystal growth co-efficient and g is the exponent referred to as the order of the overall growth process. The overall growth process is diffusion limited when the surface integration step occurs faster than the molecular diffusional step. It becomes surface reaction limited when the diffusion step occurs faster than the surface reaction step.

2.3 Product characteristics

The product quality is often described in terms of the CSD and the morphology of the crystal. The former is determined by the relative rates of nucleation and primary growth as well as secondary growth processes such as aggregation, agglomeration and attrition. The latter is determined by the differential facial growth rates of the crystal surfaces. It follows that the operating conditions which dictate these rate processes, such as supersaturation, type of solvent, presence of impurities and agitation play a pivotal role in modifying final product quality.

2.3.1 Crystal Size Distribution (CSD)

CSD is a population or mass distribution expressing how the number or mass of crystals is distributed over various size ranges. In other words, it is number-based or mass-based. It has an impact on product appearance, solid-liquid separation, purity and dissolution properties (Ulrich and Stelzer, 2011). There are two types of CSDs namely the density distribution and the cumulative distribution. The former is presented in normalized form as shown in Equation 2-15 and the latter is defined as shown in Equation 2-16.

$$\int_0^\infty \mathrm{f(L)dL} = 1 \qquad 2\text{-}15$$

$$\mathrm{F(L)} = \int_0^\infty \mathrm{f(L)\,dL} \qquad 2\text{-}16$$

where, f(L)dL is the fraction of particles in the size range L to L+ dL.

A CSD is often characterized by the mean size, median size, dominant size and the co-efficient of variation (CV). The median size is the crystal size for which fifty percent of the crystals are larger or smaller, whereas the dominant size is the crystal size attained by a greater population of the crystals. The CV is a measure of the spread of the distribution and is expressed as:

$$\mathrm{CV} = \frac{\mathrm{Sd}}{\mathrm{L_D}} \qquad 2\text{-}17$$

where, Sd is the standard deviation of the distribution and L_D is the dominant size.

According to Mullin (2001) and Myerson (2002), the CSD of the product from a Mixed Suspension Mixed Product Removal (MSMPR) crystallizer is expected to have a CV of about 50 %.

2.3.2 Morphology

Morphology refers to the external appearance of the crystal. Crystal morphology depends on supersaturation, which determines the rates of nucleation and growth. It is also affected by the presence of impurities / additives, the solvent used as well as the state and degree of agitation employed (Mullin, 2001). Two crystals having the same crystal lattice may have different shapes due to influence of external conditions (Myerson, 2002). Crystal habit can affect the rheological properties of the suspension, filtration or centrifugation efficiency, bulk density of the solid and flow properties of the solid (Myerson, 2002). Control of crystal habit and crystal size distribution is therefore essential in industrial crystallization processes. Crystal habit can vary significantly with the rates of nucleation and growth. Very rapid crystallization often produces crystalline solids, which appear to be amorphous (with no faces) due to high growth rates of all faces resulting in disappearance of the faces (Myerson, 2002). Rapid crystallization often results in the formation of needle-like shapes and dendrites (Mullin, 2001).

According to Wulff's (1901) thermodynamic prediction of crystal shape (as cited by Myerson, 2002), a crystal adopts a shape that has minimum Gibb's free energy. However, kinetics play an important role in determining the morphology and crystal shapes often deviate from such predictions. Crystal shape is determined by the relative growth rates of the faces; fast growing faces become smaller than slow growing faces and eventually disappear from the crystal (Ulrich and Stelzer, 2011). Internal conditions that affect the habit of a crystal include impurity content and liquid inclusions and external factors include temperature and flow around the crystals (Patience and Rawlings, 2001). The change in the crystal form is based on a difference in the adsorption energies on different crystal faces; foreign molecules will be adsorbed preferentially on surfaces where the free adsorption energy is more negative (Al-Jibbouri and Ulrich, 2001). Shtukenberg and co-workers (2014) highlighted that impurities can also result in twisted crystals due to the presence of a permanent stress source that distorts the crystal by creation of a twist moment at the growth front.

2.4 Population balance

Quantification of nucleation and growth processes is necessary for a complete description of the CSD in a continuously operated crystallizer. Randolph and Larson (1962, 1988) (as cited by Mullin, 2001) introduced the population balance model (PBM). This is demonstrated with reference to a continuous MSMPR crystallizer assuming steady-state operation, absence of

crystals in the feed stream, uniform morphology, absence of crystal breakages and agglomeration as well as growth rate-size independence. Assuming an arbitrary size range L_1 to L_2 with population densities n_1 and n_2 respectively, the population balance equation (PBE) can be written as follows:

$$Vn_1G_1 + Q_in_i\Delta L = Vn_2G_2 + Qn\Delta L \qquad 2\text{-}18$$

where, V is the crystallizer volume, G is the growth rate of the characteristic dimension and Q is the volumetric flow rate. The terms Vn_1G_1 and Vn_2G_2 denote the number of particles entering and leaving the size range by growth, whilst $Q_in_i\Delta L$ and $Qn\Delta L$ denote the number of particles entering and leaving the size range by flow. By taking into account all the assumptions of the MSMPR reactor, introducing the mean hydraulic residence time, τ, and upon integrating, the PBE reduces to:

$$n = n_o \exp\left(-\frac{L}{G\tau}\right) \qquad 2\text{-}19$$

where, n is the crystal population density (number of crystals per unit volume per unit size), n_o is the nuclei (zero-sized particles) population density, L is the mean size of the crystals and G is the growth rate of crystals. The terms n_o and G can be evaluated from the intercept and the gradient, respectively, of a semi-logarithmic plot of the population density and size as shown in Figure 2-5. At steady- state, nucleation and growth rates will be constant.

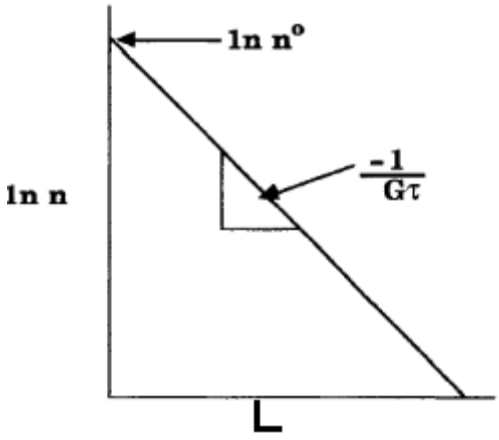

Figure 2-5. Semi-logarithmic plot of the population density versus size (adopted from Myerson, 2002)

The nucleation rate, J, which is the number of zero-sized particles per unit volume per unit time, can be evaluated as:

$$J = n^oG \qquad 2\text{-}20$$

Therefore, measurement of the CSD at steady state allows evaluation of the nucleation and growth rates using the PBE.

2.5 Theory of Eutectic Freeze Crystallization (EFC)

2.5.1 Principle of operation of EFC

EFC achieves recovery of salt and production of pure water from a brine solution by operating under sub-eutectic conditions of the salt-water system in consideration. Different salt-water systems have different eutectic compositions and temperatures. The eutectic point is defined as the concentration and temperature at which solid solvent and solid solute(s) co-exist with the solution in equilibrium. Solutions with solute concentrations lower than the eutectic concentration are termed hypoeutectic solutions and those with higher concentrations than the eutectic are termed hypereutectic solutions.

The principle of operation of EFC is best explained using a phase equilibrium diagram (PED) shown in Figure 2-6.

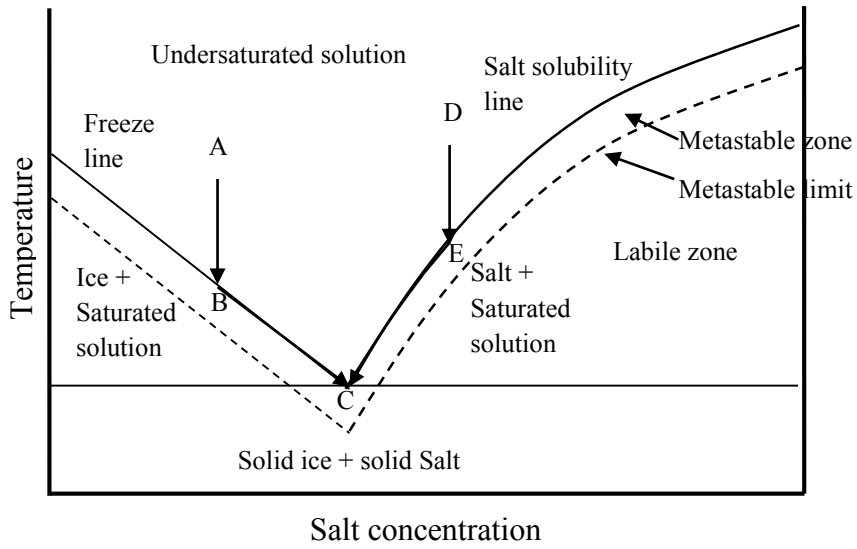

Figure 2-6. Phase equilibrium diagram of a binary system

If an undersaturated hypoeutectic solution at point A is cooled to the freeze line (representing melting temperatures of water in hypoeutectic solutions), the solution becomes saturated. Further cooling results in supersaturation, more appropriately referred to as supercooling. If the temperature is maintained within the MSZW, ice crystallization can be initiated by seeding with ice crystals. If the temperature is lowered below the metastable limit, spontaneous nucleation occurs. As ice crystallizes out of solution, the salt concentration increases thereby further depressing the melting point of water, causing the system to move towards the eutectic point (line BC). Below the eutectic point, C, salt crystallization can be

initiated within the metastable zone by seeding with salt crystals, or else spontaneous nucleation occurs in the labile zone at higher degrees of supercooling.

Likewise, cooling an undersaturated hypereutectic solution results in salt crystallization below the solubility line. This reduces the solution concentration and the system tends towards the eutectic point below which ice and salt simultaneously crystallize.

2.5.2 Na_2SO_4-H_2O phase equilibria

Figure 2-7 shows the phase equilibrium diagram of a Na_2SO_4-H_2O system over the temperature and concentration ranges shown.

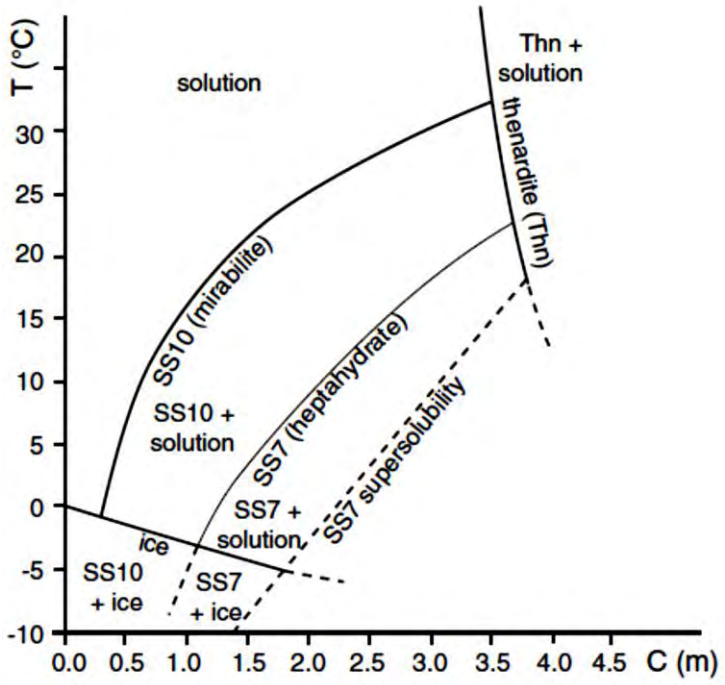

Figure 2-7. Na_2SO_4-H_2O phase equilibrium diagram showing stable (solid lines) and metastable (broken lines) phases with 'm' representing molar concentrations (adopted from Denecker et al., 2014)

Three phases of sodium sulphate crystallize at different conditions of temperature and concentration. These are mirabilite ($Na_2SO_4.10H_2O$) which is shown as 'SS10' in the diagram, sodium sulphate heptahydrate ($Na_2SO_4.7H_2O$) shown as 'SS7' and thernadite (anhydrous Na_2SO_4) labelled 'Thn'. $Na_2SO_4.10H_2O$ is the most stable phase that crystallizes at temperatures below about 32 ˚C. $Na_2SO_4.7H_2O$ crystallizes below the metastable region of $Na_2SO_4.10H_2O$. It is possible that certain impurities can induce crystallization of a less stable phase.

2.6 Ostwald ripening

The Gibbs-Thomson equation relates crystal size to equilibrium solubility as shown in Equation 2-21 (Enustun and Turkevich, 1960 as cited by Myerson, 2002).

$$\ln \frac{C^*(r)}{C^*(\infty)} = \frac{2 \propto V_m}{RTr} \qquad 2\text{-}21$$

where, $C^*(r)$ and $C^*(\infty)$ are equilibrium solubilities for spherical crystals of small radius, r, and very large radius, ∞, respectively, α is the surface energy of the solid phase, V_m is the molar volume and R is the universal gas constant. This equation shows that the equilibrium solubility increases with decreasing crystal size. It then follows that the effective supersaturation available for growth of larger crystals is higher than that available for small crystals (Myerson, 2002). Ostwald ripening is the process of equilibration by which dissolution of small crystals creates supersaturation for deposition of solute onto the surfaces of large crystals. Thus, large crystals grow at the expense of small crystals.

The driving force for Ostwald ripening is the difference in solubility between crystals of different sizes. The rate of this process depends on the CSD, growth and dissolution kinetics, diffusivity of the solute molecules through the liquid phase and viscosity of solvent. A heterogeneous system with a size distribution of the solid phase strives to attain a state of equilibrium, hence a state of lowest Gibb's free energy. The large interfacial area presented by the small particles contributes to the free energy which can be reduced by dissolution of the small crystals, thereby minimising surface area. The nett effect is to reduce the crystal population, increase the mean crystal size and increase the spread of the distribution.

2.7 Imaging technique for in-situ crystallization studies

Arellano and co-workers (2004) developed a non-intrusive technique to monitor lactose crystallization and implemented an image analysis procedure for determination of crystallization kinetics. Figure 2-8 shows the imaging set-up which consists of a glass holder containing the solution, a polarized light microscope viewed with a lens that has a magnification factor of four. Images are continuously captured at certain time intervals and these are processed using an image processing protocol, which involves background subtraction, conversion to grey scale, thresholding and generation of CSD histograms. The PBE is then used to evaluate the nucleation and growth rates from the obtained CSDs as described in section 2.4

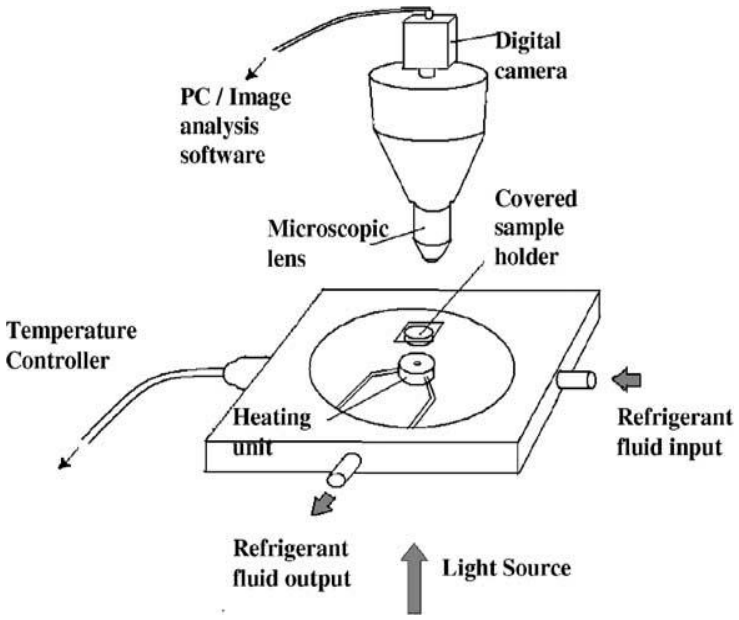

Figure 2-8. Digital imaging system (adopted from Arellano et al., 2004)

Virone and co-workers (2005) investigated the growth kinetics of attrition fragments of $(NH_4)_2SO_4$ parent crystals in a set-up which consisted of a 2L draft tube crystallizer, a glass stagnant growth cell immersed in a cooling cell connected to a thermostatic bath. The cooling cell was viewed under a microscope equipped with a camera connected to a video printer. Ferreira and co-workers (2005) used a similar set-up for morphology assessment and crystal particle classification of NaCl crystals. In this set-up, the crystals were deposited on a glass slide and observed by a transmitted light microscope with a monochrome camera connected to a computer. The images captured were processed by conversion to greyscale, hole filling, noise elimination, removal of crystals that contact the edge of the images and particle identification in the image.

Qu and co-workers (2006) used in-line image analysis to investigate the effect of additives in batch cooling crystallization of potassium dihydrogen phosphate. The set-up consisted of a particle image analysis video microscope that was inserted into the crystallizer to collect in-line images. The advantage of in-line video microscopy is that crystal breakage and attrition can also be detected. The resulting images were processed by edge detection, morphological closing and hole filling and exclusion of objects touching the image boarder.

2.8 Prediction and measurement of solubility

Measured values of solubility are more reliable than predicted values. However, due to the complexities associated with accurate measurement of solubility, use is often made of predicted data.

2.8.1 Prediction

Various solubility correlation and prediction methods exist and these range from simple interpolation or extrapolation techniques to the thermodynamic based computational techniques. Most thermodynamic approaches are based on the modified Debye-Hückel equations which require prediction of activity co-efficients, enthalpies, entropies and specific heat capacities of solutions (Mullin, 2001). The selection of a solubility prediction tool is subject to the accuracy required and the ultimate use of the data obtained.

2.8.2 Measurement

Solubility determination requires constant temperature during the course of equilibration and sampling. For substances whose solubility changes much appreciably with temperature, a greater accuracy of temperature control is required. A temperature variation of ±0.1 ˚C results in a precision of less than 0.1 % for NaCl solubility and greater than 0.1 % for Na_2SO_4 solubility. A precision of less than 1 % is however quite satisfactory for solubility measurements in most cases (Mullin, 2001). Platinum resistance temperature sensors (PT100) with an accuracy of ±0.01 ˚C are quite essential where high accuracy is desired. Agitation also plays a pivotal role in bringing solute and solvent to equilibrium. Completely sealed agitated vessels are preferred due to evaporation losses that could occur in open vessels.

The time of contact required varies from hours to days or even weeks depending on the solubility properties of the solute, the type of solvent, viscosity of solvent and the operating temperature. Gardner and Nancollas (1983) determined solubility of $BaSO_4$ in experiments that were allowed to equilibrate over a period of 3 – 70 hours. Vavouraki and Koutsoukos (2012) measured the solubility of mirabilite over an equilibration time of 24 hours and the results were in good agreement with reported values. The short equilibration time was justified by the large surface to volume ratio of mirabilite crystals. After sufficient contact time, samples of clear supernatant liquid should be collected using a pipette or syringe fitted with filtering material. The pore size of the filter is also an important parameter for better accuracy of the solubility data. It should not allow any solids to pass through. Knowledge of

the solubility of a crystallizing component enables determination of the driving force required for crystallization as well as maintaining constant supersaturation (Myerson, 2002).

2.9 Freezing Point Depression (FPD) calculation

According to Atkins and Clugston (1982) (as cited by Uba and Saeed, 2008), the FPD is a function of molar solute concentration. In other words, it is a colligative property (Atkins and Paula, 2014) which is expressed as in equation 2-22.

$$FPD = vE_f m_2 \qquad 2\text{-}22$$

where, v is the ionization factor, m_2 is the molality (moles solute per kg solvent) and E_f is the Cryoscopic Constant, a characteristic property of the solvent, which is calculated using equation 2-23 (Lide, 2005).

$$E_f = \frac{RT_f^2 M_r}{\Delta_{fus}H} \qquad 2\text{-}23$$

where, R is the molar gas constant, T_f is the absolute freezing point temperature of the solvent, M_r is the molar mass of the solvent, and $\Delta_{fus}H$ is the molar enthalpy of fusion of the solvent.

The Cryoscopic Constant for water is 1.86 (Lide, 2005).

2.10 Additives and / or impurities

Foreign substances in solution can either be tailor made additives dosed deliberately to improve the process kinetics and the product quality, or they can be impurities entrained from upstream unit operations. The subject of this research is on antiscalants that are dosed in RO feed streams. These emerge as contaminants in the brine retentate stream, which can be treated using EFC.

An impurity is defined as any foreign substance in the solution other than the desired crystallizing compound. An additive is defined as a deliberately added impurity and the term admixture refers to an impurity added in large amounts. An impurity that decelerates growth of crystals is termed a poison or inhibitor and an impurity that accelerates growth of crystals is termed a promoter (Sangwal, 2007). Some inhibitor molecules have the capacity to adsorb on all crystal faces, decreasing the crystallization rates to zero implying nucleation inhibition (Ruiz-Agudo et al., 2006). Immobile impurities retard the growth of a step and become incorporated into the crystal lattice, whereas mobile impurities can move further away as the step advances (Myerson, 2002).

Additives can have a thermodynamic effect (effect on solubility) and a kinetic effect (effect on nucleation and growth rates). Additive molecules can alter the solute ion activity through formation of other chemical species with the solute molecules. Impurities can alter growth by blocking or promoting the adsorption and movement of solute molecules on the crystal surface, attachment or detachment of solute molecules at kink sites and incorporation of solute molecules into the crystal lattice. The greatest impact on growth rate occurs when spiral growth mechanism is dominant. Subsequent deposition of growth layers can result in incorporation of the additive molecules in the crystal lattice. If an impurity is present in considerably huge amounts in a binary system, its effect can be assessed in terms of a ternary PED (Mullin, 2001). Veintemillas-Verdaquer (1996) pointed out that, at low concentrations, the effect of impurities is greater on the crystal surface properties than on the bulk properties.

2.10.1 Proposed mechanisms for crystal growth inhibition

Four models have been proposed by which additive molecules modify growth of solute crystals (De Yoreo and Velikov, 2003). These models predict that the presence of impurities in solution reduces the growth rates (Rauls et al., 2000; Al-Jibbouri and Ulrich, 2001).

2.10.1.1 Cabrera-Vermilyea model (step pinning)

Cabrera and Vermilyea (1958) (as cited by Myerson, 2002) proposed that if an immobile impurity blocks a growing step, the step front will try to squeeze through the space between adjacent impurity molecules resulting in a curved step edge with radius of curvature. The step will continue to advance if the average spacing between a pair of impurities is greater than $2r_c$ where r_c is the critical radius of curvature, otherwise step growth is completely inhibited. Advancement of a step past the impurity molecules will alter its characteristic shape and proceeds at a lower velocity than that in a pure solution. The critical radius of curvature below which growth stops is referred to as the dead zone and the supersaturation at which a step reaches its r_c is termed the width of the dead zone. The width of the dead zone varies with impurity concentration. This model shows that the step velocity is reduced by an amount, which is proportional to the concentration of the adsorbed impurities on terraces.

2.10.1.2 Incorporation

Incorporation of additive molecules on kinks or growing steps within the crystal lattice can either inhibit or promote growth. It also results in solid solutions, which have either lower or higher solubility than the pure crystal (Shtukenberg et al., 2014). Inhibition is characterized by the increase in solute ion activity and unchanged kinetic co-efficient associated with

molecular attachment. This implies that the kinetics of the attachment process remains constant.

2.10.1.3 Bliznakov model (kink blocking)

Some impurity molecules block kink sites temporarily resulting in the reduction of available kink sites. A dead zone is not created and therefore solubility is not changed. The attachment kinetic co-efficient is however changed due to reduced kink sites.

2.10.1.4 Surfaction

Impurities can act as surfactants and enhance growth kinetics either thermodynamically by lowering the step edge free energy, or kinetically by reducing the activation energy of attachment. A change in step morphology can thus occur without a change in step velocity and this is attributed entirely to a thermodynamic effect where the directional dependence of the step free energy is modified.

2.10.2 Antiscalants

Antiscalants are chemical compounds that prevent the precipitation of sparingly soluble salts, hence scale formation on heat exchange surfaces or membrane surfaces. Common problematic salts include calcium carbonate, magnesium sulphate, calcium sulphate, barium sulphate and strontium sulphate. The composition of commercial antiscalants is proprietary.

However, antiscalants fall into any of these categories or blends of these categories namely: phosphates, phosphonates, carboxylates, acrylates and sulphonates. Phosphonates are amongst the most common crystallization inhibitors (Ruiz-Agudo et al., 2006; Weijnen et al., 1983) widely used in various industrial sectors due their excellent inhibition effect. They are highly efficient in preventing the nucleation and crystallization of many sparingly soluble inorganic salts, as well as having high stability even at relatively high temperatures and harsh conditions (Liu et al., (1975) as cited by Akyol et al., 2009). Gardner and Nancollas (1983) observed that phosphonic acids were excellent inhibitors even at 125 °C. Moreover, they are capable of simultaneously forming covalent bonds with cations and hydrogen bonds with anions on the crystal surface (Veintemillas-Verdaquer, 1996). Weijenen and van Rosmalen (1986) demonstrated that phosphonates are highly active if a significant proportion of the phosphonic groups exist as PO_3^{2-} as shown in Figure 2-9.

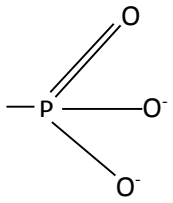

Figure 2-9. Phosphonate anionic group

The P-C bond in phosphonic acid derivatives does not readily oxidize or hydrolyse due to its high stability. Consequently, many reactions can occur on the organic part of the molecule. Antiscalants exhibit their effects by adsorption on nuclei surfaces thereby blocking growth sites. Antiscalants can affect different stages of nuclei formation and growth.

Antiscalants can reduce scale formation by different mechanisms namely: threshold inhibition, crystal distortion, dispersion and sequestration. Threshold inhibition occurs when the antiscalant acts on the nucleation stage by inhibiting the ordering of proto-nuclei thus preventing nucleation. This occurs by adsorption of antiscalant molecules on sub-microscopic entities. Phosphonic acids can prevent precipitation of sparingly soluble salts by threshold inhibition when added in sub-stoichiometric quantities (Svara et al., 1995). Crystal distortion occurs by the selective adsorption of antiscalant molecules on nuclei surfaces causing different facial growth rates, thereby distorting the shape and reducing the resulting scale hardness.

Dispersion occurs by the adsorption of antiscalant molecules on nuclei surfaces causing electrical repulsion that keeps the particles in suspension, thus preventing them from adhering to each other and to the surfaces. Sequestration occurs by formation of soluble and stable complex compounds with the metal ions in solution. Additives exhibiting this behaviour are called chelating or sequestering agents. An example is ethylenediaminetetraacetic acid (EDTA). Several di- or polyphosphonic acids are capable of sequestering polyvalent cations (Svara et al., 1995).

3 Literature review

In this chapter, a review of literature on the evolution of EFC as well as the design and development of EFC crystallizers and processes is presented. Literature on the effect of antiscalants on crystallization thermodynamics and kinetics is presented in two main parts. The first part is an extensive review on the effect of impurities, in particular antiscalants, on salt solubility as well as nucleation and growth rates of various salts during crystallization processes. The review extends to the effect of antiscalants on CSD and morphology since these quality parameters are dictated by the crystallization kinetics. The second part is on the effect of impurities on ice kinetics with emphasis on similar parameters as outlined for salt. To the best of the authors' knowledge, only literature on effect of ionic impurities during EFC is available. Most of the literature presented in this section is pertinent to evaporative, cooling and freeze crystallization. Following a critical synthesis of previous findings from a pool of researchers, the gap is identified and the research aim, objectives, hypothesis and questions are laid out.

3.1 Evolution of EFC

Eutectic Freeze Crystallization (EFC) started in the 1950s when Nelson and Thompson attempted to determine the order of crystallization of salts (as cited by Vaessen, 2003). Stepakoff and co-workers (1974) proposed a continuous EFC process for the treatment of brines (KCl and NaCl) in which direct cooling was used and it was concluded that both ice and salt could be separated from their binary solutions. In direct cooling, an inert cooling fluid is injected into the solution and vaporizes at the desired temperature by withdrawing its heat of vaporization from the solution. The drawbacks of this process were production of impure crystals and presence of the cooling fluid in all equipment including solid / solid separator, filters, wash column and pumps. For these reasons, the idea was abandoned. Swenne (1983) (as cited by Vaessen, 2003) investigated EFC of NaCl using direct cooling. The economic feasibility of this process was proven but the process never reached industrial scale.

Due to stricter wastewater regulations and concerns for energy consumption, van der Ham (1998) rekindled research in EFC by investigating the recovery of $NaNO_3$ and $CuSO_4$ in an indirect cooled crystallizer: the Cooling Disk Column Crystallizer (CDCC). In the CDCC, heat is removed through cooled disks mounted on a vertical axis in the column. The disks

have orifices to permit flow of crystals from one compartment to the other. To prevent scaling, the disks are equipped with scrapers which also provide mixing. In comparison to conventional three stage evaporative crystallization, energy reductions of up to 70 % can be achieved (van der Ham, 1998). Vaessen (2003) scaled up the process to a 100 L Scrapped Cooled Wall Crystallizer (SCWC). Genceli (2008) scaled up the process to 220 L using a skid mounted third generation CDCC. Research continued in areas such as the physical aspects of heat transfer (Rodriguez-Pascual, 2009). Current and on-going research in EFC involves investigations into the recovery of two pure salts in a continuous process and the effect of impurities on crystallization kinetics.

This technology has shown potential to be an attractive alternative to conventional treatment of wastewaters produced from the mining industries and has been shown to have lower energy consumption than conventional evaporative processes (van der Ham, 1999; Vaessen, 2003; Genceli, 2008). It has become desirable to investigate the effect of additives on salt and ice crystallization in EFC.

3.2 Crystallization kinetics of sodium sulphate

Vavouraki and Koutsoukos (2012) determined the growth kinetics of $Na_2SO_4.10H_2O$ at different relative supersaturation levels in the range 0.18 to 0.66 and constant temperatures of 18 ˚C and 20 ˚C using cooling crystallization and precipitation reaction. It was observed from both methods that the growth rate had a parabolic dependence on relative supersaturation at low relative supersaturation levels below about 0.25, after which the dependence became linear. This is in agreement with the prediction of the Burton-Cabrera-Frank (BCF) model of spiral growth suggesting surface diffusion or integration controlled growth kinetics (Myerson, 2002). The higher temperature yielded higher growth rates and this was confirmed by lower calculated interfacial surface energy. A change in morphology was also observed at different temperatures showing that temperature has an effect on surface integration kinetics.

3.3 Effect of impurities on salt crystallization

Organic phosphonic acids are the most widely used crystallization inhibitors and can drastically increase the solubility of sparingly soluble salts. In a study of $CaCO_3$ precipitation inhibitors conducted by He and co-workers (1997), phosphonates were found to be the best inhibitors. When an impurity molecule reaches the surface of a growing crystal, it undergoes surface adsorption, followed by surface diffusion and then adsorption at the active sites (Sangwal, 1999). Weijnen and co-workers (1983) highlighted that a phosphonate surface

coverage of 5 % is sufficient to completely inhibit crystal growth implying adsorption preferably at kink sites. They suggest that this is due to the co-ordination of surface cations by phosphonate ions and possibly hydrogen bond formation between additive molecular constituents, such as, -OH and -NH_2 groups, with surface anions. Similar molecules can have different effects on the crystallization behaviour of particular salts and this is largely due to their different adsorption free energies (Rauls et al., 2000). According to Al-Jibbouri and Ulrich (2001), impurities can have a thermodynamic effect where the solubility of the crystallizing species is altered and a kinetic effect where the nucleation and growth rates are altered. Consequently, modification of the CSD and morphology is expected.

3.3.1 Effect of impurities on salt solubility

Additives always lead to a change in the solubility of the solute and the solute-fluid interfacial energy (γ). Factors affecting solubility include the presence of foreign and / or common ions, pH, temperature and the presence of chelating agents (Sangwal, 2007). According to Mullin (2001), trace impurities can sometimes have highly unexpected effects on equilibrium solubility. A change in solubility implies that the supersaturation required for crystallization or rather the change in solubility must be correctly determined for accurate evaluation of crystallization kinetics.

Ruiz-Agudo and co-workers (2006) investigated the effect of three common phosphonic acid inhibitors on $Na_2SO_4.10H_2O$ in evaporative crystallization from an aqueous solution. These include 1-hydroxyethylidene-1,1-diphosphonic acid (HEDP), aminotris-methylene phosphonic acid (ATMP) and diethylenetriaminepentakis-methylene phosphonic acid (DTPMP). The authors observed that $Na_2SO_4.10H_2O$ crystallization in the presence of additive concentrations of 10^{-2}, 10^{-3} and 10^{-4} M occurred at a relatively lower critical supersaturation than in the control solution at the natural pH of a saturated Na_2SO_4 solution of ca. 6.4. It can be inferred that this was due to an increase in Na_2SO_4 solubility whilst maintaining a constant initial feed concentration.

Reddy and co-workers (2010) investigated the effect of various ionic impurities (F^-, Cl^-, K^+, Li^+, Mg^{2+}, Ca^{2+}, NO_3^- and NH_4^+) on $Na_2SO_4.10H_2O$ crystallization. Low concentrations of these impurities, between 0.0001 and 0.012 moles per kg, lowered the eutectic point of the $Na_2SO_4.10H_2O$ system from -1.24 ˚C to -2.22 ˚C. This shows an increase in the solubility of Na_2SO_4 in the presence of impurities. However, in the presence of 0.06 moles per kg NaCl,

the nucleation temperature of $Na_2SO_4.10H_2O$ increased, hence a reduction in solubility and this was attributed to the common ion effect. At the same time, presence of high concentration of NaCl, about 2 moles per kg, had a strong freezing point depression (FPD) effect such that the overall effect was to reduce the eutectic temperature to -21.22 °C. Marliacy and co-workers (2000) obtained similar results in which addition of NaCl decreased $Na_2SO_4.10H_2O$ solubility and this was ascribed to the common ion effect. The solubility of a compound may increase or decrease with increasing additive concentration depending on the properties of the additive; the presence of common ions leads to a reduction in solubility whereas the presence of foreign ions and complex formation increase the solubility (Sangwal, 2007; Mullin, 2001).

Selwitz and Doehne (2002) highlighted that phosphonic acids have little effect on the solubility of highly soluble salts. The authors found that 0.1 – 1 wt. % of potassium ferrocynide ($K_4Fe(CN)_6.3H_2O$) increased the solubility of NaCl by 25 – 30 %. Rauls and co-workers (2000) investigated the effect of Al^{3+} and two azo dyes, amaranth and fuchsine, on $(NH_4)_2SO_4$ crystallization behaviour, in an MSMPR crystallizer. The impurity concentrations ranged from 1 to 500 ppm. It was found that the supersaturation increased almost proportionally with impurity concentration. This corresponds to a reduction in solubility. The authors suggest that this was due to reduction in the specific surface of crystals owing to changes in crystal shape and size.

Al-Jibbouri and Ulrich (2001) investigated the effect of $MgCl_2$, $PbCl_2$, $K_4Fe(CN)_6.3H_2O$ and $CuSO_4.5H_2O$ on NaCl crystallization. The maximum impurity concentration investigated is 250 ppm. The first three impurities reduced NaCl solubility in proportion to the impurity concentration and this manifested as an increase in nucleation temperature and / or reduction in dissolution rate. $CuSO_4.5H_2O$ did not have a notable effect on NaCl solubility. According to the authors, reduction in solubility often leads to an apparent increase in growth rates if crystallization temperature is maintained constant due to increased supersaturation. Therefore, in order to determine the effect of impurities on crystallization kinetics, the crystallization temperature has to be adjusted accordingly to maintain constant supersaturation.

3.3.2 Effect of impurities on crystallization kinetics of solute(s)

The nucleation rate plays a pivotal role in simulation of crystallization processes (Liu et al., 2004). Presence of impurities can either enhance heterogeneous nucleation (Veintemillas-Verdaquer, 1996) since the impurity particles can act as heteronuclei or inhibit nucleation if the active sites on growing nuclei are blocked by the impurity molecules (Rauls et al., 2000). The major setback in optimizing crystallizer design and operation is unavailability of reliable kinetic data (Liu et al., 2004). According to Akyol and co-workers (2009), measurement of induction time is an acceptable method of determining the effect of additives on nucleation. However, it is quite possible that an increase in induction time can result in a higher nuclei population density due to the higher supersaturation required for nucleation. Ruiz-Agudo and co-workers (2006) noted that ATMP and DTPMP additives in concentrations of 10^{-4} to 10^{-2} M increased the nuclei population density of $Na_2SO_4.10H_2O$ crystals despite the increase in induction time. The authors attributed this effect to heterogeneous nucleation of $Na_2SO_4.10H_2O$ on the phosphonate template formed by adsorption of additive molecules on the Si-OH glass substrate. Growth promotion was observed at a neutral pH although there was no clear trend with increasing antiscalant concentration. It was also observed that a rise in pH up to 8 – 8.5 increased the crystallization inhibition capacity to a maximum beyond which it diminished. The increased inhibition capacity was attributed to increased electrostatic attraction forces between the additive molecules and the crystal surface cations, due to deprotonation of phosphonate groups as pH increased. This reduced the available kink sites for solute molecular attachment. This shows that pH plays an important role in modifying the interactions between additive and crystal surface molecules. They also observed that the number of phosphonate groups does not dictate the extent to which Na_2SO_4 crystallization is inhibited since ATMP which has three groups had a greater effect than DTPMP which has five groups at pH of 8 – 8.5.

Shih and co-workers (2004) investigated the effect of five commercial antiscalants of different proprietary compositions on $CaSO_4.2H_2O$ crystallization. Similarly, an increase in additive concentration between 0.25 and 3 ppm increased the induction time and the phosphino-carboxylic acid blend antiscalant had the greatest effect. However, the authors did not investigate on nucleation kinetics. A lower molecular weight polyacrylic acid antiscalant had a greater effect than a higher molecular weight polyacrylic acid antiscalant. However, an explanation for this could not be found since details of the molecular structures of the polyacrylic acid constituents of the two antiscalants were not provided. According to Rauls

and co-workers (2000), nucleation rates are reduced by blocking of active growth sites on nuclei surfaces. Kinetic data shows that the growth rate of salts is significantly reduced by many scale inhibitors (Weijnen and van Rosmalen, 1984, as cited by Black et al., 1991). Trace impurities can reduce the growth rate of a crystal significantly (Al-Jibbouri and Ulrich, 2001).

Gardner and Nancollas (1983) investigated the effect of nitrilo-trimethylene phosphonic acid (NTMP) on $BaSO_4$ growth at 125 ˚C. They observed that at NTMP concentrations of the order of 10^{-7} to 10^{-6} M, the growth of $BaSO_4$ was inhibited and the effect was greater for higher additive concentrations. To further support this, Leung and Nancollas (1978) found that $BaSO_4$ crystal growth is completely inhibited with only a 4.5 % surface coverage of NTMP on $BaSO_4$. In-situ crystallization experiments measuring growth rates along different crystallographic directions are necessary to investigate the effect of additives on crystal growth at a molecular level (Shtukenberg et al., 2014).

Weijnen and co-workers (1983) investigated the effect of HEDP on $CaSO_4.2H_2O$ growth rate. At an HEDP concentration of 10^{-7} M, there was no change in the growth rate, but at concentrations of the order of 10^{-5} M, almost complete inhibition was observed. This substantiates the fact that phosphonates are excellent inhibitors even at very low concentrations. The effectiveness of the additive decreased with increasing supersaturation, therefore low supersaturations are required to determine the effect of impurities on kinetics. At acidic pH values and HEDP concentration of 10^{-6} M, no inhibition occurred whilst at alkaline pH values, growth retardation was observed. This dependence of phosphonate inhibition efficiency on pH was observed by Black and co-workers (1991) for $BaSO_4$ and Ruiz-Agudo and co-workers (2006) for $Na_2SO_4.10H_2O$. This is attributed to full dissociation or deprotonation of phosphonate groups, PO_3^{2-}. Adsorption surface coverage of HEDP on $CaSO_4.2H_2O$ crystals, as determined by X-ray Photoelectron Spectroscopy (XPS) increased with increasing additive concentration and pH in the ranges 10^{-6} – 10^{-4} M and 5 – 9 respectively.

In an investigation by Akyol and co-workers (2009) to determine the effect of four tetraphosphonate additives in concentrations of the order of 10^{-7} M on $CaSO_4.2H_2O$ crystallization, all additives increased the induction time significantly (Liu and Nancollas, 1973) and retarded growth slightly. The increase in induction time was proven to be a result of an increase in the crystal-liquid interfacial energy in the presence of additives. Slight

retardation of growth was attributed to temporary adsorption and desorption of additive molecules, thus freeing growth sites that were initially unavailable. Interestingly, the inhibitory efficiency increased with increase in the number of methylene groups between the nitrogen atoms bonded to the phosphonate group moieties. The authors suggested that longer chain additive molecules are capable of both short and long range interactions with surface Ca^{2+} ions. It was also confirmed by XRD that the additive molecules formed complex compounds by chelating Ca^{2+} ions.

Liu and Nancollas (1973) suggest that, at minute additive concentrations of the order of 10^{-4} to 10^{-7} moles / litre, the chelation mechanism can be ruled out and inhibition is most likely due to adsorption. In a similar study, they showed that HEDP had no effect on $CaSO_4.2H_2O$ growth, whilst NTMP caused growth inhibition. However, at NTMP concentrations between 10^{-5} and 10^{-4} M, increase in NTMP concentration increased the growth rate even though the reaction constants were lower than those obtained for the pure solution. This was attributed to adsorption of additive molecules or their complexes which served as active sites for further growth. It is not quite clear whether the growth promotion was a reversal or turning point on the effect of the additive. They also observed that the size and quantity of seed crystals can influence the effect of additives due to the number of growth sites available.

Rauls and co-workers (2000) found that the presence of Al^{3+} caused the nucleation rate of $(NH_4)_2SO_4$ to pass through a minimum, at an Al^{3+} concentration of 50 ppm, beyond which it increased gradually. It was also observed that the growth rate passed through a maximum, after which it dwindled with increasing impurity concentration despite the corresponding increase in supersaturation. However, the apparent increase in growth rate at low additive concentrations was attributed to an increase in supersaturation observed with increase in additive concentration. At higher additive concentrations, the surface coverage of crystals by foreign molecules increases thereby retarding growth kinetics. The authors observed that the threshold additive concentration beyond which its effect is reversed from growth promotion to growth poisoning is in the range of 1 – 1000 ppm. Upon correcting for the effect of supersaturation, it was concluded that the growth rate decreased with increasing additive concentration. This suggests growth inhibition by adsorption of impurity entities on the active sites of the crystal surface. In addition, inclusion of impurities was observed beyond threshold impurity concentrations resulting in purity reduction. Interestingly, the authors noted that the dominant growth mechanism can change at different operating temperatures

with possibility of changing the number of active sites available on the crystal surface, hence modified impurity-crystal interactions.

Yang and co-workers (2012) investigated the effect of L-valine impurity in the concentration range of 0 – 0.1 wt. % on growth of L-alanine {011} and {120} faces. It was observed that growth retardation and almost complete inhibition occurred on the faces respectively at an impurity concentration of about 0.02 wt. %. Molecular dynamic simulations proved that the total surface energies in the presence of L-valine were higher, thereby slowing the surface adsorption and subsequent incorporation of L-alanine on crystal surfaces. Interestingly, the adsorption energies of L-valine molecules were lower than those of L-alanine molecules implying that adsorption of impurity molecules was more favoured. The surface energies of the {120} face were found to be higher than those of the {011} face showing that impurity molecules could adsorb preferentially on {120} faces, there by retarding growth.

In another investigation, Yang and co-workers (2013) observed a turning point at an L-valine concentration of 0.2 wt. % below which growth of the {011} face of L-alanine was retarded and above which growth promotion of that face occurred. Growth retardation was attributed to impurity adsorption on this face as suggested by the Cabrera-Vermilyea (C-V) model of growth inhibition. The growth promotion was explained in terms of the effect of solvent on molecular surface diffusion. Through molecular dynamic simulation, it was shown that surface diffusion was limited by the solvent in the liquid-solid interface. With increase in impurity concentration, the L-valine and L-alanine molecules became close enough such that the water molecules were repelled, thereby reducing the surface diffusion resistance.

Al-Jibbouri and Ulrich (2001) obtained first order growth kinetics for NaCl implying a diffusion-controlled process in the absence of impurities. They observed that the presence of impurities led to the reaction step playing an important role. The authors noted a reduction in the growth rate of NaCl in the presence of impurities and the effect increased with impurity concentration. Vavouraki and Koutsoukos (2012) suggested use of adsorptive compounds to control $Na_2SO_4.10H_2O$ kinetics by altering surface integration kinetics. Veintemillas-Verdaquer (1996) highlighted that changes in temperature and pressure or the presence of other impurities can alter the effect of an impurity. This warrants the investigation on the effect of antiscalants in EFC at sub-zero temperatures.

3.3.3 Effect of impurities on CSD, morphology and polymorph of salt(s)

Ruiz-Agudo and co-workers (2006) observed that the presence of ATMP and DTPMP at moderately alkaline pH values resulted in the overdevelopment of $Na_2SO_4.10H_2O$ {100} faces, thereby altering morphology. Molecular modelling showed structural matching between these additive molecules and the $Na_2SO_4.10H_2O$ {100} faces. This leads to preferential adsorption on specific crystal surfaces. On the contrary, HEDP did not cause any morphological changes. At an acidic pH of 3.4, addition of 10^{-3} M DTPMP induced crystallization of thin needle crystals of thernadite (Na_2SO_4) implying that crystallization occurred at high supersaturation. In an investigation by Reddy and co-workers (2010), the morphology of $Na_2SO_4.10H_2O$ did not change in the presence of various ionic impurities and was prismatic and monoclinic. The crystal sizes ranged from 50 to 350 μm after 150 minutes of batch EFC experiments in the presence of F^-, Cl^-, K^+, Li^+, Mg^{2+}, Ca^{2+}, NO_3^- and NH_4^+ and 50 to 400 μm in the presence of high NaCl concentration. This confirms growth promotion due to the common ion effect.

Black and co-workers (1991) investigated the effect of sulphonates, carboxylates and phosphonates on $BaSO_4$ and $CaSO_4.2H_2O$ morphology. Only phosphonates with at least two functional groups linked by a three atom chain, such as ATMP, showed some effects. Upon increasing the concentration of dimethylene diphosphonic acid from 0.024 mM to 0.096 mM, the morphology of $BaSO_4$ changed from rhombic plates to discs. It was also noted that the phosphonates did not cause any morphological changes at lower pH values below 5 possibly due to protonation. This suggests that the effectiveness of the inhibitors depends on their degree of deprotonation as observed by Ruiz-Agudo and co-workers (2006). Stereochemical matching and geometry have also been attributed to this phenomenon since these can diminish the growth rate by substitution of surface atoms or ions by inhibitor molecules. The morphology of $CaSO_4.2H_2O$ changed from needle to plate-like crystals. The authors suggest that hydrogen bonding between surface hydration water molecules of $CaSO_4.2H_2O$ and inhibitor molecules could play a role in changing the morphology. Formation of hydrogen bonds was validated by Yang and co-workers (2013) via molecular dynamic simulation.

In another investigation conducted by Gardner and Nancollas (1983), the morphology of $BaSO_4$ crystals was modified in the presence of NTMP. Shtukenberg and co-workers (2014) highlighted that the internal stress generated by the crystal compositional inhomogeneity can result in non-crystallographic curved morphologies. In a research conducted by Rauls and co-workers (2000), the presence of Al^{3+} modified $(NH_4)_2SO_4$ morphology from well-defined

tetrahedral prismatic structures to elongated rods. This was attributed to the tendency of impurity molecules to adsorb on crystal faces where the adsorption free energy is more negative (Al-Jibbouri and Ulrich, 2001). Poornachary and co-workers (2008) attributes habit modification to disruption of incorporation of solute molecules onto crystal surfaces by adsorption of impurity molecules on these surfaces. Poornachary and co-workers (2008) highlight that the incorporation of solute molecules becomes less favourable due to modified attachment energies as a result of adsorption of impurity molecules. This often leads to void formation as the step strives to progress over the poisoned surface.

Akyol and co-workers (2009) observed that the presence of four tetraphosphonates resulted in less elongated needles and platelets of $CaSO_4.2H_2O$ of smaller mean crystal sizes. In an investigation by Liu and Nancollas (1973), the presence of NTMP in concentrations of the order of 10^{-6} – 10^{-7} M resulted in smaller $CaSO_4.2H_2O$ crystals grown over a month in comparison to those grown in five hours from the pure solution. The aspect ratio of the plate-like crystals dwindled significantly proving that additive molecules adsorb selectively on different crystal faces. Tailor made additives modify habit predictably owing to their structural similarity to the crystallizing unit; they are adsorbed at preselected crystal faces thus hindering deposition of incoming solute molecules resulting in reduced growth rates and surface enlargement of affected faces – a change in morphology (Ulrich and Stelzer, 2011; Myerson, 2002). Weissbuch and co-workers (1991) suggested that in systems that display polymorphism, additives can selectively interact with the more stable phase resulting in the crystallization of the less stable phase.

3.4 Effect of impurities on ice crystallization

Little information is available in literature on the effect of impurities, particularly antiscalants and related compounds, on ice crystallization in EFC. Available literature is based on research carried out for freeze concentration processes. However, deductions and inferences are made from the available literature and related to eutectic freeze crystallization.

3.4.1 Effect of impurities on the freezing point of water

Arai and co-workers (1984) found that 5 % wt. of gelatin and gelatin hydrolysate added to pure water in the presence of the ice nucleation inducer, AgI, caused ice to nucleate at - 4 ˚C whereas an ester derivative of gelatin resulted in an ice nucleation temperature of -7 ˚C. Molecular modelling showed that the additive molecules were capable of binding on ice

surfaces via hydrogen bonds. It can be inferred that similar molecular interactions can enhance the freezing point depression effect in aqueous electrolyte systems.

3.4.2 Effect of impurities on crystallization kinetics of ice

Damodaran (2007) investigated the effect of gelatin hydrolysate on ice crystallization kinetics in ice cream using optical microscopy. It was observed that gelatin polypeptides with molar weights less than 4,000 Daltons (Da) had a greater inhibitory effect that those with higher molar weights above 7,000 Daltons (Da). Molecular modelling showed that the gelatin peptide molecules had oxygen-oxygen distances which were similar to the oxygen-oxygen distances in the ice nuclei. Therefore, it was concluded that hydrogen bonding between these additive molecules and water molecules in ice was responsible for growth inhibition. The poor inhibitory efficiency of higher molecular weight additives was attributed to steric hindrance offered by the longer molecular chains which would prevent full coverage of active growth sites.

Omran and King (1974) studied ice crystallization from sucrose, glucose and fructose solutions as well as in the presence of pectin and gelatin additives using the thermal-time response technique in a batch crystallization cell. It was found that the nucleation rate of ice increased with increase in sucrose concentration in the range 0 – 45 wt. %. Addition of pectin and gelatin additives in concentrations up to 10,000 mg/L resulted in reduction in the ice nucleation rate and the effect increased with increasing additive concentration. At an impurity concentration of about 5,000 mg/L, the effect levelled off. According to the authors, additives which alter surface properties of crystals can alter the nucleation rate.

In an investigation by Huige (1972), the growth rates of ice crystals in both dextrose and sucrose solutions diminished with increasing solute concentration, hence a decrease in the mean equivalent spherical diameter. The surface reaction constant was found to decrease exponentially with increasing dextrose concentration and this was attributed to adsorption of dextrose molecules on the ice surfaces as well as boundary layer interactions between dextrose and water molecules. This probably slowed down the surface incorporation step implying a change in the growth mechanism. According to Huige (1972), additives can affect the secondary nucleation rate by changing the crystal growth mechanism or by blocking growth sites.

Melia and Mottiff (1964) observed an increase in the secondary nucleation rate of NaCl due to the growth of dendritic crystals in the presence of potassium ferrocyanide and sodium

nitroprusside, suggesting a change in the growth mechanism. Coverage of growth sites results in concentration of solute molecules around the crystal surfaces due to lower surface reaction kinetics and diffusion of solute molecules. This increases local supersaturation which is consumed by formation of crystal nuclei, hence an increase in nucleation rate (as cited by Huige, 1972). Crystallization is a very selective process which rejects impurities owing to the high purities obtained (Omran and King, 1974).

Michaels and co-workers (1966) investigated the effect of ionic impurities (NaCl, CsF, CsI, NH_4F, NH_4I), surfactants and water soluble polymers on ice growth kinetics and morphology. The concentrations of the ionic impurities were of the order of 10^{-4} M and those of the surfactants and water soluble polymers were 0.1 wt. %. All impurities had no effect at low supercooling between 0.03 – 0.07 ˚C, but growth promotion was observed for the first four impurities at high supercooling between 0.07 – 0.15 ˚C. NH_4I had a significant growth reduction effect in the whole range of supercooling levels tested. The surfactants investigated promoted growth at higher supercooling. Polyacrylic acid, which is a constituent of some commercial antiscalants, caused a substantial reduction in the ice growth rate for all supercooling levels.

3.4.3 Effect of impurities on CSD and morphology of ice

Ice crystals grown from pure water exhibit growth anisotropy since the growth rate in the a-axis is much higher than that in the c-axis. This results in either disk-shaped or hexagonal platelets (Huige, 1972; Margolis et al., 1971). The morphology of ice crystals depends on various factors which include supercooling, concentration of solution, type and concentration of impurities present as well as the prevalent hydrodynamic conditions (Huige, 1972). The prevalent heat and mass transfer conditions during ice crystal growth determines the final product morphology with a propensity towards thin hexagonal platelets (Michaels et al., 1966).

Huige (1972) investigated the growth of ice crystals in pure water, dextrose and sucrose solutions. Ice crystals grown from pure water and dextrose solutions were almost spherical and disk-shaped respectively. The author attributed the difference in the shape to the low supercooling, of 0.005 ˚C, at which ice nucleates from pure water. The disk shapes had an average height to diameter ratio of 0.26 and this increased to 0.33 – 0.5 in sucrose solutions implying that the sucrose molecules selectively adsorbed and impeded growth of the crystal face normal to the basal plane. The growth rate was enhanced in the presence of low dextrose

concentration and this was attributed to either reduction of interfacial energy or an increase in growth sites as a result of adsorption of dextrose molecules on the ice surface. At higher concentration, the surface incorporation step is affected due to a higher dextrose concentration around the ice crystal surface which hinders attachment of water molecules to the crystalline structure. As cited by Halett (1964), very thin disks were obtained at bulk supercooling of 0.2 ˚C.

Halett (1964) showed that the extent of supercooling and mode of nucleation largely determine the morphology of ice crystals. According to Huige (1972), the morphology tends to disk shapes with increase in bulk supercooling. Michaels and co-workers (1966) obtained ice crystals from pure water in capillary tubes whose basal plane had a smooth interface at supercooling below 0.2 ˚C and at higher supercooling, the basal plane had a rough conical depression whose size increased with increasing supercooling. This substantiates the need to maintain constant, low supercooling, stirring rates and seeding protocol in this investigation on the effect of antiscalants on crystallization kinetics in EFC. Presence of ionic salts and poly acrylic acid did not change the morphology of ice, but some surfactants caused pitting of the basal plane surface. Omran and King (1974) observed a decrease in ice crystal size with increase in sugar concentration. The relative rates of nucleation and growth determine the crystal size, hence CSD, and ice crystals normally grow in flat disk shapes.

3.5 Determination of solubility and crystallization kinetics

Rodriguez-Pascual and co-workers (2009) determined the phase equilibria data for a $NaHCO_3$-Na_2CO_3-H_2O system. A tightly closed, fully insulated and well agitated crystallizer was used. Equilibration was allowed to occur over a period of 48 – 72 hours and the period was deemed enough for Ostwald ripening to occur. The solubility concentrations were obtained by titration to an accuracy within 1 %.

An MSMPR and a fluidized bed reactor can be used to predict the growth kinetics of crystals growing in suspension (Al-Jibbouri and Ulrich, 2001). Accurate prediction of crystal size distribution at a particular hydraulic residence time under steady state conditions is pertinent to determination of nucleation and growth rates simultaneously in an MSMPR. The CSD which depends on nucleation and growth kinetics as well as residence time distribution in the crystallizer can be determined using the population balance model (Randolph and Larson, 1971 as cited by Libin et al., 2009). However, Liu and co-workers (2004) comment that, use of an MSMPR crystallizer and the population balance equation is time consuming and the

process is difficult to control. Deviation from the McCabe ΔL law has been observed for small crystals in previous experimental work and this complicates estimation of the crystallization kinetics (Libin et al., 2009; Sha et al., 1996).

Libin and co-workers (2009) investigated the crystallization kinetics for $Na_2SO_4.10H_2O$ in an MSMPR crystallizer in which a period equivalent to eight residence times was allowed for attainment of steady state (Sha et al., 1996). It was observed that the growth of $Na_2SO_4.10H_2O$ crystals is size-dependent. Sha and co-workers (1996) also obtained a similar result for K_2SO_4. The nucleation rate was estimated for a nuclei size of 0.4 μm since it is difficult to estimate for a nuclei size of zero in a size dependent growth system. Sha and co-workers (1996) highlighted that the zero size nucleation rate does not effectively describe a system that shows strong size dependent growth; an arbitrary method which is generally acceptable is to use a one-size nucleation rate and assume that all crystals grow from this size.

Brecevic and Garside (1981) allowed at least ten residence times of 2.5 – 4.9 minutes to attain steady state conditions as determined by constant particle density. Chivavava and co-workers (2014) used eight residence times of 20 – 45 minutes. This implies that the number of residence times required to attain steady state conditions depends on the prevailing operating conditions such as temperature, solids density, degree of mixing and kinetic rates of nucleation and growth. According to Vavouraki and Koutsoukos (2012), the large metastable zone width of sodium sulphate allows accurate determination of the effect of impurities on crystallization kinetics in an MSMPR crystallizer. Moreover, measurement of particle size distribution in an MSMPR crystallizer is a common method for determining crystallization kinetics (Libin et al., 2009).

Chivavava and co-workers (2014) obtained crystal size distributions for determination of $Na_2SO_4.10H_2O$ crystallization kinetics using an in-situ digital imaging technique. A white light source was used to illuminate the crystallizer suspension whilst images were captured by a metal oxide semi-conductor camera which was connected to a computer. The image sequences were recorded by a digital motion analyser software, MotionBLITZ Director. The acquired images were digitally processed using custom-developed algorithms which allowed conversion from red-blue-green (RGB) format to grayscale, background subtraction, segmentation, thresholding and at times, edge detection. CSDs were then obtained from processed images and at least 1000 crystals were counted. However, crystal sizes lower than

30 μm could not be analysed due to poor magnification and it was deemed that this would not significantly affect the CSD, since mean sizes of CSDs obtained under an optical microscope were off by only about 2 – 10 μm. Michaels and co-workers (1966) measured ice growth rates using a microscope equipped with a micrometre eyepiece.

Huige (1972) measured nucleation rates of ice crystals in pure water by counting the number of crystals per unit suspension volume at steady state using direct visual observation for at least 10 samples per run. The population balance model was used for ice crystals grown from dextrose solutions since the crystals were too small for visual counting. The nucleation rate at steady state is the number of crystals per unit suspension volume divided by the mean residence time at steady state. Steady state was achieved after 3 residence times, as determined from constant crystal population density.

3.6 Research motivation

Previous research focused on batch experiments to determine the effect of additives on either salt or ice crystallization separately. Experiments for salt were carried out at ambient to high temperatures and there is little information in literature about the effect of additives on ice crystallization. The current research seeks to investigate the effect of antiscalants in simultaneous crystallization of ice and salt under eutectic conditions characterized by sub-zero temperatures in a continuous EFC process.

3.6.1 Aim and Hypotheses

The aim of the research is to investigate the effect of a phosphonate antiscalant on salt and ice crystallization in eutectic freeze crystallization. It is hypothesized that the nucleation and growth rates of both ice and salt crystals will decrease with increasing antiscalant concentration. This can be justified by the fact that antiscalants, particularly phosphonates, are well known for inhibiting crystallization and precipitation of sparingly soluble salts. However, the salt of interest in this investigation is $Na_2SO_4.10H_2O$ which has high solubility in water under ambient conditions. It is quite imperative to determine if the presence of antiscalant in brine streams has an effect on $Na_2SO_4.10H_2O$ crystallization kinetics. Since ice and salt crystallization rates are interdependent in EFC, it is expected that the effect of antiscalant on salt crystallization kinetics will be induced on ice crystallization kinetics. Several authors have reported a decrease in the nucleation and / or growth rates of salt

crystals with increasing additive concentration and it is anticipated that the sub-zero temperatures employed in EFC will not produce an opposite effect.

3.6.2 Key questions

The following research questions arise:

1. How is the phase equilibria of a binary Na_2SO_4 aqueous system affected by different antiscalant concentrations?
2. How are the nucleation and growth rates of ice and salt crystals altered by different antiscalant concentrations in EFC?
3. How are the morphology and size (hence crystal size distribution) of ice and salt crystals changed by different antiscalant concentrations in EFC?
4. How is the purity of both ice and salt affected by different antiscalant concentrations in EFC?
5. Is there a threshold antiscalant concentration beyond which the effect becomes pronounced or is reversed?

3.6.3 Objectives

The objectives of this research are to determine the effect of a phosphonate based antiscalant on:

1. The phase equilibria of a binary Na_2SO_4 aqueous system.
2. The crystallization kinetics (nucleation and growth rates) of both ice and salt crystals in a continuous EFC process.
3. The Crystal Size Distributions (CSDs) of both ice and salt crystals in EFC.
4. The morphology and purity of both ice and salt crystals.

3.6.4 Scope

Antiscalant concentrations normally encountered in industry will be used in this investigation. Information obtained on antiscalant data sheets reveals that normal dosages do not exceed 5 ppm at most. However, in the case of RO brine streams, this would have increased by a factor of 100, assuming a water recovery of 99 %. Determination of the nucleation and growth rates of crystals requires solubility data; hence the need to determine changes in solubility in the presence of different antiscalant concentrations. Nucleation and / or growth rates determine the final product quality (crystal size and morphology) and the research will also investigate the effect of antiscalant on these quality parameters.

4 Methodology

This section provides details of the antiscalant analyses conducted and description of the equipment and materials used in the experiments. The experimental procedure as well as the measurement techniques, sampling methods and data analyses techniques are clearly outlined.

4.1 Antiscalant analyses

The antiscalant was analysed in an attempt to determine its molecular composition and functional group(s). ICP-MS was used to analyse for specific ions and liquid state NMR was used in a bid to identify the actual phosphonate species in the antiscalant.

4.1.1 Dry mass

The dry mass of the antiscalant was determined by heating three samples of known initial weight at 40 °C until the final mass became constant. It was then calculated using equation 4-1.

$$X(\%) = \frac{100(m_f)}{m_i} \qquad 4\text{-}1$$

Where X (%) is the dry mass percentage, m_f and m_i are the final and initial masses of the samples respectively.

4.1.2 Chemical composition

ICP-MS was used to determine the concentrations of certain cationic and anionic species which include K^+, Na^+, P^{3-}, Cl^-, PO_4^{3-} and SO_4^{2-}. NMR spectroscopy of 13C isotope was conducted using the 300 MHz and 400 MHz NMR instruments with D_2O insert in the samples in order to identify the constituent phosphonic acid molecules.

4.2 Solubility experiments

Freezing point depression (FPD) calculations were conducted using Equation 2-9 prior to experimental validation. It was indeed necessary to validate the calculations empirically in order to maintain constant supersaturation (supercooling), measured from equilibrium solubility in the presence of impurities, in subsequent crystallization kinetics experiments. The solubility experiments were conducted in batch crystallizers to determine the effect of the phosphonate antiscalant on FPD of water in hypoeutectic solutions and Na_2SO_4 solubility in hypereutectic solutions.

4.2.1 Equipment and materials

In this study, a synthetic Na_2SO_4 aqueous solution was used to determine the effect of antiscalants on salt solubility. Solutions were prepared using 99 % analytical grade anhydrous Na_2SO_4 and deionised water of resistivity 6.2 mega Ohms centimetre (MΩcm). Three hypoeutectic solutions of concentrations 0.8, 1.8 and 2.8 % wt. Na_2SO_4 and three hypereutectic solutions of concentrations 4.5, 5.5 and 6.5 % wt. Na_2SO_4 were used to obtain the freezing and salt solubility lines of the phase equilibrium diagram in both pure solutions and in the presence of different antiscalant concentrations.

The commercial antiscalant used was a neutralized aqueous solution of phosphonate(s) with a pH of 10 ± 0.2. The actual composition of the antiscalant is proprietary. For each solution composition, the experiment was repeated with antiscalant dosages of 200 mg/L, 350 mg/L and 500 mg/L in order to observe the effect of various antiscalant concentrations on phase equilibria. These antiscalant concentrations were computed on the basis of an RO water recovery of 99 % and RO feed stream antiscalant dosages recommended by the Supplier of 2 – 5 mg/L. Ice seeds were prepared by freezing water droplets on a glass plate in a domestic freezer and 99 % analytical grade $Na_2SO_4.10H_2O$ was used as salt seeds.

A 2 L jacketed Pyrex® glass crystallizer was used in which the solution in the crystallizer was cooled indirectly using Kryo 40 coolant. The temperature of the coolant was maintained constant and circulated through the crystallizer jacket by a LAUDA PROLINE RP855 refrigerated bath chiller. The coolant tubes were insulated to minimize heat flux from the atmosphere. Two PT100 temperature sensors with an accuracy of ±0.01 ˚C were used to measure the top and bottom temperatures of the solution. Agitation was provided by a 4 blade pitched type impeller driven at 600 rpm by an electric motor equipped with manual speed control.

4.2.2 Experimental set up

Figure 4-1 shows the experimental set-up used for determining the effect of the antiscalant on phase equilibria of a binary Na_2SO_4 aqueous solution. It depicts the 2 L jacketed glass crystallizer in which the solution was agitated. The coolant flow circuit is also shown in which coolant maintained at a constant temperature flowed through the crystallizer jacket. The experiment was conducted in a temperature controlled lab in which the lab temperature was set to tally with the coolant temperature to minimize heat flux into the crystallizer. Under

these conditions, the solution temperature could be maintained constant for equilibration to occur.

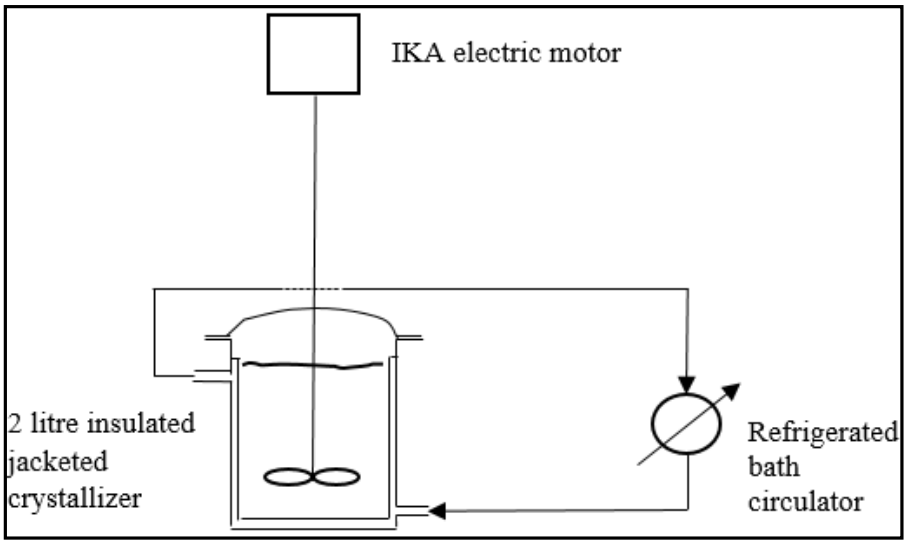

Figure 4-1. Experimental set-up for solubility experiments

4.2.3 Experimental Procedure

The saturation temperatures of the aqueous Na_2SO_4 solution compositions used were predicted using the Helgeson-Kirkham-Flowers (HKF) equation of state on OLI Stream Analyser 9.0 software and these are shown in Table 4-1 together with the operating temperatures.

Table 4-1. Aqueous Na_2SO_4 solution compositions used

Na_2SO_4 % wt.	Saturation temperature (˚C)	Seeding temperature (˚C)	Operating temperature (˚C)
0.8	-0.27	-0.29	-0.45
1.8	-0.57	-0.59	-0.67
2.8	-0.84	-0.86	-1.02
3.95	-1.14	-1.16	-1.20
4.25	-0.25	-0.27	-0.40
5.10	2.45	2.43	2.32
5.80	4.40	4.38	4.36

The solution was cooled at a rate of 1 ˚C / min to 0.02 ˚C below the saturation temperature and seeded with ca. 0.1 g of ice or salt crystals depending on solution concentration, to initiate secondary nucleation of the crystallizing species. After nucleation, the crystal suspension was subjected to a constant temperature below the saturation temperature of the initial solution concentration, for a pre-determined period of 72 hours to allow the solution to

equilibrate by Ostwald ripening. The equilibration period was determined initially by taking solution samples on a daily basis at 4 hour intervals. It was observed that the solution concentration changed during the first two days and remained fairly constant on the third day.

Three solution samples were taken from the agitated solution at the middle section of the crystallizer using a syringe fitted with a 0.2 μm cellulose acetate membrane filter and they were analysed for sodium concentration using Atomic Absorption Spectroscopy (AAS). This concentration was taken to be the equilibrium concentration at that temperature. Agitation was not stopped during sampling due to development of a concentration gradient as a result of product separation. Each experiment was done in triplicate to ascertain reproducibility.

4.3 Crystallization kinetics experiments

Continuous EFC experiments were conducted to determine the effect of the antiscalant on the nucleation and growth rates of both ice and sodium sulphate crystals under sub-eutectic conditions. Since these two fundamental rate processes determine the final product quality in terms of crystal size distribution and morphology, the effect of the antiscalant on these quality parameters was also investigated.

4.3.1 Equipment and materials

4.3.1.1 Chemicals

A synthetic aqueous Na_2SO_4 solution was used to determine the effect of the antiscalant on crystallization kinetics. Solutions were prepared using 99 % analytical grade anhydrous Na_2SO_4 and deionised water of resistivity 6.2 MΩcm. Experiments were conducted under sub-eutectic conditions using a 4.2 % wt. aqueous Na_2SO_4 solution. Details of antiscalant used and its concentrations are given in section 4.2.1.

4.3.1.2 Crystallizer and accessories

The experiments were conducted in a 2 L jacketed Duran® glass continuous crystallizer fitted with a concave bottom section in which heavy salt crystals settled. The concave shape facilitated pumping of the salt slurry out of the crystallizer using a Watson Marlow 520S peristaltic pump. The top section was fitted with an overflow pipe through which the ice slurry exited the crystallizer. The effective heat transfer surface area was that of the middle section which was jacketed and the effective volume was found to be 1.8 L. Figure 4-2 shows the crystallizer configuration.

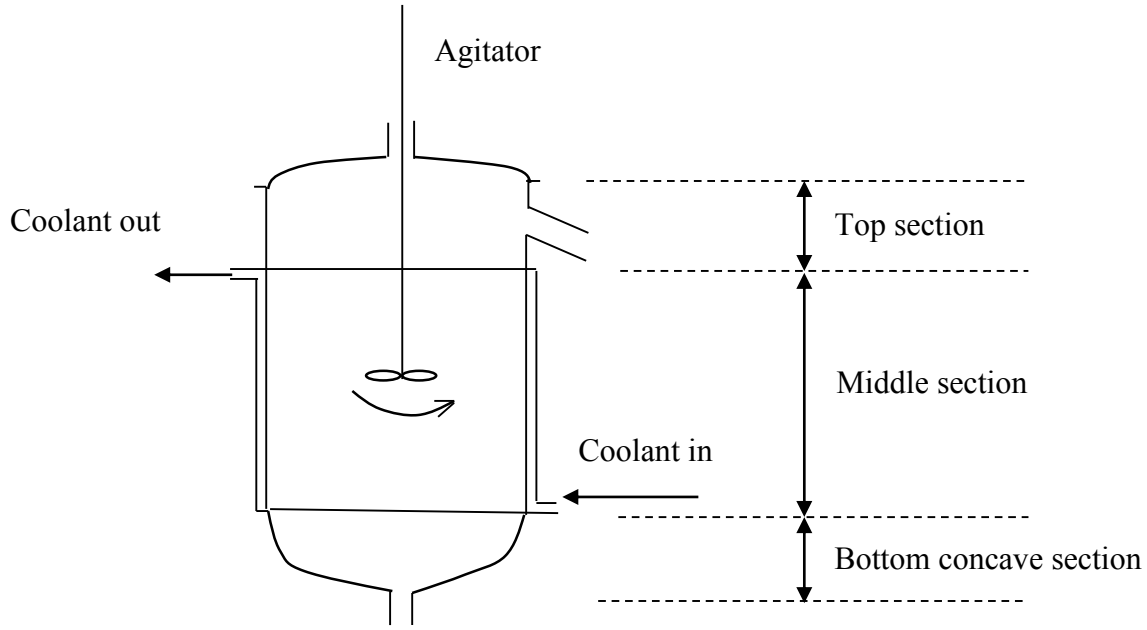

Figure 4-2. Crystallizer configuration

A custom developed algorithm was used to control the cooling rate as well as to maintain the crystallizer temperature constant, hence constant supercooling throughout all experiments. The solution was cooled indirectly by means of silicon oil coolant flowing through the crystallizer jacket. The crystallizer was a component of the Labmax unit which was designed to allow the coolant, Kryo40®, circulated by the Lauda Proline RP855 refrigerated bath cooler to exchange heat with silicon oil within the unit by means of a plate heat exchanger located inside the unit. The silicon oil then circulated through the jacket of the crystallizer and exchanged heat with the solution inside the crystallizer. A PT100 temperature sensor with an accuracy of ±0.01 ˚C was used to measure the middle section temperature of the solution. Agitation in the crystallizer was provided by a 2 blade impeller located in the middle section of the crystallizer. It was pre-determined that the 2 blade impeller provided better settling of salt crystals whilst maintaining adequate mixing. The feed solution was pre-cooled in two tubular, insulated glass heat exchangers connected in series. A counter-current cooling configuration was adopted in which Kryo40® coolant was pumped in reverse flow to the feed solution as shown in Figure 4-3.

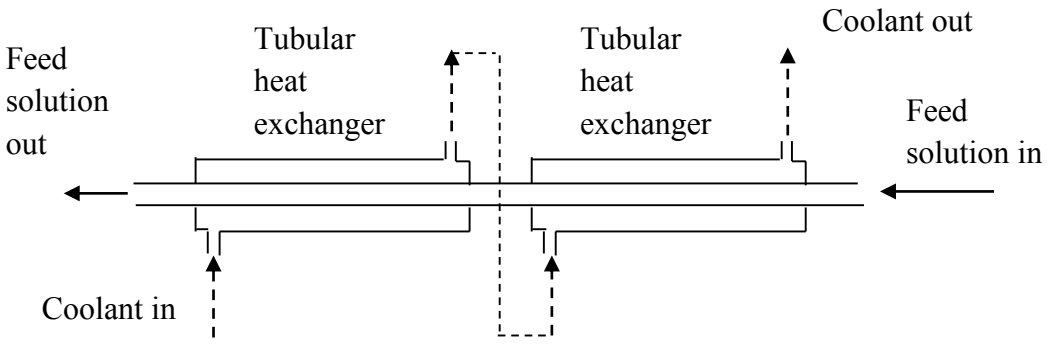

Figure 4-3. Counter-current flow cooling unit

The coolant temperature was maintained constant by means of a Lauda Proline RP845 refrigerated bath circulator. Pre-cooling ensured that the feed solution entered the crystallizer at a sufficiently low temperature to avoid huge temperature fluctuations in the crystallizer and to reduce the heat load of the crystallizer. The feed was introduced at the middle of the crystallizer by means of a Watson Marlow 505S peristaltic pump. The suction pipe of this pump was immersed in a feed storage container maintained at a constant level by means of a Watson Marlow 520S peristaltic pump, which continuously replenished the solution. This was done to ensure constant static head on the pump suction side since the flow rate delivered is dependent on the system head. All pumps were calibrated using a measuring cylinder and stop watch to determine the flow rate obtained over a range of pump speed. In order to maintain a constant hydraulic residence time of 30 minutes in the crystallizer in all experiments, it was determined that the required feed flow rate was 60 ml / min and this corresponded to 14 rpm pump speed according to the calibration. The pumps were maintained in their positions as experiments progressed to avoid altering the system head which would in turn affect the flow rate obtained, hence the residence time.

4.3.1.3 Image acquisition

In-situ image acquisition was applied in order to capture real-time images of the ice-salt crystal suspension in the crystallizer under sub-eutectic conditions. A Mikrotron EoSens MC1363 high speed camera was used for this purpose and it was fitted with a zooming lens to magnify crystals and observe morphology in-situ. A white light source was used to illuminate the contents of the crystallizer by means of an optical fibre. A frame rate of 506 frames per second and a shutter time of 30 μs were used. These settings were maintained constant throughout all experiments to establish the effect of different antiscalant concentrations on the crystallization kinetics of ice and $Na_2SO_4 \cdot 10H_2O$ crystals in EFC. The camera was connected to a computer via a one gigabyte frame grabber and

MotionBLITZDirector® 3.6.0.2 software was used for image acquisition. Prior to commencing each experiment, the camera was calibrated by capturing an image of a ruler placed inside the crystallizer in the plane of focus. This was done to determine the size of each pixel which was then used to calculate the crystal sizes during image processing. Owing to the large difference in size between ice particles and salt crystals, different zooming factors were used for the two crystal species. The zooming factors were such that the length of a pixel was determined to be equivalent to 16.13 μm and 3.66 μm for both ice and salt respectively.

4.3.2 Experimental set-up

Figure 4-4 shows the experimental set-up which consisted of the continuous glass crystallizer, a white light source which illuminated the crystal suspension in the crystallizer, a high speed camera used to capture the images of crystals in-situ and a data acquisition computer.

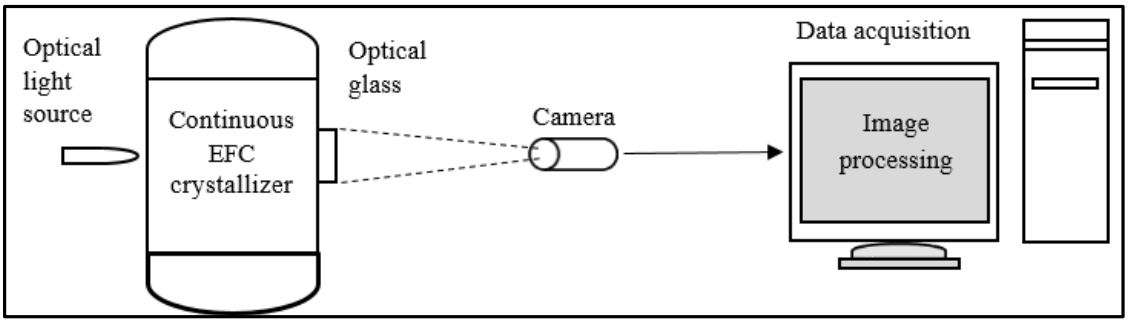

Figure 4-4. Experimental set-up for crystallization kinetics experiments

Figure 4-5 shows the labelled components of the Labmax Unit and other crystallizer accessories. The legend is provided in the caption.

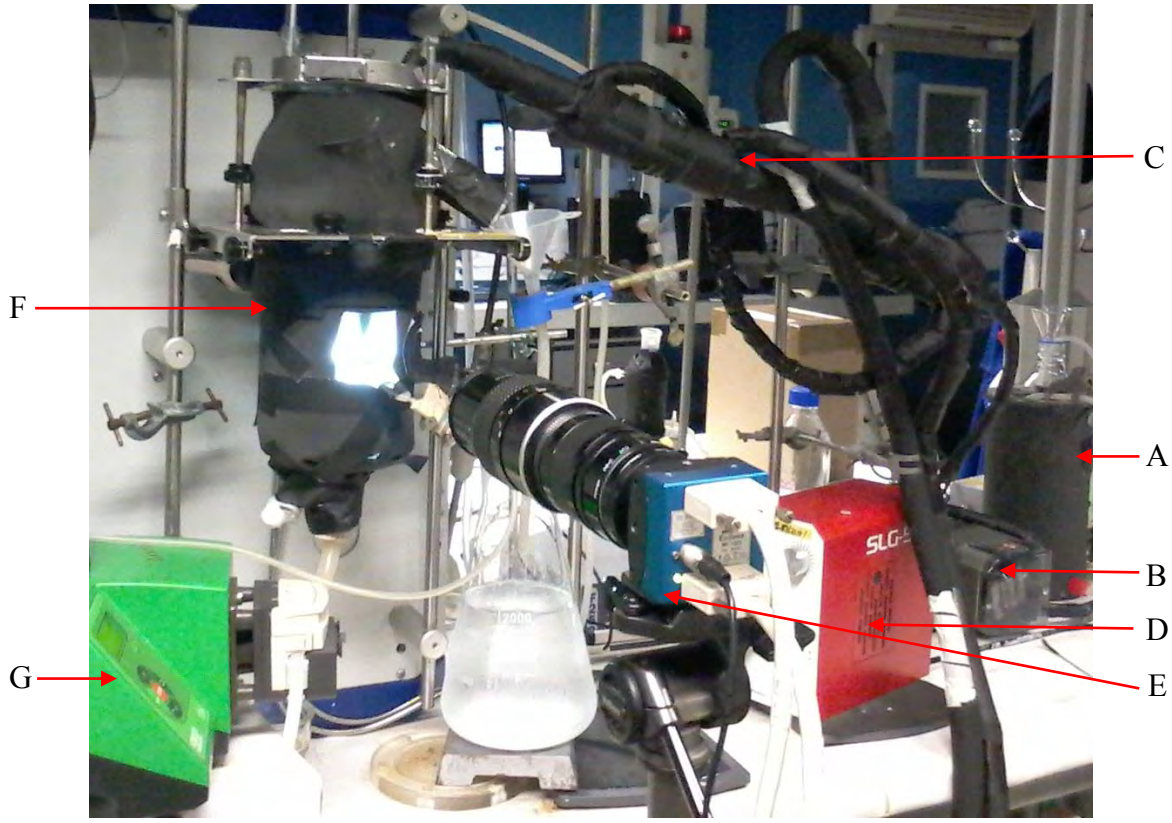

Figure 4-5. Crystallizer and its accessories. A – insulated and agitated feed container, B – feed pump, C – pre-cooler, D – white light source, E – High speed camera, F – 2L insulated jacketed glass crystallizer, G – Salt slurry pump.

4.3.3 Experimental procedure

The feed solution was pumped through the pre-cooler at 60 ml / min with the Kryo40® coolant temperature maintained at -2.7 ˚C, and it was noted that the solution temperature dropped from ca. 25 ˚C to ca. - 0.8 ˚C. Therefore, the pre-cooler duty was calculated to be 112 W. This implies that the sensible heat lost by the solution in the crystallizer corresponded to a temperature drop of about -0.35 ˚C and this was computed to be 1.5 W. Under these conditions, the crystallizer jacket temperature, was maintained at ca. -2.60 ˚C. This implies that the heat transfer temperature driving force for the crystallizer was ca. 1.5 ˚C. The eutectic temperature of a Na_2SO_4 aqueous solution was determined thermodynamically using the Helgeson-Kirkham-Flowers (HKF) equation of state on OLI Stream Analyser 9.0 software. This was found to be -1.14 ˚C. However, the most frequently experimentally observed eutectic temperature during the experiments was -1.12 ˚C which was then used as a basis for supercooling measurement. The crystallizer was operated at a temperature of -1.16 ˚C to maintain a supercooling of ca. 0.04 ˚C. The procedure consisted of start-up in batch mode and change to full operation in continuous mode .These are described separately below.

4.3.3.1 Start-up procedure

The start-up was done in batch mode by pumping the feed solution through the pre-cooler into the crystallizer until the effective volume was filled. At this point the feed pump was stopped to allow the temperature of the solution in the crystallizer to drop to its eutectic temperature. Once this temperature was achieved, the feed pump was started and its flow rate increased gradually to avoid a huge temperature offset in the crystallizer and to allow the system to re-stabilize in terms of heat transfer. This time, cooling was continued to the seeding temperature of ca. 0.06 ˚C below the eutectic temperature at which 0.1 g of $Na_2SO_4.10H_2O$ crystal seeds were introduced into the crystallizer to induce secondary nucleation of salt. 0.1 g of ice seeds were introduced 5 minutes after seeding with salt. This was done to give salt seeds time to grow so as to minimize their entrainment in ice. As soon as ice nucleated, the solution temperature would almost invariably jump to -1.12 ˚C which was taken to be the equilibrium eutectic temperature. The salt slurry pump was then started to allow settled salt to exit the crystallizer whilst floating ice would overflow through the top outlet.

4.3.3.2 Continuous operational mode

In this mode of operation, care was taken to avoid fluctuations in feed flow rate by ensuring the feed tank was maintained at constant level. This would ensure a constant hydraulic residence time (τ) of 30 minutes. Other parameters which were maintained constant throughout the experiments include the agitation rate of 180 rpm, supercooling of 0.04 ˚C and camera settings given in section 4.3.1.3. In preliminary experiments, images were captured and solution samples taken at 30 minute intervals for a minimum of 6τ to determine the number of residence times required to achieve steady state. This would be the time at which the crystal size distributions for ice and salt as well as solution concentration would become reasonably constant and it was found to be 3τ. In subsequent experiments, images and solution samples would only be taken thereafter, that is, at 4τ, 5τ and 6τ. At the end of the experiment, both ice and salt slurries were collected and filtered separately. Ice and salt samples of about 5 g were taken to determine the purity of the products, with particular emphasis on phosphorus content. The remaining ice and salt were washed with 100 g and 50 g of de-ionised water and saturated Na_2SO_4 solution respectively and samples taken for purity analyses. Inductively Coupled Plasma Optical Emission Spectroscopy (ICP-OES) was used to determine the phosphorus content in ppb and Atomic Absorption Spectroscopy

(AAS) was used to determine the sodium content in ppm. The experiments in the absence and the presence of antiscalant were done in triplicate to ascertain reproducibility.

4.3.4 Data analyses

4.3.4.1 Image processing

Images obtained were processed manually using Image J 1.48V software. This was done by determining the surface area in square pixels of user-defined selections of individual crystals. The surface area was converted from square pixels to μm^2 as shown in Equation 4-2 using the calibration data obtained as described in section 4.3.1.3.

$$S_A = S_a \times p_l^2 \quad 4\text{-}2$$

Where S_A is the surface area in μm^2, S_a is the surface area in square pixels and p_l is the pixel length in μm.

The equivalent spherical diameter (d_e) of the crystals was then calculated using Equation 4-3.

$$d_e = \sqrt{\left(\frac{4S_A}{\pi}\right)} \quad 4\text{-}3$$

Particles were counted from a fixed number of frames and it was observed that the number of particles obtained were fairly constant in the absence and presence of different antiscalant concentrations. On average, about 300 and 700 particles were counted for salt and ice respectively in all experiments.

4.3.4.2 CSD analysis

The crystal population per unit volume (N) was computed by dividing the particle diameters (d_e) obtained by the product of the area of focus (A_f) and the depth of field (d_f) as shown in Equation 4-3.

$$N = \frac{d_e}{A_f \times d_f} \quad 4\text{-}4$$

The crystal population per unit volume per unit size, termed the crystal population density, was then calculated by dividing N by the crystal size interval (ΔL_b) as shown in Equation 4-5.

$$n = \frac{N}{\Delta L_b} \quad 4\text{-}5$$

The CSDs presented were plots of n against crystal size, L.

4.3.4.3 Determination of crystallization kinetics

The population balance model was employed to obtain kinetic data from CSDs as explained in section 2.4. The nucleation and growth rates were evaluated from the intercept and gradient of the semi-logarithmic plot of particle population density (n) versus crystal size (L) respectively. These were then compared for different antiscalant concentrations to establish the effect of antiscalant concentration on crystallization kinetics. The effect of the antiscalant on the CSD was also determined by superimposing the CSDs obtained for the control experiment and in the presence of 200, 350 and 500 mg/L antiscalant. Morphology was observed visually on original images and any changes in the presence of antiscalant were noted.

The purity of both ice and Na_2SO_4 crystals was determined to establish the effect of antiscalant on this property with respect to phosphorus content. Ice was also analysed for sodium using AAS.

5 Results and Discussion

This section presents the results of the antiscalant analyses and the experimental work conducted to determine the effect of a phosphonate antiscalant on the thermodynamics of a binary Na_2SO_4 aqueous solution and on the crystallization kinetics as well as product quality parameters of both ice and $Na_2SO_4.10H_2O$ in EFC.

5.1 Antiscalant analyses

Thermal drying experiments were conducted to determine the dry mass of the antiscalant. ICP-MS was employed to determine the concentration of specific cations and anions. Liquid-state NMR analyses was conducted to determine the actual molecular constituents of the antiscalant.

5.1.1 Dry mass %

The dry mass calculated from 3 samples was found to be 35.86 ± 0.33 wt. %. Since the antiscalant is described as an aqueous mixture of phosphonates, it can be deduced that this is the weight composition of the phosphonates and the rest is water.

5.1.2 ICP-MS analyses

ICP-MS results for elemental analyses are shown in Table 5-1.

Table 5-1. Elemental concentration results obtained using ICP-MS

Sample	Concentration (mg/L)			Ratio $\frac{[P]}{[Na]}$
	K	Na	P	
1	97.60	145700.00	94350.00	0.65
2	95.96	163100.00	107900.00	0.66
Mean	96.78	154400.00	101125.00	0.65
Sd	0.82	8700.00	6775.00	0.01

Two samples were analysed and although there is a considerable difference between their results, the ratio of the concentrations of P and Na are similar with a mean of 0.65 ± 0.01. Of particular interest is that, this ratio is almost equivalent to the ratio of the molar mass of P to twice the molar mass of Na, that is, 0.67.

This suggests a Na phosphonate in which two Na atoms have substituted the H atoms on the two hydroxyl functional groups of the phosphonic acid as shown in Figure 5-1. Therefore, the molecules have a non-polar alkyl chain and a polar $–O^-Na^+$ bond.

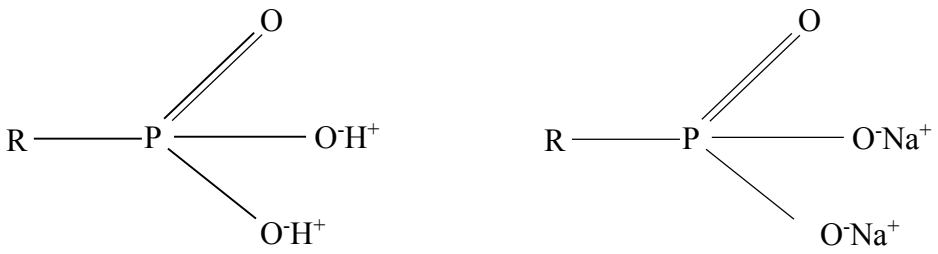

Figure 5-1. Phosphonic acid and Na phosphonate functional groups

Anions which include Cl^-, PO_4^{3-} and SO_4^{2-} were present in concentrations below 1.8 wt. % and these would be very minute considering the antiscalant concentrations of 200, 350 and 500 mg/L (0.02 – 0.05 wt. %). There was no meaningful information that could be deduced from anionic analyses.

5.1.3 NMR analyses

The antiscalant was also analysed for 13C isotope using NMR. Figure 5-2 shows the spectra obtained.

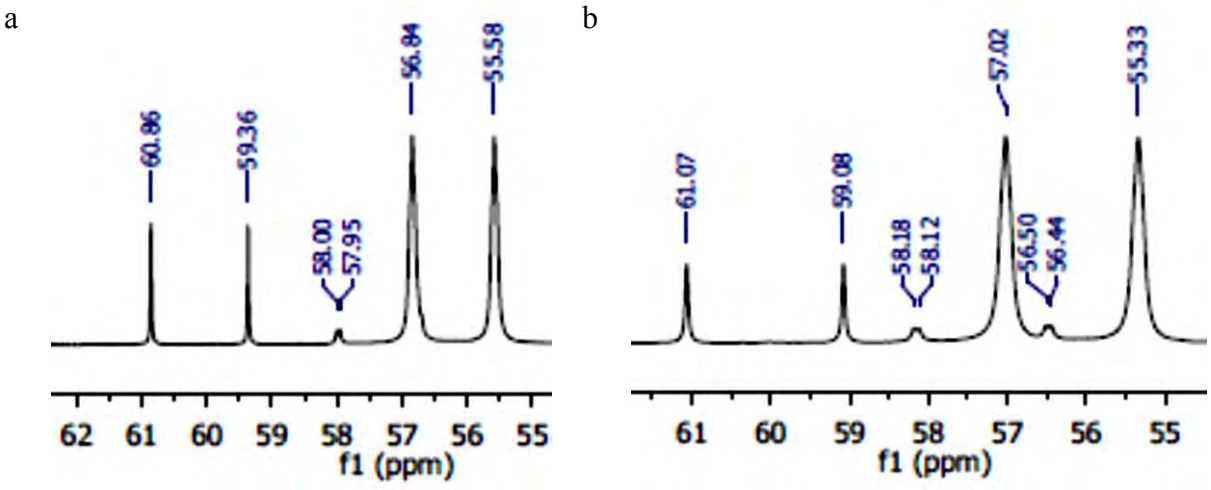

Figure 5-2. 13C isotope spectra of two antiscalant samples obtained using (a) 400 MHz NMR and (b) 300 MHz NMR instruments

Several carbon signals are visible in each spectrum implying the presence of a mixture of phosphonates or one chained alkyl phosphonate. Methylene phosphonate would result in only one carbon peak. This information together with the ICP-MS results confirm the presence of phosphonate(s) in the antiscalant although the actual molecular composition could not be

obtained. It is interesting to note that the spectrum was reproducible to a greater extent using NMR instruments of different frequencies. The chemical shifts of the tallest peaks were 56.94 ± 0.09 and 55.47 ± 0.08 on average.

5.2 Effect of antiscalant on Na_2SO_4-H_2O phase equilibria

The effect of different antiscalant concentrations on Na_2SO_4-H_2O phase equilibria was investigated in batch solubility experiments in which the crystal suspension was left to equilibrate over a pre-determined period of 72 hours. Supernatant samples were then obtained and analysed for Na concentration using AAS. These experiments were conducted to ensure constant supercooling in subsequent crystallization kinetics experiments, as measured from the respective empirically determined eutectic temperature, in the absence and in the presence of 200, 350 and 500 mg/L antiscalant.

5.2.1 Freezing Point Depression (FPD) calculations

Calculations were conducted, using Equation 2-22, prior to experimental investigations to assess the magnitude of the effect of the antiscalant on FPD. Equation 2-22 requires parameters such as the ionization factor, the cryoscopic constant of the solvent as well as the molality of the antiscalant, calculated in Section 5.2.1.1. As an assumption, Na_2SO_4 concentrations of up to 4.2 wt. % have been assumed to be dilute such that only pure water has been considered.

5.2.1.1 Molality of phosphonic acids

Table 5-2 lists typical phosphonic acids and their molecular weights.

Table 5-2. Molecular weights of typical phosphonic acids

Phosphonic acid	**M_r (g / mol)**
MP	96
ATMP	299
HEDP	206
DTPMP	573
DHTPMP	685
HDTMP	492

MP has the lowest M_r of 96 g / mol and DHTPMP has the highest M_r of 685 g / mol.

The molality of the phosphonic acids were calculated using equation 5-1.

$$m_2 = \frac{XC_a}{1000M_r} \quad \text{5-1}$$

where, X is the dry weight % of the antiscalant, C_a is the antiscalant dosage in ppm and 1000 is a factor to convert weight units to kg. The maximum dosage used was 500 mg/L which was taken as 500 ppm in this calculation. The dry mass of the antiscalant was found to be 36 wt. %. From Equation 5-1, it follows that the lowest molecular weight acid will have the highest molality, which in turn has a greater effect on FPD, therefore, 96 g / mol was used in this case as shown below:

$$m_2 = \frac{0.36\times500}{1000\times96} = 0.001875 \text{ Mol / kg solvent}$$

5.2.1.2 Freezing Point Depression (FPD)

The FPD was calculated using equation 2-22 where the value of E_f is taken to be 1.86 for water (Lide, 2005). The ionization factor of 3 assumes that the antiscalant dissociates in solution into PO_3^{2-} and two Na^+ ions.

$$FPD = 3 \times 1.86 \times 0.001875 = 0.01 \text{ K}$$

Although, the FPD appears to be negligible, a change in supercooling of 0.01 K can result in notable changes in the crystallization kinetics of ice. This can be seen in appendix 6 on a plot of ice growth velocity against supercooling adopted from Halett (1964).

5.2.2 Effect of the antiscalant on the eutectic point of a Na_2SO_4 aqueous system

Figure 5-3 is an experimentally determined phase equilibrium diagram for a Na_2SO_4 aqueous solution in the absence and in the presence of 200, 350 and 500 mg/L phosphonate antiscalant.

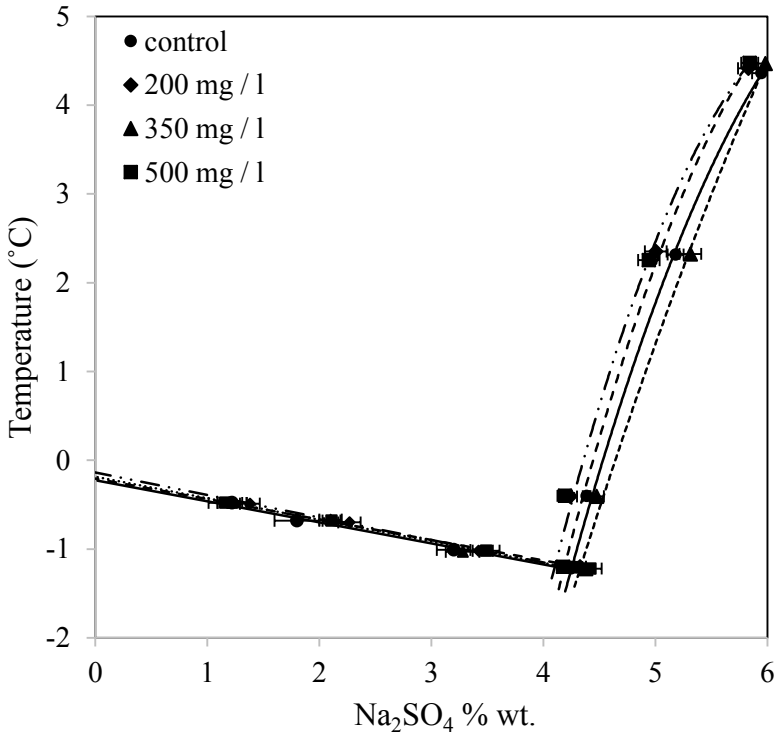

Figure 5-3. Effect of a phosphonate based antiscalant on the phase equilibria of a Na_2SO_4-H_2O system

Figure 5-3 shows that there was no effect on the FPD of water in hypoeutectic solutions, as predicted by the FPD calculations in Section 5.2.1, and the effect on salt solubility in hypereutectic solutions was negligible. The freeze lines are superimposed on each other and there was no clear trend observed on the salt solubility line with increase in antiscalant concentration. The presence of 200 and 500 mg/L antiscalant reduced salt solubility whereas the presence of 350 mg/L antiscalant increased salt solubility. This manifests as an upward and downward shift of the solubility line respectively. Since some of the error bars overlap, it was concluded that the effect on salt solubility was not significant. The freeze lines shown are linear lines of best fit with R^2 values above 0.98 showing perfect fits. The salt solubility lines are second order polynomials with R^2 values greater than 0.99. The freezing temperatures for pure water obtained by extrapolation are about -0.20 ˚C even in the absence of the antiscalant.

The most probable reason for the negligible effect on FPD was that the antiscalant concentration was very small to cause any significant effect on FPD as shown in section 5.2.1. This coupled with possible reversible adsorption of phosphonate molecules on ice crystal surfaces could have resulted in the negligible effect on FPD. This implies that the antiscalant molecules could have desorbed thereby allowing incorporation of water molecules

into the ice lattice. Fischer (1993) found that phosphonate adsorption is partially reversible. In addition, ice crystallization is known to reject impurities (Omran and King, 1974). Since FPD is a colligative property (Atkins and Paula, 2014), it was expected that the presence of the antiscalant would depress the freezing point of water in hypoeutectic Na_2SO_4 aqueous solutions in proportion to the impurity concentration.

The insignificant effect on salt solubility is most likely due to very small antiscalant concentrations investigated as well as reversible adsorption of antiscalant molecules on salt crystal surfaces. Since the crystallization process was allowed to proceed to equilibrium at constant temperature as confirmed by a fairly constant concentration on the third day, the antiscalant molecules could have desorbed over time owing to the propensity of the crystal lattices to attain a state of lowest Gibb's free energy. The equilibration process could have allowed partial dissolution and recrystallization causing lattice rearrangement of Na_2SO_4 molecules within the crystals with possibility of displacement of phosphonate molecules by free Na_2SO_4 molecules. This would result is restoration of the phase equilibria of a pure binary Na_2SO_4 aqueous system. The period of 72 hours could have allowed Ostwald ripening to occur.

The eutectic temperature obtained is about -1.2 ˚C and the eutectic concentration was found to be about 4.2 wt. %. These values are in good agreement with values reported in literature although the eutectic concentration reported in literature ranges from 3.8 – 4.2 wt. % (Brand et al., 2008; Reddy et al., 2010). From these observations, it can be deduced that the phosphonate based antiscalant in the concentration range of 200 – 500 mg/L did not have an effect on FPD of water in hypoeutectic Na_2SO_4 solutions, and it had a negligible effect on Na_2SO_4 solubility as highlighted by Selwitz and Doehne (2002).

5.3 Effect of the antiscalant on ice crystallization

Continuous EFC experiments were conducted to determine the effect of the antiscalant on the particle size distribution (PSD), crystallization kinetics, morphology and purity of ice particles. The term 'particle' was adopted for ice owing to the large number of ice agglomerates observed. It was difficult to identify individual crystals in the agglomerates. The results obtained are presented in this section.

5.3.1 Effect of the antiscalant on the PSD and crystallization kinetics of ice

PSDs were obtained manually using Image J for the control experiment and in the presence of 200, 350 and 500 mg/L antiscalant. The nucleation and growth rates were then evaluated from the intercept and gradient of the semi-logarithmic plot, respectively, of the crystal population density against size as shown in appendix 2.

5.3.1.1 Particle size distribution (PSD)

Figure 5-4 shows the effect of the antiscalant on ice PSD.

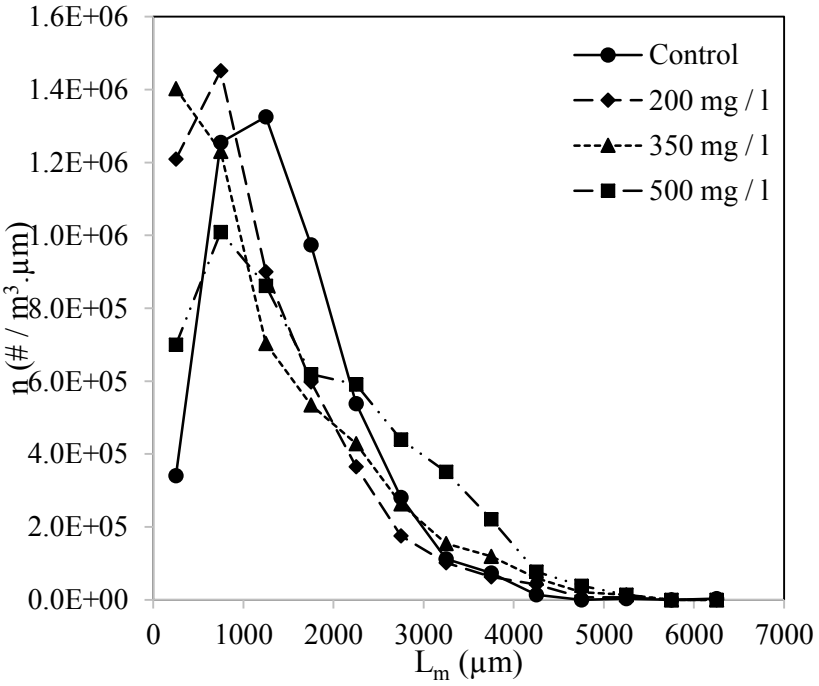

Figure 5-4. Variation of ice PSD in the absence and presence of 200, 350 and 500 mg/L antiscalant

Figure 5-4 shows that the presence of the antiscalant caused a general skewness of the PSD to the left. The effect increased with increase in antiscalant concentration up to 350 mg/L antiscalant, after which the effect diminished. The PSD in the presence of 500 mg/L shifted to the right of the PSD obtained in the presence of 350 mg/L. This implies a decrease in modal particle sizes up to an antiscalant concentration of 350 mg/L and a reduction in the effect of the impurity at an antiscalant concentration of 500 mg/L as shown in Figure 5-5. This suggests a turning point on the effect of the antiscalant on ice crystallization between antiscalant concentrations of 350 and 500 mg/L. A similar turning point was observed on the effect of the antiscalant on $Na_2SO_4.10H_2O$ crystallization as explained in section 5.4.

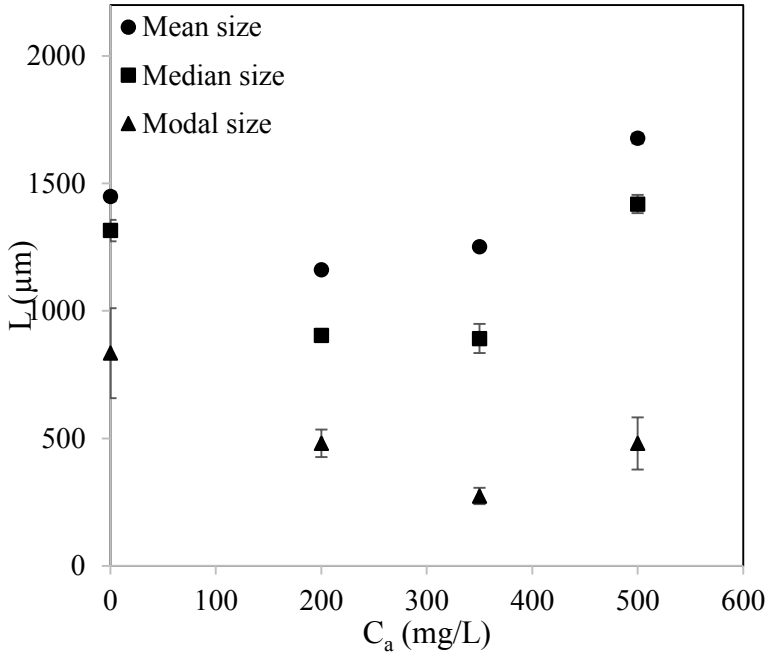

Figure 5-5. Variation of mean, median and modal particle sizes for ice in the absence and presence of 200, 350 and 500 mg/L antiscalant

Figure 5-5 shows that the mean ice particle size declined from 1,448.83 ± 18.25 to 1,160.93 ± 8.52 µm in the absence and presence of 200 mg/L antiscalant respectively. This is followed by a slight increase to 1,251.76 ± 1.09 and a drastic increase to 1,676.85 ± 19.46 µm in the presence of 350 and 500 mg/L antiscalant respectively. An almost similar trend is observed for the median particle size except that there is no change between 200 and 350 mg/L antiscalant. The modal particle sizes obtained in the control experiment and in the presence of 200, 350 and 500 mg/L antiscalant are 834.58 ± 176.52, 480.65 ± 53.84, 274.19 ± 31.61 and 480.51 ± 102.48 µm. A turning point is observed on the effect of the antiscalant between 350 and 500 mg/L. The mean, median and modal particle sizes are tabulated in appendix 3.

The general decline in the mean, median and modal particle sizes up to an antiscalant concentration of 350 mg/L is attributed to adsorption of antiscalant molecules on ice particle surfaces. This most likely results in reduction of available kink sites for incorporation of water molecules into the ice crystal lattice. In addition, adsorption of impurity molecules on ice particle surfaces results in modification of the surface properties such as adsorption energy and lattice incorporation energy. The decline in the mean, median and modal particle sizes could have resulted from an increase of either the adsorption energy required for water

molecules to adhere to the ice surface, or an increase in surface incorporation energy for incorporation of water molecules into the ice crystalline structure.

In the presence of 350 mg/L antiscalant, an anomaly is observed. The mean particle size increased marginally and the modal size decreased significantly. Whilst there is a significant reduction in modal particle size, an increase in the particle population density for particles greater than 2,000 μm is observed upon increasing the antiscalant concentration from 200 to 350 mg/L. The same phenomenon is observed for particles greater than 3,000 μm in comparison to the control experiment. The increase in the population density of bigger particles could explain the marginal increase in the mean particle size.

The increase in mean, median and modal sizes of ice particles in the presence of 500 mg/L antiscalant corresponds to a decrease in these parameters for salt as presented in Figure 5-14. This suggests that the antiscalant had a greater effect on salt crystallization than on ice crystallization at an antiscalant concentration of 500 mg/L. It should be noted that in a system where simultaneous crystallization of two different solid species occurs, adsorption of impurity molecules on the particle surfaces is governed by the adsorption equilibrium with respect to each solid species. It is most likely that, adsorption equilibria exist between antiscalant molecules in the solution and antiscalant molecules that have adsorbed on either solid surface. It is possible that at a higher antiscalant concentration of 500 mg/L, the antiscalant had a greater adsorption affinity for salt, thereby reducing its effect on ice crystallization. This implies that in the presence of 500 mg/L antiscalant, the surface adsorption and incorporation energies for water molecules dwindled, thereby favouring ice growth.

In EFC, where simultaneous crystallization of ice and salt occurs, there is likely to be preferential adsorption of the antiscalant on either ice or salt. Consequently, determination of the effect of additives on both ice and salt in EFC becomes complex since it requires measurement of surface adsorption energies of both crystal species, in the absence and presence of different additive concentrations to be able to determine the adsorptive affinity of the additive molecules towards each crystal species.

The ice PSDs shown in Figure 5-4 were characterized by the co-efficient of variation (CV) as shown in Figure 5-6. The CV obtained in the control experiment was 53.89 ± 5.99 % which is in agreement with the CV expected for a product from an MSMPR crystallizer (Mullin, 2001). However, this increased to 74.18 ± 3.73, 79.71 ± 3.16 and 65.35 ± 2.43 % in the

presence of 200, 350 and 500 mg/L antiscalant respectively. This implies a general increase in the spread of the PSDs in the presence of the antiscalant. It can be seen that 200 and 350 mg/L antiscalant resulted in higher CV values and 500 mg/L antiscalant led to a lower CV, confirming the turning point observed between 350 and 500 mg/L antiscalant. The general increase in CV with increasing antiscalant concentration suggests an increase in the particle population density of larger particles. It can be seen in Figure 5-4 that whilst the PSDs have been slightly skewed to the left, there is a general slight increase in the particle population density for particles of sizes greater than 3,500 μm in the presence of antiscalant.

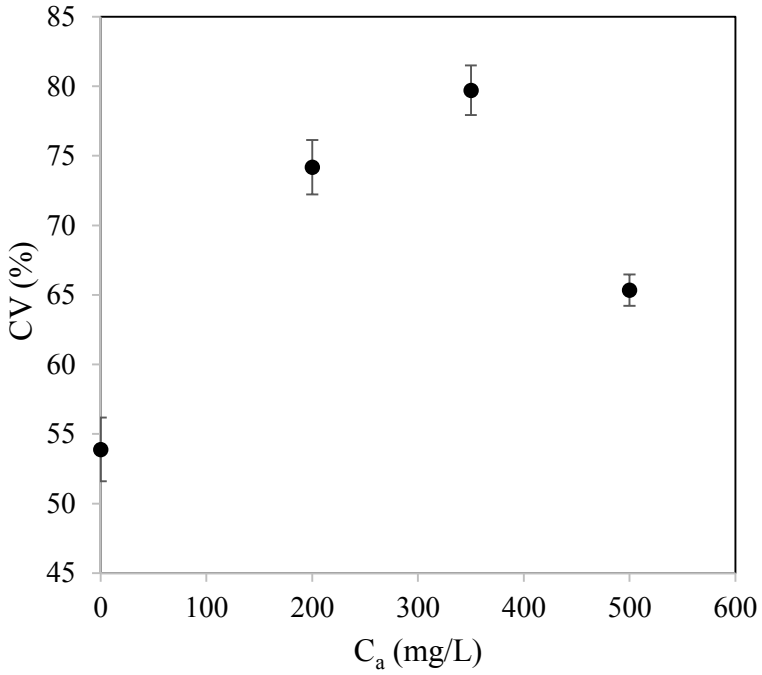

Figure 5-6. CV% for ice PSDs obtained in the absence and presence of 200, 350 and 500 mg/L antiscalant

5.3.1.2 Nucleation rate

Figure 5-7 shows the variation in ice nucleation rate in the absence and presence of 200, 350 and 500 mg/L antiscalant.

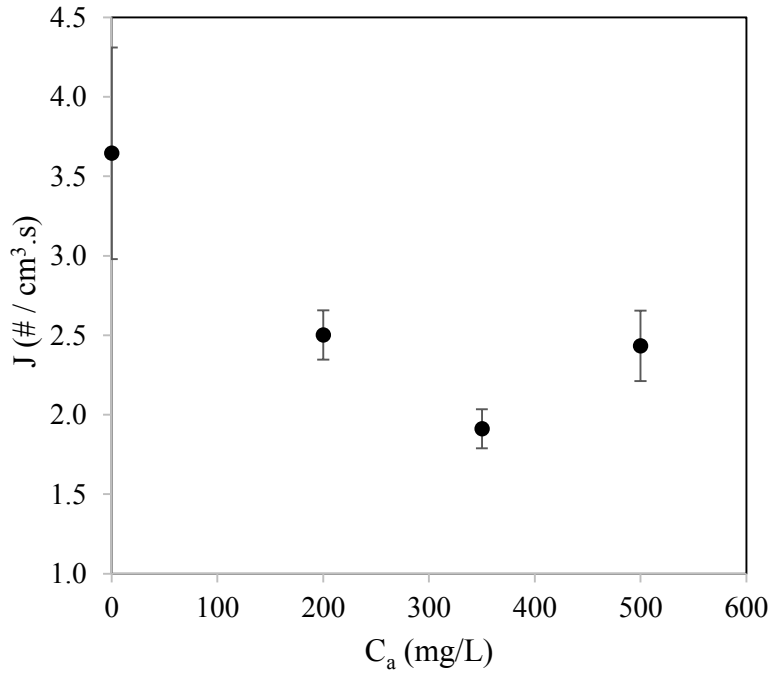

Figure 5-7. Variation of ice nucleation rate in the absence and presence of 200, 350 and 500 mg/L antiscalant

Figure 5-7 shows that there is a decrease in ice nucleation rate up to an antiscalant concentration of 350 mg/L followed by an increase in nucleation rate in the presence of 500 mg/L antiscalant. The nucleation rates obtained in the absence and presence of 200, 350 and 500 mg/L antiscalant are 3.64 ± 0.67, 2.50 ± 0.16, 1.91 ± 0.12 and 2.43 ± 0.22 measured in # / (cm^3.s) respectively. These values are tabulated in appendix 4.

It has been deduced in section 5.3.1.1 that the antiscalant had a greater inhibition effect on ice nucleation than on salt nucleation at antiscalant concentrations below 350 mg/L. The decrease in ice nucleation rate in this region could have occurred by adsorption of antiscalant molecules on ice nuclei. This would prevent growth of these nuclei to attain critical sizes. The effect increased with increase in antiscalant concentration as expected. In the presence of 500 mg/L antiscalant, the inhibition effect on ice nucleation lessened. This confirms a turning point on the effect of the antiscalant between concentrations of 350 and 500 mg/L.

Interestingly, this change corresponds to a decline in the growth rate of salt in the presence of 500 mg/L. This could imply interdependence between the ice kinetics and salt kinetics. It could be possible that the antiscalant had a profound effect on one of the solid species and this effect was induced on the other solid species as explained in section 5.3.1.3.

5.3.1.3 Growth rate

Figure 5-8 shows the effect of the antiscalant on growth rate of ice particles. It should be noted that the fractal dimension was used in the analysis of images due to the tendency of ice crystals to agglomerate. Agglomerates such as the ones shown in Figure 5-9 were observed in all experiments and it was difficult to identify individual crystals in the particles. The average R^2 value for the linear trend lines obtained in the semi-logarithmic plot of particle population density (n) against particle size (L) was 93.33 ± 3.64 %. An example of this plot is shown in appendix 2.

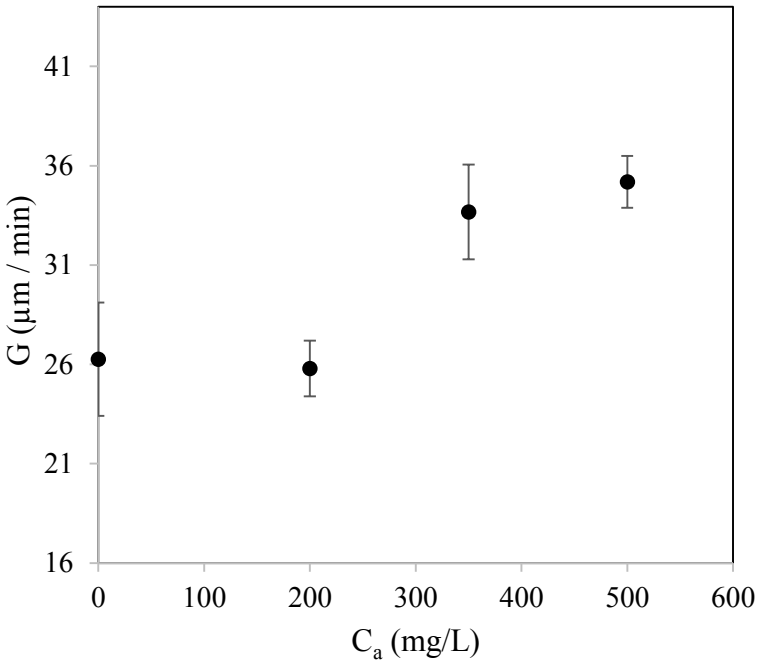

Figure 5-8. Variation of ice growth rate in the absence and presence of 200, 350 and 500 mg/L antiscalant

Figure 5-8 shows a negligible change in ice growth rate in the presence of 200 mg/L antiscalant and an increase in growth rate in the presence of 350 and 500 mg/L antiscalant. The growth rate values obtained in the absence and presence of 200, 350 and 500 mg/L antiscalant are 26.26 ± 2.86, 25.79 ± 1.40, 33.67 ± 2.38 and 35.19 ± 1.31 µm / min. Growth rate values are shown in appendix 4.

The observed trend for ice growth rate in the presence of 200 mg/L antiscalant is inconsistent with the decrease in mean, median and modal particle sizes. However, if the overlapping error bars are disregarded, a marginal decrease in ice growth rate is observed. The increase in ice growth rate in the presence of 350 and 500 mg/L antiscalant explains the general increase

in the mean particle size as shown in Figure 5-5. As discussed, the marginal decrease in ice growth rate in the presence of 200 mg/L antiscalant could be due to adsorption of the antiscalant molecules on ice particle surfaces resulting in one or a combination of the following: increase in adsorption energy required for water molecules to adhere to the ice surface, hindrance to surface diffusion of water molecules, reduction of available kink sites for growth and increase in lattice incorporation energy on kink sites. Figure 5-4 shows that the modal particle size decreased in the presence of 200 mg/L antiscalant. This implies a decrease in the ice growth rate.

Since constant supercooling and agitation rate were employed, it is highly likely that the hydrodynamics in the crystallizer remained invariably constant throughout all experiments. Consequently, it is expected that the extent of ice agglomeration also remained invariably constant and changes observed in the ice growth rate were entirely due to the effect of antiscalant.

The increase in the ice growth rate in the presence of 350 and 500 mg/L antiscalant was attributed to an indirect reduction in either surface adsorption energy or lattice incorporation energy of the ice particles. As discussed in section 5.3.1.1, the antiscalant could have adsorbed on salt crystals to a greater extent, thereby reducing its effect on ice crystallization. This would result in lower surface adsorption and incorporation energies. However, this phenomenon requires further investigations.

5.3.2 Effect of the antiscalant on morphology of ice

Figure 5-9 shows the morphology of ice particles obtained in the absence and presence of 200, 350 and 500 mg/L antiscalant.

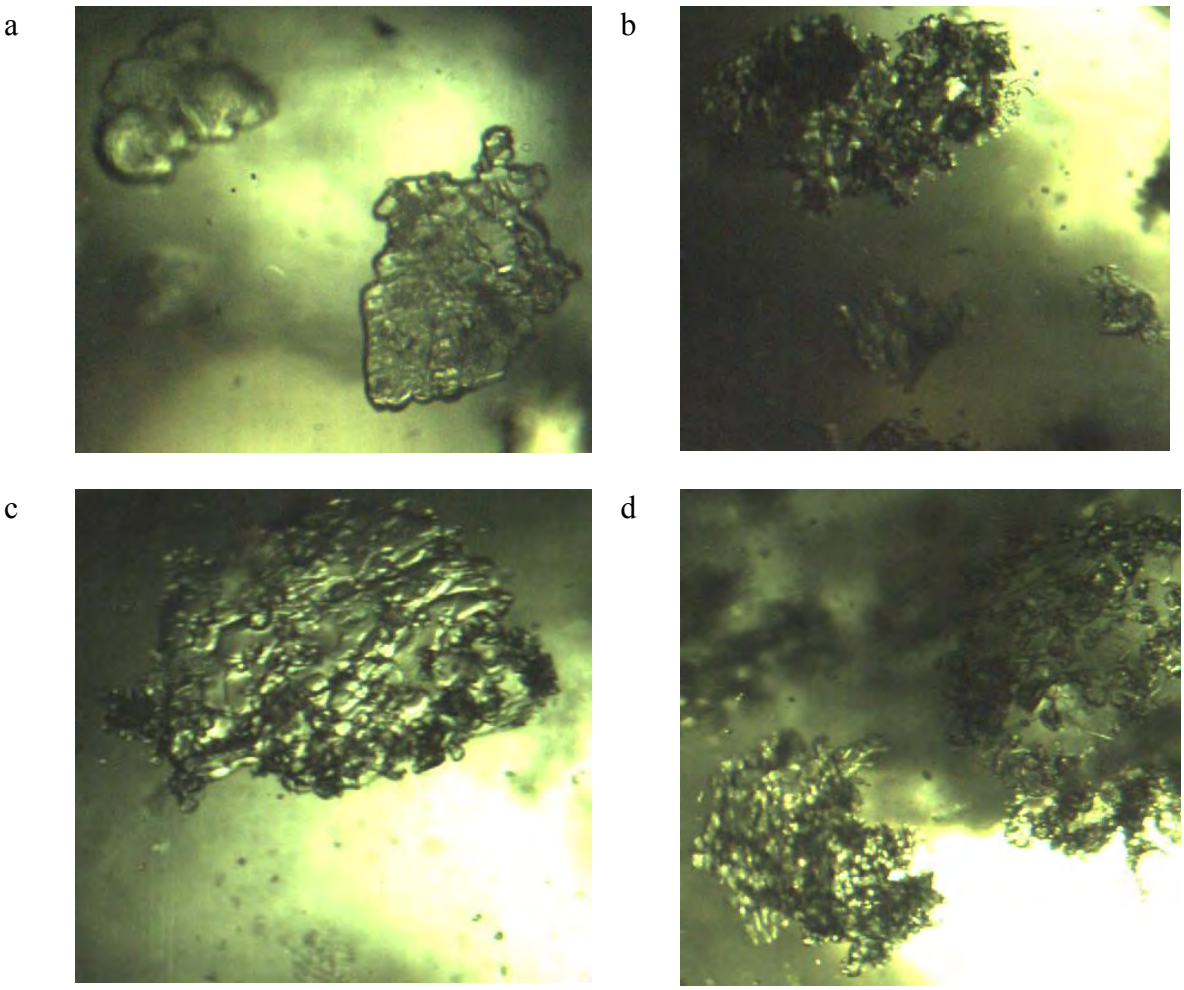

Figure 5-9. Morphology of ice in the absence and presence of 200, 350 and 500 mg/L antiscalant

Changes in morphology could not be determined from these images due to the high tendency of ice crystals to agglomerate. In Figure 5-9, the ice particle surfaces appear to be rougher in the presence of the antiscalant. The surface roughness is attributed possibly to a change in the growth mechanism of ice particles as a result of adsorption of antiscalant molecules on the ice surfaces. This is further aggravated by salt entrainment which was severe in the presence of the antiscalant. It is postulated that the antiscalant molecules formed bridges between the ice particles and salt crystals resulting in salt entrainment. This is likely to occur if the antiscalant molecules contain at least two highly electronegative atoms bonded to a hydrogen atom, thereby increasing the number of hydrogen bonds formed by a single molecule. This could not be ascertained from the antiscalant analyses described in section 5.1. It could be possible that the antiscalant molecules adhered to ice surfaces through hydrogen bonding and attracted surface cations of salt crystals electrostatically.

5.3.3 Impurity concentration in ice samples

Figure 5-10 shows the concentration of Na_2SO_4 in ice before and after washing in the absence and presence of 200, 350 and 500 mg/L antiscalant.

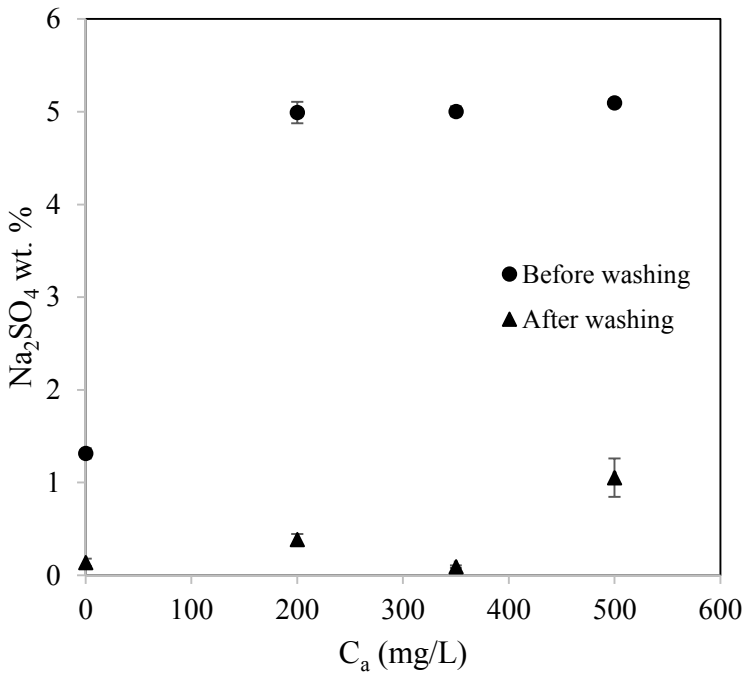

Figure 5-10. Variation of Na_2SO_4 concentration with antiscalant concentration

Figure 5-10 shows a significant reduction in Na_2SO_4 concentration before and after washing the ice. The percentage reduction is about 89, 92, 98 and 79 % for the control experiment and in the presence of 200, 350 and 500 mg/L antiscalant respectively. This shows that the washing of ice was quite effective due to the large particle sizes obtained which result in large interstitial spaces between the particles. The Na_2SO_4 concentration in the absence of antiscalant before washing was much lower than that in the presence of antiscalant. It would have been expected that all concentrations should have been in the neighbourhood of 1 wt. % since the bulk ice dilutes any entrained mother liquor. It is therefore apparent that the higher concentrations obtained in the presence of antiscalant were a result of salt entrainment in ice as discussed in section 5.3.2. During the experiments, it was also observed visually that salt entrainment in ice was more severe in the presence of antiscalant than in the control experiment. The author proposed that this could be due to adsorbed antiscalant molecules which formed bridges between the ice and salt particles or surface roughening of ice particles which allowed entrapment of salt particles.

It is also noted that the Na_2SO_4 concentration in ice after washing is much higher in the presence of 500 mg/L antiscalant. This has been attributed to the rough surface of the ice particles obtained which tend to entrap salt crystals within the ice bed during filtration and washing. It is probable that with an increase in washing cycles, higher ice purities could be obtained.

Figure 5-11 shows the phosphorus concentration in the presence of 200, 350 and 500 mg/L antiscalant before and after washing the ice with 100 g of deionised water maintained at about 1 ˚C.

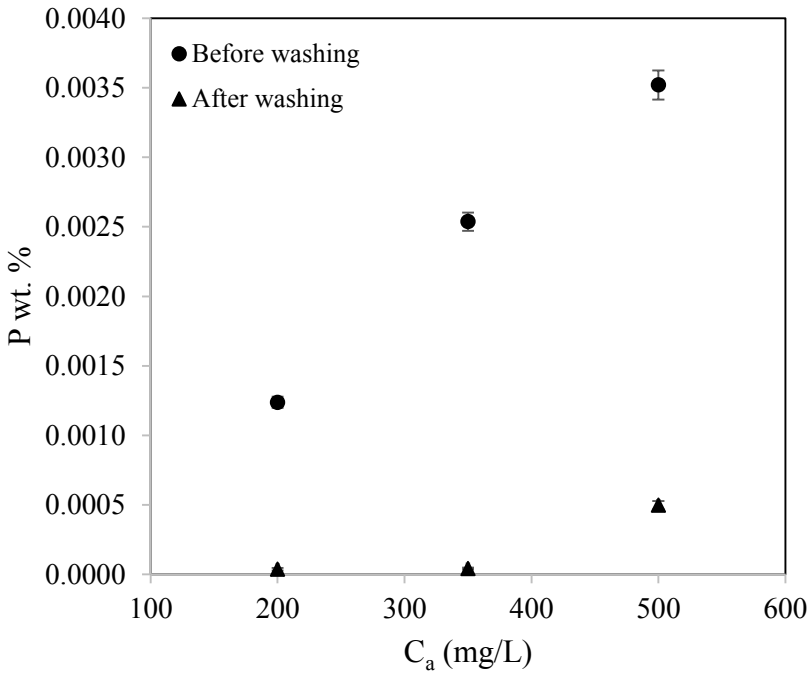

Figure 5-11. Variation of phosphorus concentration with antiscalant concentration

Figure 5-11 shows that the phosphorus concentration in ice increased with increasing antiscalant concentration. There was also a significant reduction in phosphorus concentration before and after washing, averaging about 94 %. However, it is not obvious that the remaining impurities after washing were incorporated into the crystal lattice. There is a possibility that these impurities were still entrapped in the interstitial spaces within the ice bed during filtration and washing or they were still adsorbed on the ice particle surfaces. Since a high reduction in phosphorus content was obtained upon washing, it is highly likely that the mechanism by which the antiscalant molecules adsorbed on the ice particles is physisorption. An increase in the number of washing cycles could possibly reduce the phosphorus concentration in ice although this would lead to poor ice yield.

Figure 5-12 shows the purity of ice before and after washing in the absence and presence of 200, 350 and 500 mg/L antiscalant.

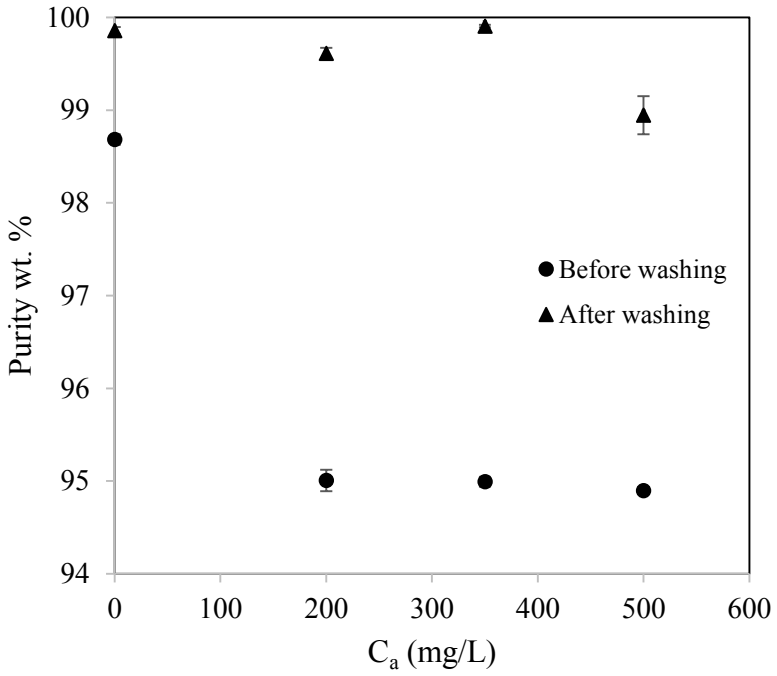

Figure 5-12. Purity of ice in the absence and presence of 200, 350 and 500 mg/L antiscalant

Ice purity was calculated taking into account both Na_2SO_4 and phosphorus concentration in the ice samples. The average purities obtained before and after washing are about 95.9 and 99.6 wt. %. An additional washing cycle could possibly achieve higher purity of the ice, although this provokes a higher loss of ice product.

5.4 Effect of the antiscalant on $Na_2SO_4.10H_2O$ crystallization

Continuous EFC experiments were conducted to determine the effect of different antiscalant concentrations in the range of 200 to 500 mg/L on the CSD, crystallization kinetics and quality parameters of $Na_2SO_4.10H_2O$ under eutectic conditions. Results on these parameters are therefore presented and discussed in subsequent sub-sections.

5.4.1 Effect of the antiscalant on CSD and crystallization kinetics of $Na_2SO_4.10H_2O$

Crystallization kinetics data was obtained from the CSDs in the absence and presence of different antiscalant concentrations by plotting a semi-logarithmic graph of the crystal population density (n) against crystal size (L) as shown in appendix 2. It was deduced that steady state with respect to solution concentration and CSD was attained after 3τ and only CSDs obtained from images captured at 4τ, 5τ and 6τ were considered. Huige (1972) also

attained steady state conditions at times slightly longer than 3τ. The attainment of steady state conditions is shown in concentration and CSD profiles in appendix 1.

5.4.1.1 Crystal Size Distribution (CSD)

Figure 5-13 shows the CSDs obtained in the control experiment and in the presence of 200, 350 and 500 mg/L antiscalant.

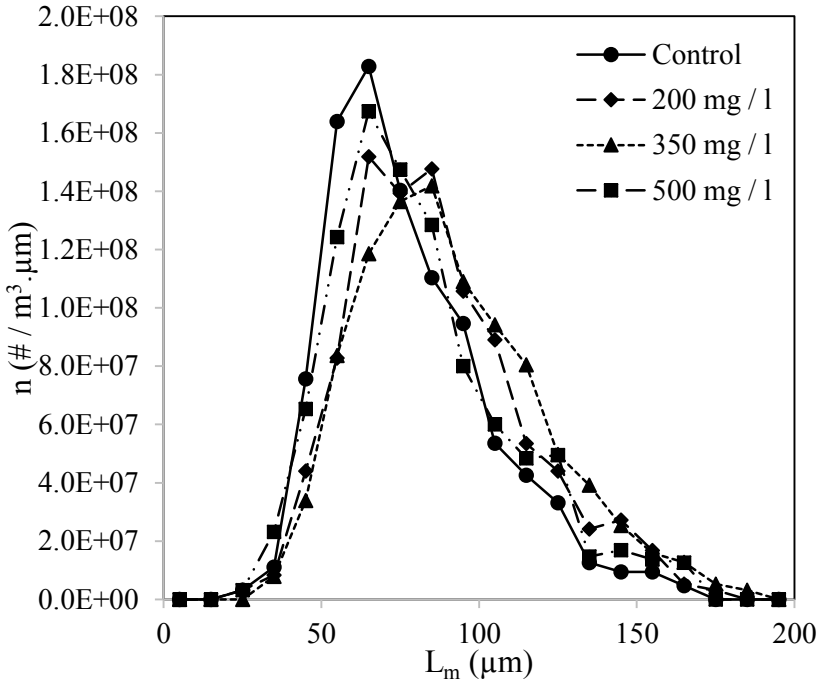

Figure 5-13. CSDs of $Na_2SO_4.10H_2O$ in the absence and presence of 200, 350 and 500 mg/L antiscalant

It can be seen on the plot that the presence of 200 and 350 mg/L antiscalant caused a slight skewness of the CSD to the right resulting in an increase of the modal crystal size from 62.87 ± 5.28 µm to 66.73 ± 4.53 µm and 76.04 ± 3.36 µm respectively as depicted in Figure 5-14. Values of the mean, median and modal crystal sizes are tabulated in appendix 3.

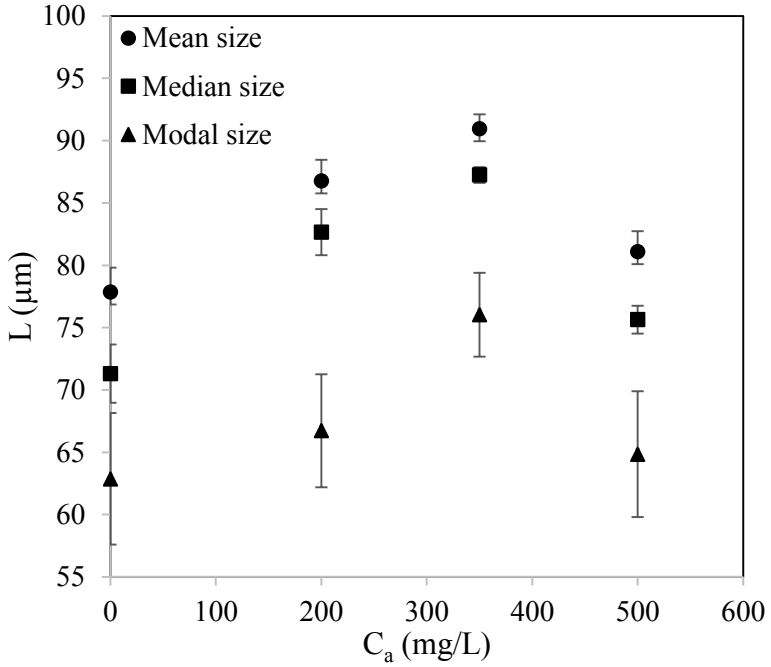

Figure 5-14. Mean, median and modal crystal sizes of $Na_2SO_4.10H_2O$ in the absence and presence of 200, 350 and 500 mg/L antiscalant

Increasing the antiscalant concentration to 500 mg/L resulted in restoration of the CSD obtained in the control experiment, giving a modal size of 64.84 ± 5.04 µm. Despite the overlapping error bars, the trend in the modal crystal size can be authenticated by the fact that it resembles the trend observed in mean and median crystal sizes.

The mean crystal size increased from 77.85 ± 1.97 µm to 86.77 ± 1.69 µm in the absence and presence of 200 mg/L antiscalant respectively. An antiscalant concentration of 350 mg/L further increased the mean size to 90.96 ± 1.16 µm after which it diminished to 81.09 ± 1.66 µm in the presence of 500 mg/L antiscalant.

The median crystal size was also observed to increase from 71.30 ± 2.35 µm to 82.66 ± 1.84 µm and 87.24 ± 0.63 µm in the absence and presence of 200 and 350 mg/L antiscalant respectively. Thereafter, it dropped to 75.64 ± 1.12 µm in the presence of 500 mg/L antiscalant. Since the trend in the mean and median crystal sizes appear to be significant, this suggests a turning point in the effect of the antiscalant on these parameters. This can be termed a threshold antiscalant concentration beyond which the effect is reversed and it lies between 350 and 500 mg/L. A similar phenomenon has been observed for ice in Figure 5-5 although the trends are not similar.

Antiscalants, amongst other additives and impurities, are known to alter crystallization kinetics by adsorption on crystal surfaces thereby affecting the surface properties. According to Veintimillas-Verdaquer (1996), the effect of impurities is more pronounced on crystal surface properties than on the bulk properties. The increase in the mean and median crystal sizes observed is most likely caused by adsorption of the antiscalant molecules on $Na_2SO_4.10H_2O$ crystal surfaces. This implies that in the range of antiscalant concentrations of 200 – 350 mg/L, adsorption of antiscalant molecules on crystal surfaces reduced the surface incorporation energy for incorporation of solute molecules into the crystal lattice. This usually occurs if there is a high degree of structural matching between the crystal molecular structure and the impurity molecules. The molecular structure of the phosphonate based antiscalant under investigation could not be obtained. The only information available is that it could be a one-chained long molecular alkyl phosphonate, or it could be a mixture of different phosphonate species. However, Ruiz-Agudo and co-workers (2006) showed that the phosphonic acids, ATMP and DTPMP, had a good structural matching with the {100} faces of $Na_2SO_4.10H_2O$, thereby promoting adsorption on these faces. This could not be validated in this investigation since there was no change in morphology. The phenomenon of the reduction in surface incorporation energy of $Na_2SO_4.10H_2O$ crystal surfaces as suggested, at antiscalant concentrations below 350 mg/L, is not well understood and requires further investigation.

It is also proposed that below the antiscalant concentration of 350 mg/L, the phosphonate molecules could have repelled water molecules at the solid-liquid interface, thereby promoting surface diffusion of solute molecules on the crystal surfaces. Through molecular dynamic simulation, Yang and co-workers (2013) proved that the growth retardation of the L-alanine {100} face in the presence of L-valine at concentrations below 0.1 wt. %, was due to reduction in molecular surface diffusion caused by the hydration layer around L-alanine molecules. At L-valine concentrations greater than 0.2 wt. %, growth promotion was observed due to repulsion of water molecules which formed the hydration layer around solute molecules at the solid-liquid interface. However, in this investigation, growth promotion was observed at antiscalant concentrations below 350 mg/L (0.035 wt. %) and Yang and co-workers (2013) observed growth promotion at impurity concentrations above 0.2 wt. %.

It could be possible that beyond a threshold antiscalant concentration between 350 and 500 mg/L, adsorption of the antiscalant molecules on the crystal surfaces and possibly, kink sites, became more pronounced. This means that, at antiscalant concentrations beyond 350 mg/L,

there was an increase in surface adsorption and / or lattice incorporation energies which resulted in reduction of the mean and median crystal sizes. As the moles of antiscalant increase, so does the extent of surface coverage, possibly resulting in lattice incorporation of the antiscalant molecules. This disrupts surface diffusion and incorporation of solute molecules into the crystal lattice. Molecular modelling conducted by Poornachary and co-workers (2008) proved that adsorption of impurity molecules on crystal surfaces can modify the surface energy for integration of solute molecules into the lattice. This is in agreement with the Bliznakov model which suggests that solubility is not altered, but rather, surface incorporation of solute molecules is reduced due to temporary blockage of kink sites.

It is proposed that as the antiscalant concentration increases, there is a change in the mechanism by which antiscalants function. At concentrations below 350 mg/L, the mechanisms that are most likely dominant are incorporation and / or surfaction. Yang et al., (2013) observed an increase in facial growth rate of L-alanine beyond a threshold impurity concentration.

It is further proposed that, at antiscalant concentrations beyond 350 mg/L, the Bliznakov model becomes dominant resulting in temporary blockage and reduction of available kink sites (Shtukenberg et al., 2014). The kinetic co-efficient of molecular attachment is lowered due to the increase in surface adsorption and / or lattice incorporation energies.

The range of antiscalant concentrations investigated is quite small corresponding to 0.02 to 0.05 wt. %. This rules out the possibility of chelation (Liu and Nancollas, 1973) of Na^+ ions by antiscalant molecules. In any case, if this occurs, it would result in reduction in the mean and median crystal sizes for the entire range of concentrations tested, due to the reduction in available Na^+ ions.

The CSDs shown in Figure 5-13 were characterized by the Co-efficient of Variation (CV). Figure 5-15 shows the CVs for CSDs obtained in the absence and presence of 200, 350 and 500 mg/L antiscalant.

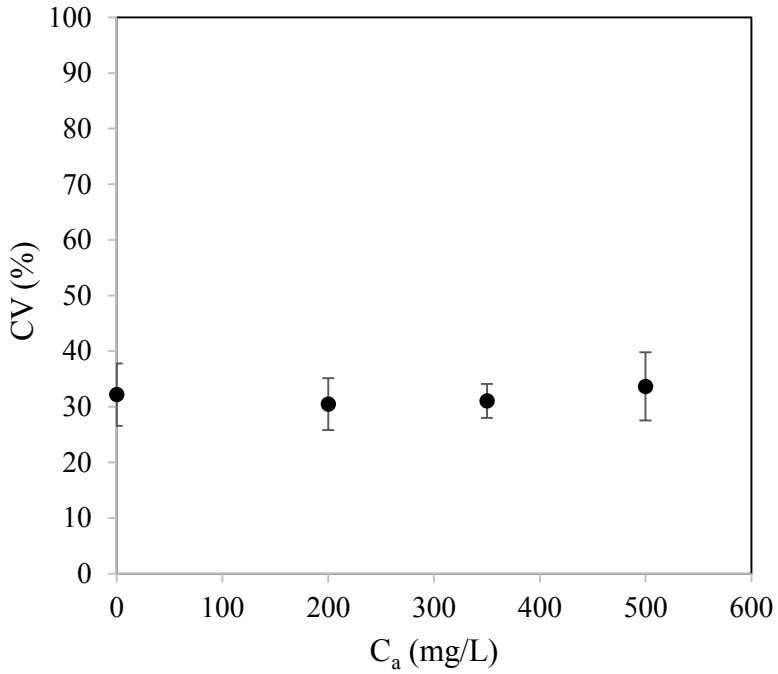

Figure 5-15. CVs for CSDs in the absence and presence of 200, 350 and 500 mg/L antiscalant

Values for the CVs are tabulated in appendix 4. The CVs in the absence and presence of 200, 350 and 500 mg/L antiscalant were almost similar as shown by the overlapping error bars. The mean CV was computed to be 31.85 ± 3.79 % which is well below the expected CV of about 50 % for a product from an MSMPR crystallizer (Mullin, 2001). The smallest salt crystal size obtained during CSD analysis was 32.29 ± 1.55 µm and the largest size obtained was 171.18 ± 2.32 µm. These crystal sizes are within the range obtained for $Na_2SO_4.10H_2O$ in batch EFC experiments by Reddy and co-workers (2010).

5.4.1.2 Nucleation rate

The nucleation rate values were obtained from Equation 2-2 in which the parameter, n_o, is the intercept of a semi-logarithmic plot of the crystal population density against crystal size. The linear trend lines fitted for crystal sizes above 55 µm were extrapolated to obtain the intercept. Although, this would not accurately predict the nucleation rates, the extrapolation method was adopted to obtain arbitrary nucleation rates for comparison purposes. An example of the semi-logarithmic plot obtained is shown in appendix 2. Further details of this evaluation method are given in section 5.4.1.3. Figure 5-16 shows the variation of the nucleation rate with increase in antiscalant concentration.

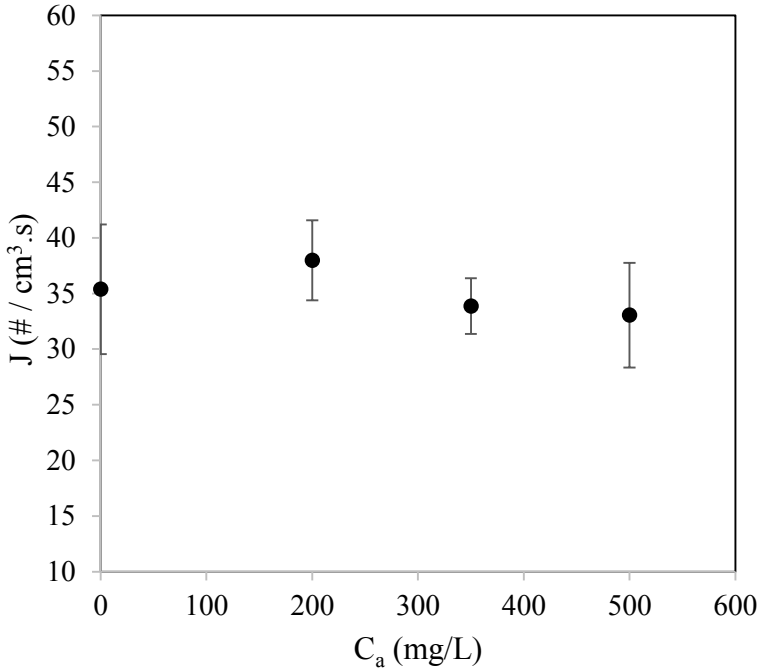

Figure 5-16. Nucleation rates of $Na_2SO_4.10H_2O$ in the absence and presence of 200, 350 and 500 mg/L antiscalant

Figure 5-16 shows that there is no significant change in nucleation rate since the error bars overlap. The nucleation rates obtained for the control experiment and experiments in the presence of 200, 350 and 500 mg/L antiscalant are 35.39 ± 5.83, 37.98 ± 3.59, 33.86 ± 2.50 and 33.05 ± 4.70 measured in # / (cm^3.s) respectively as shown in appendix 4. It was expected that a decrease in the nucleation rate coupled with an increase in the growth rate due to reduced crystal surface area, or a null change in nucleation rate coupled with an increase in growth rate due to increase in the growth rate kinetic co-efficient would be the most probable reasons for the observed increase in mean and median sizes. Since there was no significant change in the nucleation rate of salt, an increase in growth rate due to an increase in the growth kinetic co-efficient would explain the trend shown in Figure 5-14 for antiscalant concentrations below 350 mg/L. The increase in the growth kinetic co-efficient is most likely caused by a reduction in the lattice incorporation energy required for solute molecular attachment.

A constant supercooling of 0.04 ˚C was maintained in all experiments using a PT100 temperature sensor with an accuracy of ± 0.01 ˚C. An agitation rate of 180 rpm was used in all experiments and it can be assumed that the hydrodynamic conditions in the crystallizer were similar in all experiments conducted.

5.4.1.3 Growth rate

The growth rate values were obtained from the gradient of the semi-logarithmic plots of the crystal population density against crystal size as shown in Appendix 2. It can be noted that although the points of the semi-logarithmic plots for crystal sizes greater than 55 μm seem to show a linear trend, the R^2 values for the linear trend lines were low averaging to 88.26 ± 4.57 %. However, despite such rather low R^2 values, these lines of best fit were adopted for comparison of growth rate values in the absence and presence of different antiscalant concentrations.

The trend line was not fitted to sizes below 55 μm since the positive gradient obtained in this section of the curve suggested negative growth. The reason for this phenomenon is not quite clear. However, this could have been due to crystal breakages. Figure 5-17 shows the variation in growth rate as a function of antiscalant concentration.

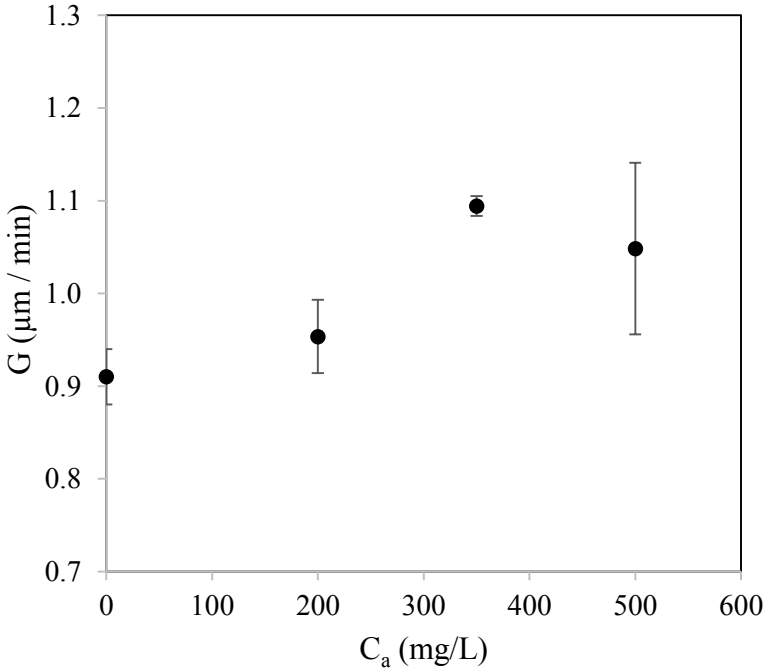

Figure 5-17. Growth rates of $Na_2SO_4.10H_2O$ in the absence and presence of 200, 350 and 500 mg/L antiscalant

Figure 5-17 shows a general increase in the growth rate up to an antiscalant concentration of 350 mg/L followed by a decline at an antiscalant concentration of 500 mg/L. This is consistent with the trend observed for the mean and median crystal sizes. The growth rate values obtained in the control experiment and experiments with 200, 350 and 500 mg/L

antiscalant are 0.91 ± 0.03, 0.95 ± 0.04, 1.09 ± 0.01 and 1.05 ± 0.09 μm / min respectively as tabulated in appendix 4.

The trend shown suggests that, at antiscalant concentrations below 350 mg/L, adsorption of antiscalant molecules on crystal surfaces promotes growth of the crystals. Furthermore, adsorption at an antiscalant concentration of 500 mg/L retards growth of crystals implying a turning point between 350 and 500 mg/L antiscalant concentration. As discussed in section 5.4.1.1, the increase in growth rate up to an antiscalant concentration of 350 mg/L, is attributed to two phenomena. The first one is that adsorption of antiscalant molecules on $Na_2SO_4.10H_2O$ surfaces resulted in reduction of the lattice incorporation energy required for molecular attachment of solute molecules into the lattice. This most likely occurs by surfaction as discussed earlier. Liu and Nancollas (1973) attributed the increase in $Ca_2SO_4.2H_2O$ crystal growth observed with increase in NTMP concentration to creation of favourable growth sites as a result of adsorption of additive molecules on crystal surfaces. Sangwal (1996) also highlighted that impurity clusters on crystal surfaces can provide additional growth steps thereby promoting crystal growth.

The second one is that the antiscalant molecules could have repelled water molecules on the solid-liquid interface thereby promoting surface diffusion of solute molecules. However, with increase in antiscalant concentration to 500 mg/L, the surface coverage due to adsorption would block favourable growth sites, thereby retarding growth. The reduction in growth rate at an antiscalant concentration of 500 mg/L implies an increase in the lattice incorporation energy due to blockage and reduction of available kink sites. Vavouraki and Koutsoukos (2012) observed that at low relative supersaturation such as the one employed in this investigation, growth of $Na_2SO_4.10H_2O$ is surface diffusion or integration controlled in line with the BCF model (Myerson, 2002). This implies that impurities are most likely to disrupt the surface diffusion and integration of solute molecules into the crystal lattice.

Alternatively, there appears to be a strong interdependence between the crystallization kinetics of ice and salt. It was observed in Figure 5-7 and Figure 5-8 that the ice nucleation rate decreased and there was a general increase in ice growth rate up to an antiscalant concentration of 350 mg/L. Since constant supercooling was maintained throughout all experiments and ice nucleation was reduced by the action of antiscalant on ice nuclei, it follows that the available supersaturation was consumed by growth of ice. The growth promotion of ice implies that the operating point shifted to the right of the eutectic point,

thereby increasing the supersaturation for salt crystallization. The fact that the salt nucleation rate was not affected by the presence of the antiscalant means that, possibly, the antiscalant interacted more on ice nuclei surfaces than on salt nuclei surfaces. This implies that the growth promotion observed for salt up to antiscalant concentrations of 350 mg/L could be due to increase in supersaturation induced indirectly, by the increase in ice growth rate.

It is possible that beyond an antiscalant concentration of 350 mg/L, the effect of the antiscalant on salt crystal surface properties became more pronounced. The most likely mechanism of antiscalant action is the Bliznakov model. Impurities can affect the growth rate by altering the crystal surface adsorption energy for solute molecules, the mobility of solute molecules on the surface, the attachment and / or detachment of solute molecules at kink sites as well as the lattice incorporation of solute molecules. A turning point was also observed by Rauls and co-workers (2000) in which the nucleation and growth rates of $(NH_4)_2SO_4$ passed through a minimum and maximum at an Al^{3+} additive concentration of 50 ppm respectively. However, this was attributed to increase in supersaturation or reduction in solubility caused by the additive.

It was also observed that the pH of the solution increased with increasing antiscalant concentration from 6.5 ± 0.2 to 8.2 ± 0.1 in the absence and presence of 500 mg/L antiscalant as shown in appendix 5. Several authors reported an increase in phosphonate inhibitory efficiency with increase in solution pH in the alkaline range (Weijnen et al., 1983; Black et al., 1991; Ruiz-Agudo et al., 2006). This was attributed to full dissociation or deprotonation of the additive molecules under alkaline conditions. A similar phenomenon could have occurred in this investigation at the high pH value of 8.2 obtained in the presence of 500 mg/L. This could have resulted in stronger electrostatic bonds between the negatively charged phosphonate ions, PO_3^{2-} and the positively charged cations on the crystal surfaces. The pH values in the presence of 200 and 350 mg/L antiscalant are almost neutral, averaging about 7.3. Under these conditions, the phosphonate molecules would not completely dissociate, implying weaker electrostatic attractive forces.

This shows that the interaction between the antiscalant molecules and surface ions is of electrostatic nature. Consequently, adsorption most likely occurred by physisorption. As the number of antiscalant molecules that adsorb on crystal surfaces increases, it is highly likely that solute molecules are hindered from adsorbing onto the crystal surfaces due to increase in surface adsorption and incorporation energies. The effect of an impurity on crystallization

kinetics is highly unpredictable since it depends partly on the modification of crystal surface properties and partly on the modification of bulk solution properties.

5.4.2 Effect of the antiscalant on morphology of $Na_2SO_4.10H_2O$

Figure 5-18 shows the morphology of $Na_2SO_4.10H_2O$ crystals obtained in the absence and presence of 200, 350 and 500 mg/L antiscalant.

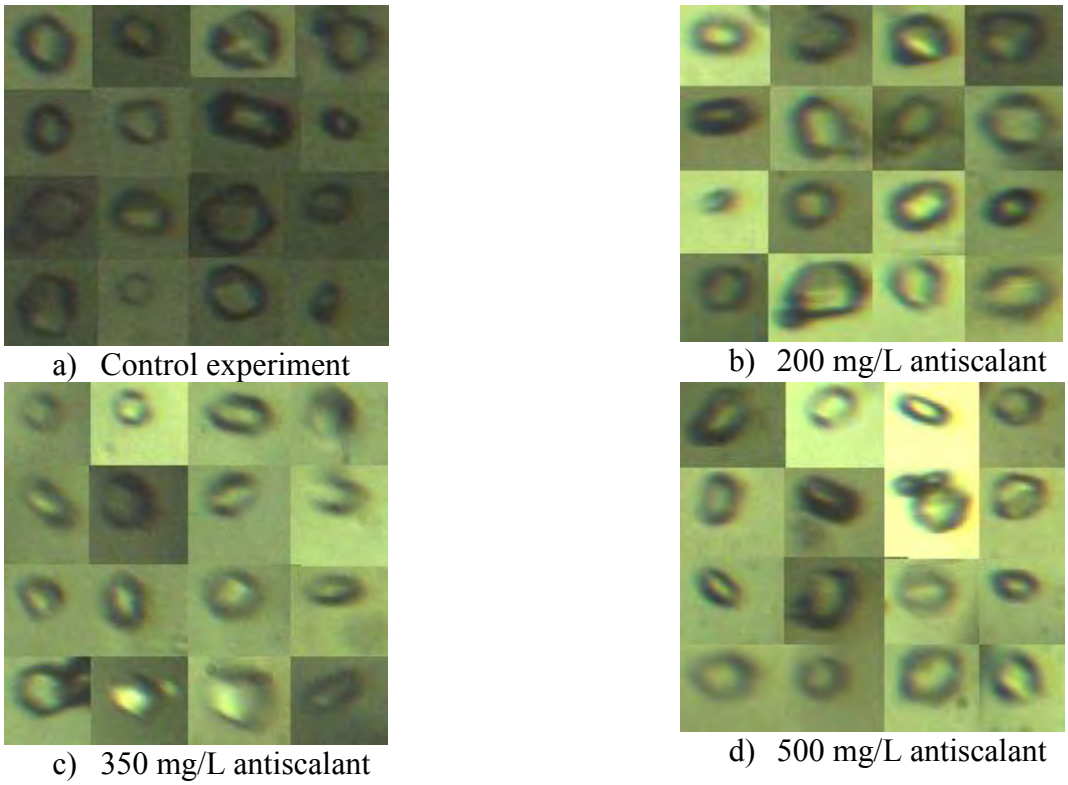

a) Control experiment

b) 200 mg/L antiscalant

c) 350 mg/L antiscalant

d) 500 mg/L antiscalant

Figure 5-18. Morphology of $Na_2SO_4.10H_2O$ in the absence and presence of 200, 350 and 500 mg/L antiscalant

There was no observable change in morphology with increase in antiscalant concentration. In each set of crystal images presented, it can be seen that the dominant shape is a monoclinic of hexagonal structure. The monoclinic shape has been reported for $Na_2SO_4.10H_2O$ (Plessen and Aktiengesellschaft, 2005; Reddy et al., 2010). Although, it is known that the impurity molecules adsorb preferentially on specific crystal faces where the adsorption energy is minimum, the fact that there was no marked change in morphology suggests that the adsorption of antiscalant molecules must have occurred evenly on all crystal faces and it was reversible. The occurrence of adsorption is substantiated by the change in the mean and median sizes as well as the change in growth rate. In an investigation by Ruiz-Agudo and co-workers (2006), one phosphonic acid with two functional groups did not change the

morphology of $Na_2SO_4.10H_2O$ crystals, whereas two of the phosphonic acids with three and five functional groups changed the morphology at moderately alkaline pH values. This is supported by Black and co-workers (1991) who observed that phosphonates did not cause any morphological changes to $BaSO_4$ crystals at lower pH values.

Figure 5-19 shows the variation of the aspect ratio of crystals obtained in the control experiment and in the presence of 200, 350 and 500 mg/L.

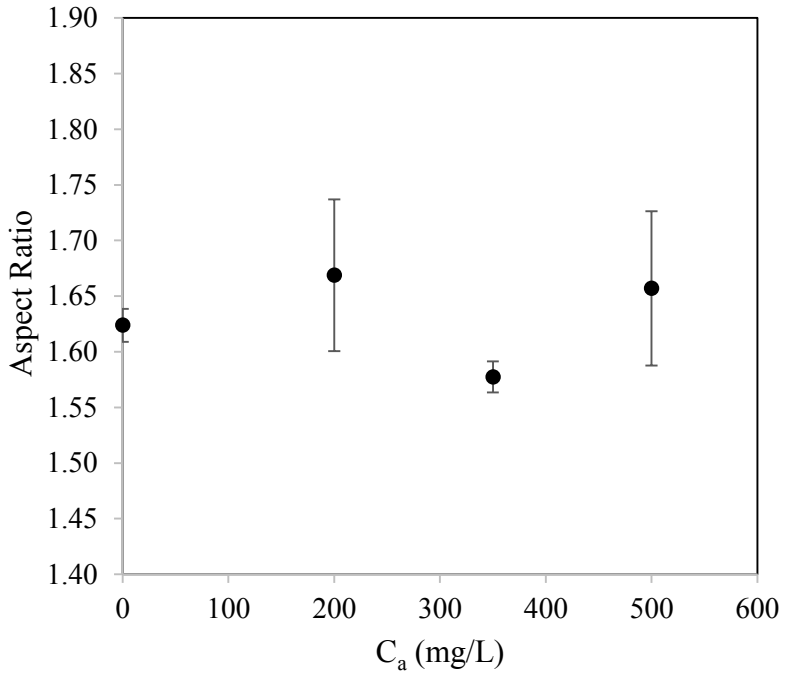

Figure 5-19. Variation of $Na_2SO_4.10H_2O$ crystal aspect ratio in the absence and presence of 200, 350 and 500 mg/L antiscalant

The changes in aspect ratio observed lie within experimental error since the error bars overlap. This substantiates the fact that there was no change in morphology due to preferential adsorption of antiscalant molecules on specific crystal surfaces.

5.4.3 Impurity concentration in salt samples

Figure 5-20 shows the variation of phosphorus concentration wt. % in salt with increase in antiscalant concentration before and after washing with 50 g of saturated Na_2SO_4 aqueous solution.

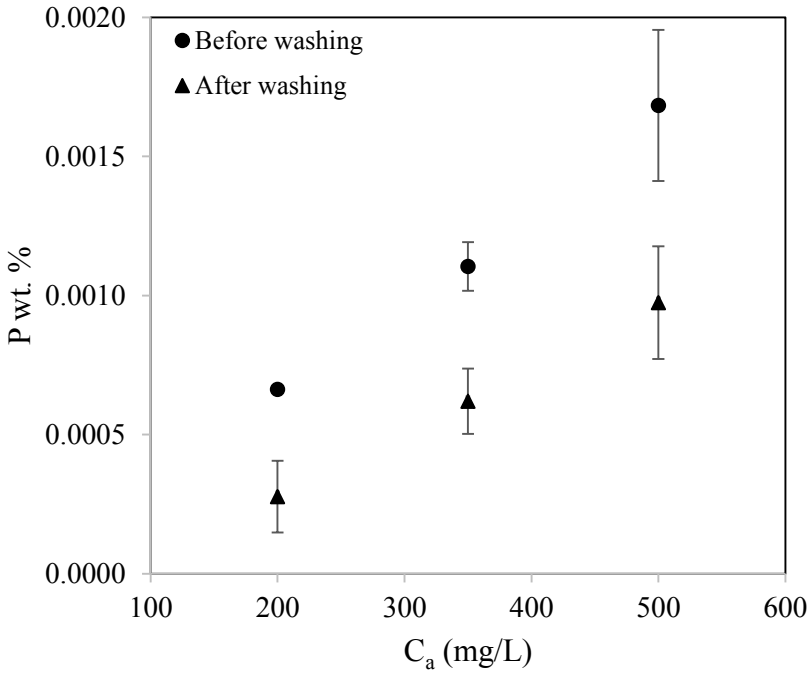

Figure 5-20. Variation of phosphorus concentration in salt in the presence of 200, 350 and 500 mg/L antiscalant

Figure 5-20 shows an increase in phosphorus concentration in the salt as the antiscalant concentration increases. It also shows a reduction in the phosphorus concentration after washing with 50 g of the saturated solution. The average phosphorus concentration reduction obtained is about 50 %. However, it cannot be deduced whether the remaining impurities were incorporated into the crystal lattice or they were entrapped in the voids of the salt bed during filtration. An increase in washing cycles could possibly further reduce the phosphorus content in the salt.

The increase in phosphorus concentration with increasing antiscalant concentration shows that there is a high possibility of antiscalant adsorption on crystal surfaces. Incorporation is less likely to occur if the impurity molecules adsorb temporarily. Since, washing was effective in reducing the phosphorus content of the salt, it can be deduced that the antiscalant molecules adsorbed on salt crystal surfaces by physisorption.

5.5 Implications on EFC and filtration

A general increase in the growth rate of both ice and salt crystals was observed in the presence of the antiscalant. The ice nucleation rate was observed to decrease in the presence of the antiscalant and no change in salt nucleation rate was observed. This is consistent with the larger mean crystal sizes obtained for salt in the presence of antiscalant. The mean ice particle size decreased in the presence of 200 mg/L after which it increased.

The changes observed do not warrant an increase in the hydraulic residence time and / or supercooling in the presence of the antiscalant. The parameters employed in the pure binary system can still be adopted in the application of EFC to treat a Na_2SO_4 aqueous solution containing phosphonate antiscalant concentrations below 500 mg/L. Although the ice modal particle size diminished significantly in the presence of 200 mg/L and 350 mg/L antiscalant, it is anticipated that this would not reduce downstream filtration efficiency to a greater extent. This is substantiated by the huge reduction in impurity content in ice upon filtering and washing. Since the morphology of salt crystals was not altered, it is anticipated that the filtration efficiency for salt in the absence and in the presence of the phosphonate antiscalant would be similar.

However, salt entrainment was more severe in the presence of the antiscalant suggesting that the antiscalant promoted it, although there is not enough evidence to prove this. This could adversely affect the separation efficiency of ice and salt in the crystallizer. However, high purities were obtained after washing and it is possible that with increase in washing cycles, higher purities could be obtained. An increase in washing cycles would reduce the ice yield due to melting. Therefore, a trade-off is required that ensures high purities without depleting the yield significantly.

6 Conclusions

Previous research focused on the effect of impurities in batch cooling and evaporative crystallization where only one crystal species was formed at ambient to high temperatures. In addition, there is little information in literature on the effect of phosphonates on the crystallization of ice and alkali earth metal salts as well as the effect of other organic impurities on ice crystallization. This study sought to close this gap in knowledge by determining the effect of different phosphonate antiscalant concentrations in the typical range of RO brine streams on the crystallization kinetics of both ice and $Na_2SO_4.10H_2O$ in a continuous EFC process. In addition, the effect of the antiscalant on the phase equilibria of a binary aqueous Na_2SO_4 solution and product quality parameters, such as the CSD, morphology and purity were investigated. The novelty of this study lies on the fact that EFC is a rather novel separation technique and establishing the effect of impurities on the crystallization kinetics of both ice and salt would facilitate the design of an efficient EFC process suitable for treatment of a diverse of wastewater streams. To the best of the author's knowledge, this is the first time an investigation has been conducted on the effect of a phosphonate antiscalant on both ice and $Na_2SO_4.10H_2O$ crystallization during EFC.

It was concluded that the antiscalant had a negligible effect on both the freezing point depression of water in hypoeutectic solutions and the salt solubility in hypereutectic solutions. This was attributed to the minute antiscalant concentrations tested as well as possible reversible adsorption of antiscalant molecules on particle surfaces.

The presence of antiscalant in concentrations up to 350 mg/L decreased the ice nucleation rate and a reversal on this effect was observed in the presence of 500 mg/L antiscalant. This was attributed to adsorption of the antiscalant molecules on ice nuclei surfaces, thereby retarding the growth of the nuclei into critical sizes. On the other hand, the salt nucleation rate remained almost constant over the entire range of antiscalant concentrations investigated. This implies that the antiscalant had a greater effect on ice nucleation than on salt nucleation.

A general increase in the growth rate of ice for antiscalant concentrations of 350 and 500 mg/L was observed. This trend was consistent with the trend observed for the mean and median particle sizes. The increase in salt growth rate for up to an antiscalant concentration of 350 mg/L could have occurred due to a direct or an indirect effect of the antiscalant. The antiscalant molecules could have adsorbed on ice particles resulting in reduction of the

surface adsorption and / or lattice incorporation energy. This phenomenon requires further investigations. Alternatively, the decrease in the nucleation rate of ice accompanied by an increase in the ice growth rate could have raised the supersaturation for salt crystallization. This could have promoted the growth of salt in the presence of antiscalant concentrations up to 350 mg/L.

The change in ice morphology could not be observed owing to the high tendency of ice to agglomerate. Individual crystals could not be identified in the agglomerates. However, in the presence of the antiscalant, it was observed that the ice particle surfaces roughened. It was proposed that the antiscalant molecules served as bridges between the ice particles and salt crystals as a result of hydrogen bonding or electrostatic interactions. However, further investigations are required to validate this. There was no change observed in the morphology of salt. The salt crystals in the absence and presence of antiscalant had a monoclinic shape of hexagonal structure.

The salt entrainment observed is validated by higher Na_2SO_4 concentrations obtained in ice before washing in the presence of the antiscalant. The phosphorus concentration in ice increased with increase in antiscalant concentration before and after washing. It was noted that washing effectively removed the impurities. The phosphorus content in ice decreased by about 94 % to values below 0.0005 wt. % after washing. However, it could not be ascertained whether the remaining phosphorus after washing indicated incorporation into the lattice or it could have been trapped in the voids of the ice bed during filtration and washing. The phosphorus content in salt after washing was in the range 0.0002 to 0.0009 wt. %.

Overall, it can be deduced that, in the range of antiscalant concentrations of 200 – 500 mg/L, the effect of the antiscalant on the crystallization kinetics of both ice and salt was not very severe to warrant significant changes in operating parameters such as supercooling and residence time. The objectives of this research were fully met and it was proven that the presence of minute concentrations of a phosphonate antiscalant has an effect on the crystallization kinetics of both ice and salt in EFC. It should be noted, however, that there were a few research limitations encountered in this study. The magnification factors employed as discussed in Section 4.3.1.3 did not allow measurement of crystal sizes below about 30 µm and 100 µm for salt and ice respectively. This reduces the accuracy of the CSD, hence the reliability of the kinetic data evaluated. Secondly, it was difficult to identify whether the ice particles were agglomerates or individual crystals due to their surface

roughness and irregularity in shape. This also reduces the accuracy of ice crystallization kinetics evaluated. On the contrary, CSD analyses for salt was more accurate since salt crystals were regularly shaped and could be identified clearly and individually. Determination of the actual phosphonate molecular composition of the antiscalant could not be achieved. However, the study confirmed the presence of a phosphonate functional group in the antiscalant.

7 Recommendations

It is recommended to conduct further investigations using a real RO brine stream which contains a diverse of organic and inorganic impurities. Although the antiscalant did not cause a significant adverse effect on the crystallization kinetics of ice and salt from a Na_2SO_4 aqueous synthetic solution, it is quite possible that other impurities in a real brine could have a significant effect on the crystallization kinetics in EFC, hence product quality. Such information is essential to determine the operating conditions, such as, supercooling and residence time, to be employed for the real brine in order to counter the effect of the impurities. It would also provide an insight into the effect on the downstream process of filtration.

Future investigations should involve determination of adsorption energies in order to validate the occurrence of adsorption and quantify the adsorption affinities of solute and impurity molecules on crystal surfaces. There is likely to be preferential adsorption of the impurity molecules on the two crystal species in EFC and measurement of the respective adsorption energies would provide a better understanding of the mechanisms by which the impurity molecules interact with the crystal surfaces.

A higher resolution is also required in the in-situ digital imaging technique employed in this investigation in order to account for smaller particle sizes in CSD analysis. This would certainly improve the accuracy in the evaluation of the nucleation and growth rates using the steady-state population balance equation given in Section 2.4.

8 References

Akyol, E., Oner, M., Barouda, E. & Demadis, K.D. 2009. Systematic structural determinants of the effects of tetra phosphonates on gypsum crystallization. *Crystal growth and design.* 9:5145-5154.

Al-Jibbouri, S. & Ulrich, J. 2001. The effect of impurities on crystallization kinetics of sodium chloride. *Crystal Research and Technology.* 36(12):1365-1375.

Arai, S., Watanabe, M. &Tsuji, R. F. 1984. Enzymatically modified gelatin as an antifreeze protein. *Agricultural and biological chemistry*. 48 (8): 2173 – 2175.

Arellano, M., Aguilera, J., & Bouchon, P. 2004. Development of a digital video-microscopy technique to study lactose crystallization kinetic in situ. *Carbohydrate research.* 339(16): 2721-30

Atkins, P. & Paula, J. 2014. Atkin's physical chemistry. Oxford: Oxford University press

Black, S. N., Bromley, L. A., Cottier, D., Davey, R. J., Dobbs, B. & Rout, J. E. 1991. Interactions at the organic / inorganic interface: Binding motifs for phosphonates at the surface of barite crystals. *Journal of the Chemical Society, Faraday Transactions.* 87(20): 3409-3414

Brand, H. E. A., Fortes, A. D., Wood, I. G., Knight, K. S. & Vocadlo, L., 2008. The thermal expansion and crystal structure of mirabilite ($Na_2SO_4.10H_2O$) from 4.2 to 300 K, determined by time-of-flight neutron powder diffraction. *Physics and Chemistry of Minerals*. 36 (1): 29-46

Brecevic, L. & Garside, J. 1981. On the measurement of crystal size distributions in the micrometre size range. *Chemical Engineering Science*. 36: 867-869

Chivavava, J., Rodriguez-Pascual, M. & Lewis, A. 2014. Effect of operating conditions on ice characteristics in continuous eutectic freeze crystallization. *Chemical Engineering and Technology*. 37(8): 1314-1320

Damodaran, S. 2007. Inhibition of ice crystal growth in ice cream mix by gelatin hydrolysate. *Journal of Agricultural Food and Chemistry*. 55: 10918-10923

Denecker, M. F. C., Hebert, R. L. & Wassermann. 2014. Experimental study of the crystallization of sodium sulphate hydrates through temperature monitoring. *Environmental Earth Sciences*. 71(12)

De Yoreo, J. J. & Velikov, P. G. 2003. *Bio mineralization - Reviews in Mineralogy and Geochemistry: Principles of Crystal Nucleation and Growth*. Volume 54. Mineralogical Society of America

Ferreira, A., Faria, N., Rocha, F., Feyo de Azevedo, S. & Lopes, A. 2005. Using image analysis to look into the effect of impurity concentration in NaCl crystallization. *Chemical Engineering Research and Design*. 83(4): 331-338

Fischer, K. 1993. Distribution and elimination of HEDP in aquatic test systems, *Water Research*, 27 (1): 485 – 493.

Gardner, G. L. & Nancollas, G. H. 1983. Crystal growth in aqueous solution at elevated temperatures. Barium sulphate growth kinetics. *Journal of Physics and Chemistry*. 87(8): 4699-4703

Genceli, F. E. 2008. *Scaling-up Eutectic Freeze Crystallization. Masters in Chemical Engineering*. Instanbul Technical University.

Hallet, J. 1964. Experimental studies of the crystallization of supercooled water. *Journal of Atmospheric Sciences.* 21(671):681.

He, S., Kan, A. T. & Tomson, M. B. 1997. Inhibition of calcium carbonate precipitation in NaCl brines from 25 to 90°C. *Applied Geochemistry*. 14(1): 17-25

Huige, N.J., J. 1972. *Nucleation and growth of ice crystals from water and sugar solutions in continuous stirred tank crystallizers*. Eindhoven. The Netherlands.

Kashchiev, D. 2000. *Nucleation, Basic Theory with application.* Oxford: Butterworth-Heinemann.

Leung, W.H. & Nancollas, G.H. 1978. Nitrilo (methylenephosphonic acid) adsorption on barium sulphate crystals and its influence on crystal growth. *Journal of Crystal Growth*. 44(2): 163-167

Libin, Y., Zuoliang, S., Juan, D., Jianjun, Y. & Aiqun, Z. 2009. Crystallization kinetics of sodium sulfate decahydrate in an MSMPR stirred crystallizer. *Chemical Engineering Transactions*. 17: 759-764

Lide, D. R. 2005. *CRC Handbook of chemistry and physics*. New York: CRC Press LLC

Liu, S. & Nancollas, G. H. 1973. The crystal growth of calcium sulphate dihydrate in the presence of additives. *Journal of Colloid and Interface Science*. 44(3)

Liu, Y., Wang, J. K. & Wei, H. Y. 2004. Determination of crystallization kinetics in solution. *Journal of Crystal Growth*. 271(1-2): 238-244

Margolis, G., Sherwood, T., Brian, P. & Sarofim, A. 1971. The performance of a continuous well stirred ice crystallizer. *Industrial and Engineering Chemistry Research.* 10(3):439-451.

Marliacy, P., Solimando, R., Bouroukba, M. & Schuffenecker, L. 2000. Thermodynamics of crystallization of sodium sulphate decahydrate in H_2O-NaCl-Na_2SO_4: Application to $Na_2SO_4.10H_2O$-based latent heat storage materials. *Thermochimica Acta*. 344: 85-94

Melia, T. P. & Motiff, W. P. 1964. Secondary nucleation from aqueous solution. *Industrial and Engineering Chemistry Fundamentals*. 3(4): 313-317

Michaels, A., Brian, P. & Sperry, P. 1966. Impurity effects on the basal plane solidification kinetics of supercooled water. *Journal of Applied Physics.* 37(13):4649-4661.

Mullin, J. 2001. *Crystallization.* 4th ed. Oxford, U.K.: Butterworth-Heinemann.

Myerson A. S. Ed. 2002. *Handbook of Industrial Crystallization*. 2nd ed. Oxford: Butterworth-Heinemann.

Nathoo, J., Jivanji, R. & Lewis, A. E. 2009. Freezing your brines off: Eutectic freeze crystallization for brine treatment. *International Mine Water Conference*. October: 431-437

Omran, A. & King, C. 1974. Kinetics of ice crystallization in sugar solutions and fruit juices. *American Institute of Chemical Engineers Journal.* 20(4).

Patience, D. & Rawlings, J. 2001. Particle-Shape monitoring and control in crystallization processes. *American Institute of Chemical Engineers Journal.* 49(9):2125-2130.

Perry, R. & Green, D. Eds. 2007. *Perry's Chemical Engineers Handbook*. 7th ed. U.S.A.: McGraw-Hill.

Plessen, H.V. & Aktiengesellschaft, H. 1995. *Ullmann's Encyclopaedia of Industrial Chemistry: Phosphorus compounds, Organic*. John Wiley & Sons Ltd.

Poornachary, S. K., Chow, S. P. & Tan, R. B. H. 2008. Impurity effects on the growth of molecular crystals: Experiments and modelling. *Advanced Powder Technology*. 19: 459-473

Qu, H., Louhi-Kultanen, M. & Kallas, J. 2006. In-line image analysis on the effects of additives in batch cooling crystallization. *Journal of Crystal Growth.* 289:286-294.

Rauls, M., Bartosch, K., Kind, M., Kuch, St., Lacmann, R. & Mersmann, A. 2000. The influence of impurities on crystallization kinetics – a case study on ammonium sulphate. *Journal of Crystal Growth*. 213: 116 – 128.

Reddy, S., Lewis, A., Witkamp, G., Kramer, H. & Spronsen, J. 2010. Recovery of $Na_2SO_4.10H_2O$ from a reverse osmosis concentration by Eutectic Freeze Crystallization technology. *Chemical Engineering Research and Design.* 88:1153-1157.

Richardson, J., Harker, J. & Backhurst, J. 2002. *Coulson and Richardson's Chemical Engineering: Particle technology and separation processes.* 5th ed. Oxford, U.K.: Butterworth-Heinemann.

Rodriguez-Pascual, M. 2009. *Physical aspects of scraped heat exchanger crystallizers: An application in Eutectic Freeze Crystallization*. PhD Thesis. Delft University of Technology

Ruiz-Agudo, E., Rodriguez-Navarro, C. & Sebastian-Pardo, E. 2006. Sodium sulphate crystallization in the presence of phosphonates: implications in ornamental stone conservation. *Crystal Growth and Design.* 6(7):1575-1583.

Sangwal, K. 1996. Effect of impurities on crystal growth processes. *Progress in Crystal Growth and Characterization of Material*. 32(1-3): 3-43

Sangwal, K. 1999. Kinetic effects of impurities on the growth of single crystals from solutions. *Journal of Crystal Growth*. 203(1-2): 197-212

Sangwal, K. 2007. *Additives and crystallization processes: From fundamentals to applications.* England: John Wiley and Sons Ltd.

Selwitz, C. & Doehne, E. 2002. The evaluation of crystallization modifiers for controlling salt damage to limestone. *Journal of Cultural Heritage*. 3: 205 – 216.

Sha, Z. L., Hatakka, H., Louhi-Kultanen, M. & Palosaari, S. 1996. Crystallization kinetics of potassium sulfate in an MSMPR stirred crystallizer. *Journal of Crystal Growth*. 166(1-4): 1105-1110

Shih, W., Albrecht, K., Glater, J. & Cohen, Y. 2004. A dual-probe approach for evaluation of gypsum crystallization in response to antiscalant treatment. *Desalination.* 169:213-221.

Shtukenberg, A. G., Lee, S. S., Kahr, B. & Ward, M. D. 2014. Manipulating crystallization with additives. *Annual Review of Chemical and Bio molecular Engineering*. 5: 77-96

Shtukenberg, A. G., Punin, Y. O., Gujral, A. & Kahr, B. 2014. Growth actuated bending and twisting of single crystals. *Angewandte Chemie*. 53(3): 672-699

Stepakoff, G., Siegelman, D., Johnson, R. & Gibson, W. 1974. Development of a eutectic freezing process for brine disposal. *Desalination.* 14:25-38.

Svara, J., Weferling, N. & Hofman, T. 1995. *Ullmann's Encyclopaedia of Industrial Chemistry: Phosphorus Compounds, Organic*. John Wiley and Sons Ltd.

Uba, S. & Saeed, M. D. 2008. Effect of non-volatile solute on the freezing point of malonic acid. *Bayero Journal of Pure and Applied Sciences*. 1(1): 53-57

Ulrich, J. & Stelzer, T. 2011. *Kirk Othmer Encyclopaedia in Chemical Technology.* 5th ed. England: John Wiley and Sons Ltd.

Vaessen, R., Seckler, M. & Witkamp, G. 2003. Eutectic Freeze Crystallization with an aqueous KNO_3-HNO_3 solution in a 100 L Cooled Disk Column Crystallizer. *Industrial and Engineering Chemistry Research.* 42(20):4874-4880.

van der Ham, F. 1999. *Eutectic Freeze Crystallization*. Delft, Netherlands: Technical University of Delft.

van der Ham, F., Witkamp, G., de Graauw, J. & van Rosmalen, G. 1998. Eutectic Freeze Crystallization: Application to process streams and waste water purification. *Chemical Engineering and Processing.* 37:207-213.

Vavouraki, A. I. & Koutsoukos, P. G. 2012. Kinetics of crystal growth of mirabilite in aqueous supersaturated solutions. *Journal of Crystal Growth*. 338(1): 189 – 194.

Veintemillas-Verdaquer, S. 1996. Chemical aspects of the effect of impurities in crystal growth. *Crystal Growth and Characterization*. 32(1-3): 75 – 109.

Virone, C., ter Horst, J. H. Kramer, H. J. M. & Jansens, P. J. 2005. Growth rate dispersion of ammonium sulphate attrition fragments. *Journal of Crystal Growth*. 275(1-2): e1397-e1401

Weijnen, M.P.C., Marchee, W.G.J. & van Rosmalen, G.M. 1983. A quantification of the effectiveness of an inhibitor on the growth process of a scalant. *Desalination.* 47: 81-92.

Weijnen, M.P.C. & van Rosmalen, G.M. 1986. Adsorption of phosphonates on gypsum crystals. *Journal of Crystal Growth.* 79(1-3): 157-168.

Weissbuch, I., Addadi, L., Lahav, M. & Leiserowitz, L. 1991. Molecular recognition at crystal interfaces. *Science*. 253(5020): 637-645

Yang, X., Qian, G., Duan, X. & Zhou, X. 2012. Effect of impurity on the lateral crystal growth of L-alanine: A combined simulation and experimental study. *Industrial and Engineering Chemistry Research*. 51: 14845-14849

Yang, X., Qian, G., Duan, X. & Zhou, X. 2013. Impurity effect of L-valine on L-alanine crystal growth. *Crystal Growth and Design*. 13: 1295-1300

9 Appendices

9.1 Appendix 1

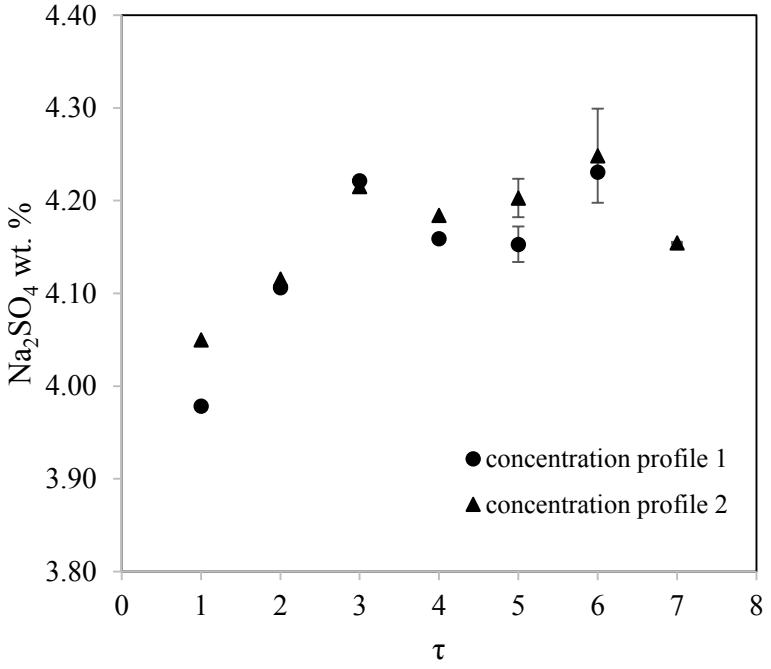

Figure 9-1. Concentration profiles for two experiments

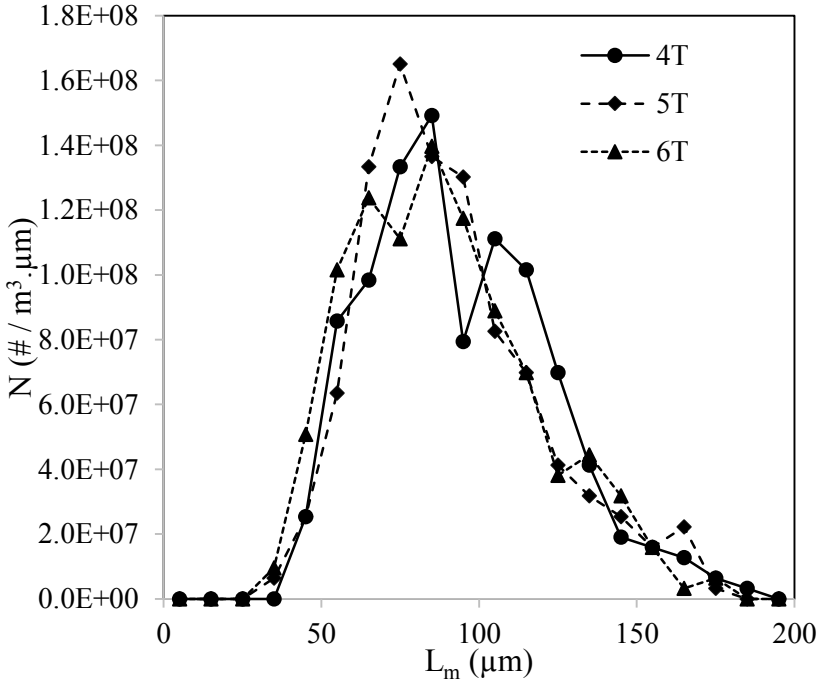

Figure 9-2. CSDs obtained at 4τ, 5τ and 6τ for salt in the presence of 350 mg/L antiscalant

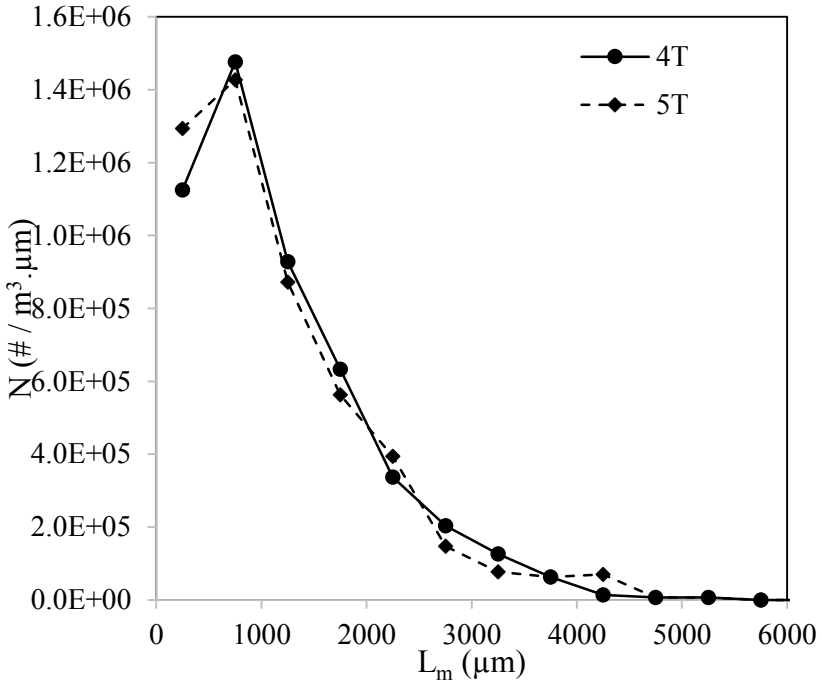

Figure 9-3. CSDs obtained at 4τ and 5τ for ice in the presence of 200 mg/L antiscalant

9.2 Appendix 2

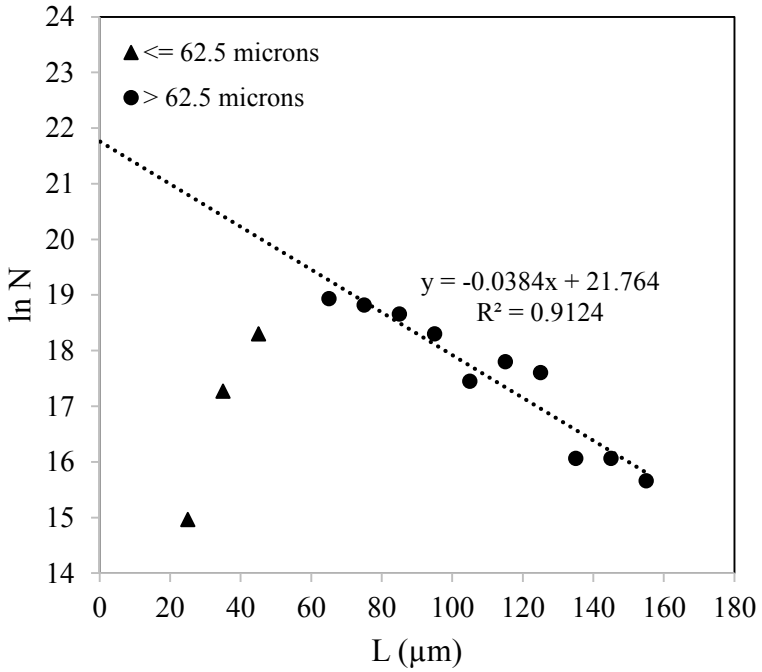

Figure 9-4. Semi-logarithmic plot of the crystal population density and crystal size for salt

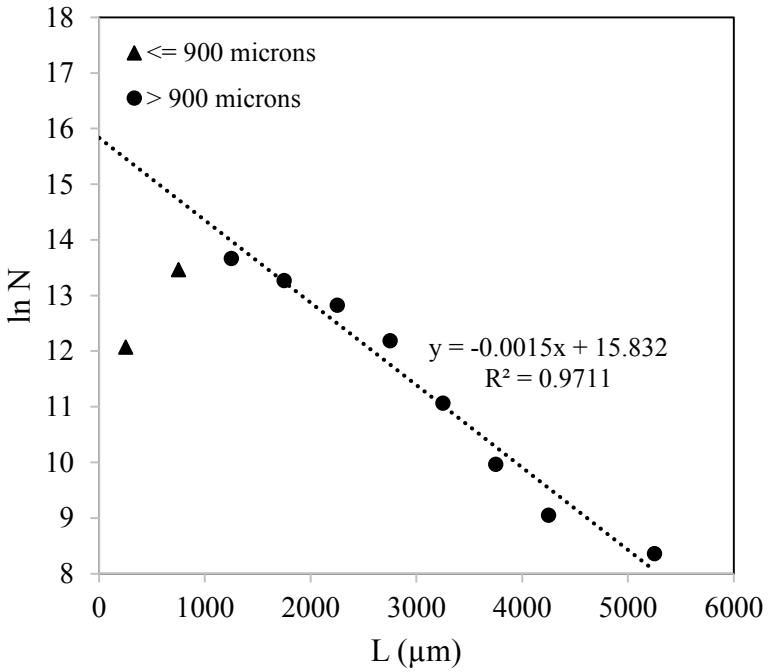

Figure 9-5. Semi-logarithmic plot of the crystal population density and crystal size for ice

9.3 Appendix 3

Table 9-1. Variation of mean, median and modal salt crystal sizes with antiscalant concentration

Experiment	Mean size (µm)	Median size (µm)	Modal size (µm)	CV (%)
Control	77.85±1.97	71.30±2.35	62.87±5.28	32.18±5.60
200 mg/L	86.77±1.69	82.66±1.84	66.73±4.53	30.49±4.65
350 mg/L	90.96±1.16	87.24±0.63	76.04±3.36	31.07±3.05
500 mg/L	81.09±1.66	75.64±1.12	64.84±5.04	33.65±6.14

Table 9-2. Variation of mean, median and modal ice crystal sizes with antiscalant concentration

Experiment	Mean size (µm)	Median size (µm)	Modal size (µm)	CV (%)
Control	1448.83±18.25	1315.23±42.18	834.58±176.52	53.89±5.99
200 mg/L	1160.93±8.52	903.48±17.47	480.65±53.84	74.18±3.73
350 mg/L	1251.76±1.09	891.76±56.99	274.19±31.61	79.71±3.16
500 mg/L	1676.85±19.46	1419.03±36.08	480.51±102.48	65.35±2.43

9.4 Appendix 4

Table 9-3. Variation of nucleation and growth rates of salt with antiscalant concentration

Experiment	B (# / cm^3.s)	G (µm / min)
Control	35.39±5.83	0.91±0.03
200 mg/L	37.98±3.59	0.95±0.04
350 mg/L	33.86±2.50	1.09±0.01
500 mg/L	33.05±4.70	1.05±0.09

Table 9-4. Variation of nucleation and growth rates of ice with antiscalant concentration

Experiment	B (# / cm^3.s)	G (µm / min)
Control	3.65±0.67	26.26±2.86
200 mg/L	2.50±0.16	25.79±1.40
350 mg/L	1.91±0.12	33.67±2.38
500 mg/L	2.43±0.22	35.19±1.31

9.5 Appendix 5

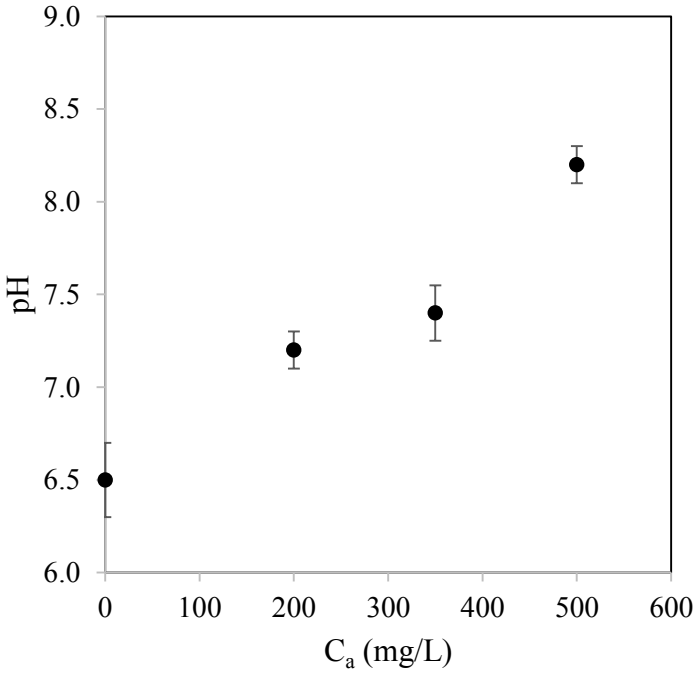

Figure 9-6. Variation of pH with antiscalant concentration

9.6 Appendix 6

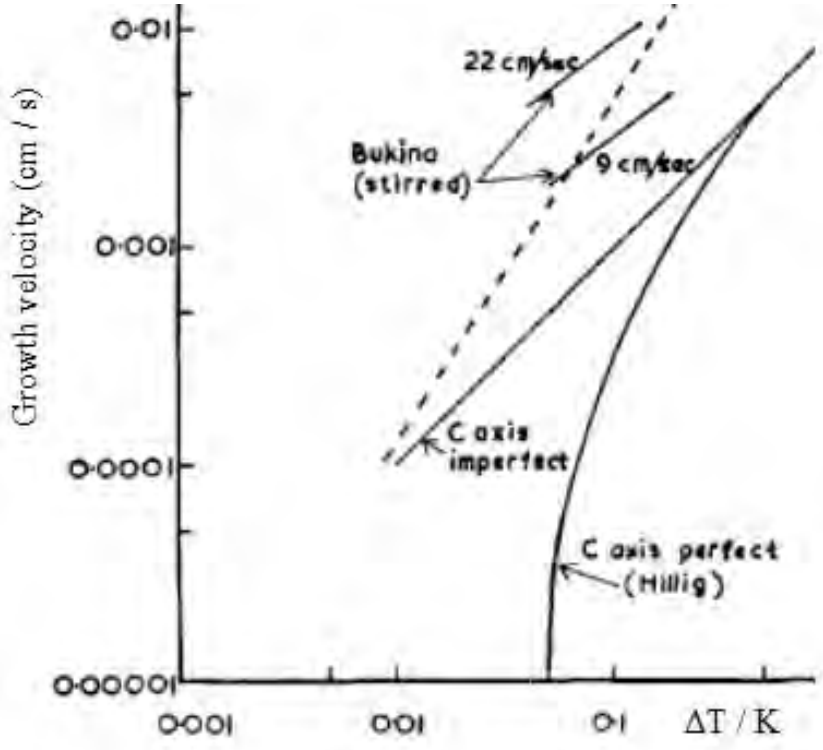

Figure 9-7. Growth velocity parallel to the basal plane (unmarked) and parallel to the 'c' axis, according to various authors (adopted from Halett, 1964)